SEARCH FOR NEW HEAVY RESONANCES DECAYING TO $\tau^+\tau^-$ PAIRS AT THE LHC WITH $\sqrt{S}$ = 7 TEV (L = 5.0 FB^{-1})

A Dissertation

by

INDARA MAYELI SUAREZ

Submitted to the Office of Graduate and Professional Studies of
Texas A&M University
in partial fulfillment of the requirements for the degree of

DOCTOR OF PHILOSOPHY

Chair of Committee,	Alexei Safonov
Committee Members,	Bhaskar Dutta
	Teruki Kamon
	Peter McIntyre
	Shery Yenello
Head of Department,	George Welch

May 2015

Major Subject: Physics

ABSTRACT

The Standard Model (SM) describes the known fundamental particles and their interactions due to the electromagnetic, weak, and strong forces through vector boson exchange. Although the SM has had major success in predicting a wealth of experimental measurements, astrophysical evidence for dark matter the observation of neutrino oscillations, and the matter-antimatter asymmetry in the universe indicate that the SM is not a complete theory. In addition to these experimental observations, problems stemming from the failure to incorporate the gravitational force and the quantum instability of the mass of the Higgs Boson have also contributed to the motivation to search for physics beyond the SM. Multiple theoretical scenarios, including those inspired by Grand Unified Theories (GUTs), models with extra spatial dimensions, and Supersymmetry (SUSY), have been proposed to address the shortcomings of the SM. In many of these models, the new symmetries that extend the SM gauge structure require the existence of new heavy neutral gauge bosons. Regardless of the exact nature or production mechanism of the hypothesized heavy bosons, they may be observed by studying dilepton final states at high energy colliders. As many models of physics beyond the SM predict enhanced couplings to third generation particles, searches for the new heavy bosons decaying into two τ-leptons are particularly well motivated. We present a direct search for high mass neutral resonances decaying into two opposite sign τ-leptons using data from proton-proton collisions at the LHC with center-of-mass energy $\sqrt{s} = 7$ TeV. The search has been conducted using data recorded by the Compact Muon Solenoid (CMS) experiment, corresponding to an integrated luminosity of 4.94 fb^{-1} and includes final states with leptonic and hadronic decays of the τ-lepton. The data has been found to be consistent with the

background-only hypothesis within the sensitivity of the measurement. Using the Sequential Standard Model Z'-boson as a benchmark, we set a 95% confidence-level upper limit on the mass of Z′-bosons decaying to pairs of τ-leptons.

DEDICATION

Dedico con gran orgullo y placer este trabajo a mi familia. Nunca encontrare las palabras adecuadas para agradecerles todo lo que han hecho por mi. Sin su apoyo y amor, no habría podido llegar tan lejos. Gracias a ustedes he tenido el privilegio de seguir mis sueños y he sido muy afortunada en tener la vida que tengo. Muchas gracias por la vida que me han dado.

ACKNOWLEDGEMENTS

This journey could not have been successful without the support and guidance of many people. I wish I could name everyone that has helped me get to this point; however, I would need another month to finish my thesis.

First, I would like to say that this accomplishment has been influenced significantly by the mentorship I received while participating in numerous physics research projects and outreach programs as an undergraduate student. Undoubtedly, this graduate journey became a reality thanks to the guidance and mentorship from Prof. Bernard Nefkens (R.I.P.) and Francoise Queval from the University of California, Los Angeles. Moving from Los Angeles to Texas was not an easy decision; however the faculty and staff from the Texas A&M Department of Physics and Astronomy have provided many opportunities for academic and personal growth that have led to the completion of this degree.

I am extremely grateful to my adviser, Professor Alexei Safonov. Throughout my time at Texas A&M, Alexei challenged me with a variety of exciting physics projects and helped me develop the skills needed to be successful in each of them. In addition to the vast scientific knowledge that I have acquired while working with Alexei, I have also learned how to become a great leader and been encouraged to continue developing my passion for education and outreach. Thanks to him, I will be leaving Texas A&M with the necessary skills to be successful and conquer the world.

I would also like to extend my gratitude to my friend and mentor, Dr. Alfredo Gurrola. Alfredo provided me with mentoring throughout the analysis presented in this thesis. Furthermore, he has continued to make time for our wonderful physics discussions. Alfredo has not only taught me a great deal of physics, but also helped

me become more assertive (he is to blame for my outspokenness). I am grateful to him and his wife, Leslie, for their incredible support throughout my time in graduate school, and for welcoming me into the lives of the little Gurrolas.

In addition to Alexei and Alfredo, I would also like to thank Dr. Eduardo Luiggi, who provided guidance throughout the High Mass Di-Tau analysis and the WH analysis, along with the rest of the High Mass Di-Tau working group. I had a great time working with all y'all and learned a great deal of physics!

Perhaps one of the best things that have happened in my life was moving to CERN and becoming involved with the ME1/1 upgrade. My time at CERN could not have been successful without my ME1/1 and CSC coworkers, many of whom have become friends for life. I had an incredible time working and learning from all of you. Dr. Jason Gilmore, thanks for helping me discover my passion for hardware. Dr. Joe Haley and Dr. Shalhout Shalhout, thank you for letting me be my bossy self. Dr. Pieter Everaerst, Evaldas Juska, and Dr. Frank Golf, thank you for those endless times at p5 and b904, as well as your friendship; we will forever share our love for Belgium beer and buenos! I would also like to thank Prof. Darien Wood, Prof. Stan Durkin, Prof. Jay Hauser for their amazing support and guidance.

I am thankful to my wonderful friends who have always been there for me. Thank you Alonso Sanchez Moguel, Juanita Vaquero, Sergio Gonzalez, and Sylvia Zamora for your unconditional love, patience, and guidance; without each of you, I would have not been able to accomplish this dream. Yaniel Cabrera, Karie Malconian, Elizabeth Sooby, and Nykkiesha Starr, thank you for keeping me sane in Texas. Lizz and Anthony Rose, thank you for your support during the time this thesis was written (and for my red hair). Kathryn Tschann-Grimm, thank you for adopting me at CERN and teaching me about the reasons for not wearing cowboy boots in the snow. Kim-Vy Tran and Helmut Katzgraber, thank you for your advice, support, and

delicious cooking. I would also like to thank my poor friends who had the misfortune to be forced to read my thesis, Slava Krutelyov, Matthias Weber, and Nick Amin.

This thesis could not have been possible without the love and support of my family. They have always supported me in every way they knew how and always encouraged my academic endeavors. Thanks to my parents, Isabel and Melquiades, I have had the privilege to pursue my dreams and have been very lucky to have the life I have. My brothers Israel and Isaac have always been there for me and taught me how to be strong.

Finally, I would like National Science Foundation Graduate Research Fellowship Program for the vital financial support during the past three years.

TABLE OF CONTENTS

Page

LIST OF FIGURES

FIGURE Page

LIST OF TABLES

TABLE Page

1. INTRODUCTION

The most widely validated theory of particle physics is the Standard Model (SM), [8, 9, 10], which successfully describes the electromagnetic, strong, and weak forces. The SM is a gauge field theory invariant under the $SU(3)_C \otimes SU(2)_L \otimes U(1)_Y$ symmetry group; it describes fermions (spin-1/2 particles) as the fundamental constituents of matter and bosons (spin-1 particles) as the force carriers that mediate interactions between fermions. Due to gauge invariance, the gauge bosons mediating the three unified forces are predicted to be massless. It has been experimentally verified that the bosons mediating the electromagnetic interactions between charged particles, γ's, and the strong interactions between particles with color charge, gluons, are massless particles (or at least, there are stringent limits suggesting they are incredibly light). However, the weak force carriers, $W^{\pm}$ and Z^0 bosons, not only have non-zero mass but have been measured to be almost 100 times heavier than the proton.

In 1964, Francois Englert, Brout, and Peter Higgs introduced the Higgs Mechanism into the SM [11, 12, 13], in order to explain how the $W^{\pm}$ and Z^0 bosons acquire their masses through spontaneous symmetry breaking. Incidentally, in the SM the Higgs mechanism also provides masses to fermions and the Higgs boson itself. This led to the prediction of the Higgs Boson, a neutral spin-0 scalar particle. On July 4th 2012, CMS and ATLAS, the two general purpose LHC experiments, announced the discovery of a new particle with mass of 125.5 ± 0.5 GeV/c^2 [14, 15], with properties consistent with the hypothesized SM Higgs Boson. The discovery represents the culmination of nearly a half-century effort to find the last missing piece of the SM.

Despite the many high precision experiments that have now confirmed the validity of the SM, it remains an incomplete theory of nature. Although its primary problem is the inability to incorporate the gravitational force, it has many other shortcomings. Even the success of the Higgs boson discovery points to a major problem with the SM: the need for extremely fine tuning to cancel very large quantum corrections in order for the Higgs boson to have a mass at the electroweak symmetry breaking scale of order 100 GeV. Furthermore, several experimentally observed phenomena, such as neutrino oscillations [16, 17, 18] and the astrophysical observations of Dark Matter/Energy, e.g. by the Wilkinson Microwave Anisotropy Probe (WMAP) [19], are not incorporated in the SM. Many well-motivated scenarios of physics Beyond the SM (BSM), such as Grand Unified Theories (GUT's) [20], models with extra spatial dimensions [21], Supersymmetry (SUSY) [22], have been developed as candidates for a more complete theory of nature. All of these predict new neutral gauge bosons by extending the SM gauge structure. While the new neutral resonances may have different nature and production mechanisms depending on the model, e.g. heavy SUSY Higgs, Z' bosons or Kaluza Klein excitations, they all share a similar experimentally observable signature and can likely be observed at the LHC.

Due to their clean signatures, dilepton final states have historically been great channels for discovery, e.g. J/ψ, Z-boson. Small and well-understood backgrounds make them the final states of choice for searches for new heavy neutral resonances at hadron colliders. Earlier searches for such new bosons suggest their mass to be in hundreds of GeV or heavier. The experimental signature for Z' boson production will be an enhancement in the high-mass region. In the case where the dileptons are muons or electrons, a fully reconstructable final state is available and the enhancement will be a narrow peak in the invariant mass distribution of two leptons. While analyses of the dielectron and dimuon final states are often considered "stan-

dard candles" in searches for heavy new resonances, the di-tau channel is equally important. While more challenging, as part of the energy in tau decays escapes detection not allowing reconstructing a narrow peak at the mass of the new boson, these searches may provide a unique opportunity for discovery since many theories beyond the Standard Model predict enhanced couplings to third-generation particles [23]. In this thesis, we present the search for heavy neutral resonances decaying into two high-p_T τ-leptons with data from the Compact Muon Solenoid Detector at CERN's LHC.

2. PHYSICS BEYOND THE STANDARD MODEL OF PARTICLE PHYSICS

In modern models of Particle Physics, interactions between particles are described in terms of four fundamental forces: the gravitational force, the electromagnetic force, the strong force, and the weak force. Each of the fundamental forces is characterized by its strength, manifested by the corresponding coupling constant, and its effective range. Measured in "natural" units of $\hbar$ and c, this range can be interpreted as an inverse of the energy scale characteristic to the interaction. While theoretical and experimental particle physicists have worked together over the past few decades to formulate a theory that describes nature at all energy scales by unifying the four forces of nature, these attempts have not yet succeeded.

2.1 The Standard Model of Particle Physics

The Standard Model (SM) of Particle Physics [8, 9, 10] successfully describes three of the four fundamental forces of nature (the electromagnetic, strong, and weak forces) through a quantum gauge field theory. Based on the gauge group $SU(3)_C \otimes SU(2)_L \otimes U(1)_Y$, the SM describes fermions (spin-1/2 particles) as the fundamental constituents of matter and bosons (spin-1 particles) as the force carriers that mediate interactions between fermions.

The 12 fundamental particles that constitute all observable matter are divided into three generations that are ordered in terms of mass hierarchy. According to this order, higher generation particles will decay into first generation particles (with the possible exception of neutrinos). Each generation is composed of two quarks and two leptons (shown in Figure 2.1). Quarks are fermions that carry fractional electric charge (-1/3, 2/3) and color charge (quantum number analogous to electric charge).

The six quarks in order of increasing mass are:

- Generation I : up (2.3 MeV), down (4.8 MeV)
- Generation II : strange (95.0 MeV), charm(1.27 GeV)
- Generation III : bottom (4.2 GeV), top (173.2 GeV)

Quarks carry one of three possible color charge ("red", "blue", and "green") and have anti-particles associated with them.

Fermions with integer electric charge (0 or 1) and no color charge are known as leptons. Neutral leptons, or neutrinos, are weakly interacting particles with very small mass. The neutrino masses remain unknown, however upper limits have been established by various experiments [24, 25, 26]. The three generations of leptons are:

- Generation I : electron (0.511 MeV), electron neutrino (< 2.2 eV)
- Generation II : muon (105.7 MeV), muon neutrino (< 0.17 MeV)
- Generation III : tau (1.777 GeV), tau neutrino (< 15.5 MeV)

The interactions between particles through the fundamental forces included in the SM are modeled by a gauge field theory invariant under the

$$SU(3)_C \otimes SU(2)_L \otimes U(1)_Y \tag{2.1}$$

symmetry group and are mediated by vector bosons. The strong force is represented by the $SU(3)_C$ term and is mediated by gluons, massless neutral particles. The weak force is represented by $SU(2)_L$ and it's interactions are carried through the exchange of massive bosons, $W^{\pm}$ and Z^0. The $U(1)_Y$ is a superposition of the weak neutral current and the photonic degrees of freedom. The latter of which is mediated by

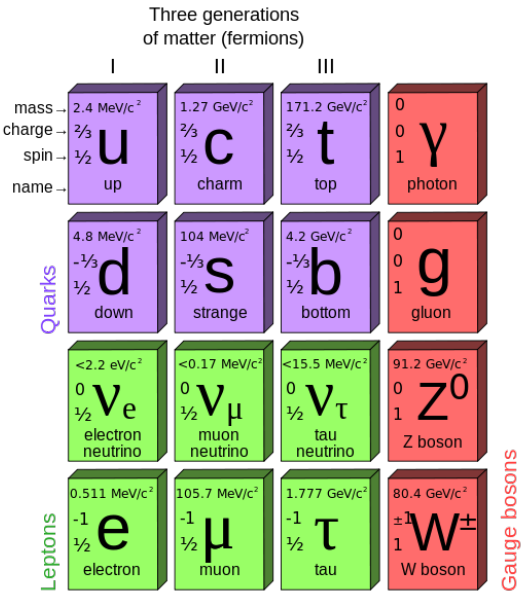

Figure 2.1: The Building Blocks of Matter. According to the Standard Model, matter is composed of three generations of fermions (spin-1/2 particles) that interact through the exchange of gauge bosons (spin-1 particles).

photons and is invariant under a $U(1)_Q$ gauge symmetry. The unification of the electromagnetic and weak force is represented by the $SU(2)_L \otimes U(1)_Y$ term in the SM gauge group shown in Equation 2.1. However, due to the introduction of the Higgs potential, the $SU(2)_L \otimes U(1)_Y$ symmetry is spontaneously broken and only the $U(1)_Q$ symmetry remains intact.

A summary of the three generation of particles and the vector bosons that mediate their interactions is shown in Figure 2.1. The fundamental forces and their gauge group representations will be explained in more detail in the following sections.

2.1.1 The Strong Force and the Theory of Quantum Chromodynamics

The strong force interactions are described by the theory of Quantum Chromodynamics (QCD) [27]. The strong force is responsible for interactions between particles

that carry color charge (quarks and gluons). The QCD Lagrangian is:

$$L_{QCD} = \sum_{q} \bar{\psi}_{q,a}(i\gamma^{\mu}\partial_{\mu}\delta_{ab} - g_s\gamma^{\mu}t^{C}_{ab}A^{C}_{\mu} - m_q\delta_{ab})\psi_{q,b} - \frac{1}{4}F^{A}_{\mu\nu}F^{A\mu\nu} \tag{2.2}$$

summed over color indexes a, b (running from a = 1 to $N_C = 3$ for the three colors of quarks), C (the gluon type running from C = 1 to N_C^2 - 1 = 8 for the eight types of gluons), and q (where flavor is the term for the type of quark, i.e. q = u, d, s, c, b, or t). The field tensor, $F^{A}_{\mu\nu}$, is defined as:

$$F^{A}_{\mu\nu} = \partial_{\mu}A^{A}_{\nu} - \partial_{\nu}A^{A}_{\mu} - g_s f_{ABC}A^{B}_{\mu}A^{C}_{\nu} \tag{2.3}$$

such that:

$$[t^{A}, t^{B}] = if_{ABC}t^{C} \tag{2.4}$$

The components of the QCD Lagrangian are

- $\psi_{q,a}$, quark-field spinors for a quark of flavor q and mass m_q
- γ^{μ}, the Dirac γ matrices
- t^{C}_{ab}, the generators of the SU(3) group
- A^{C}_{μ}, gluon fields. Gluons also carry color therefore they can interact with quarks and with each other.
- g_s, the QCD coupling constant
- f_{ABC}, structure constants of the SU(3) group

The QCD Lagrangian is characterized by invariance under SU(3) denoted by the $SU(3)_C$ term in the SM gauge group in Equation 2.1, where C is color charge in this

case. Strong force interactions between quarks are invariant under color interchange. Furthermore, quarks and gluons have never been observed as free particles but instead are confined in hadrons, color neutral states composed of quarks, anti-quarks, and gluons.

2.1.2 The Electromagnetic Force and the Theory of Quantum Electrodynamics

The electromagnetic force is modeled by Quantum Electrodynamics (QED) where gauge invariance under $U(1)_Q$ describes interactions between particles with electric charge Q. In the SM, the $U(1)_Q$ subgroup remains unbroken after spontaneous symmetry breaking ($SU(2)_L \otimes U(1)_Y \rightarrow U(1)_Q$). Therefore, the QED Lagrangian for a charged fermion interacting with an electromagnetic field is:

$$L_{QED} = \sum_q \bar{\psi}(i\gamma^\mu D_\mu - m)\psi - \frac{1}{4}F_{\mu\nu}F^{\mu\nu} \tag{2.5}$$

where the gauge covariant derivative, D_μ, is defined as:

$$D_\mu \equiv \partial_\mu + ieA_\mu \tag{2.6}$$

and the field tensor is:

$$F_{\mu\nu} = \partial_\mu A_\nu - \partial_\nu A_\mu \tag{2.7}$$

The other variables in the QED Lagrangian are:

- ψ, fermion-field spinor for a charged, spin-1/2 particle with mass m
- γ^μ, the Dirac γ matrices
- A_μ is the vector potential of the electromagnetic field generated by the charged fermion

- e is the coupling constant equal to the charge, Q, of the fermion

Invariance of the QED Lagrangian under U(1) phase transformation, $\psi \rightarrow e^{i\alpha(x)}\psi'$, and gauge transformation, $A_\mu(x) \rightarrow A_\mu(x) - \frac{1}{e}\partial_\mu\alpha(x)$, results in a zero mass term for the force mediator, the photon. Since U(1) is an Abelian group, there is no photon self-interaction. These two results are consistent with experimental observations.

2.1.3 Electroweak Theory and The Higgs Mechanism

The SM describes the electroweak interaction by a gauge field theory invariant under the $SU(2)_L \otimes U(1)_Y$ known as Electroweak (EW) Theory [8, 9]. EW Theory is a nice feature of the standard model as it unifies the electromagnetic and weak forces. In this formulation, the $SU(2)_L$ component represents the weak interaction with left-handed particles. Through experimental observations, it has been shown that the $W^{\pm}$ bosons, charged particles mediating weak force interactions, only interact with left-handed fermions [28, 29]. Therefore the three generations can be represented as:

$$\psi_1 = \nu_{e_L}, e_L, e_R, (u_L, u_R, d_L, d_R)_\alpha \tag{2.8}$$

$$\psi_2 = \nu_{\mu_L}, \mu_L, \mu_R, (s_L, s_R, c_L, c_R)_\alpha \tag{2.9}$$

$$\psi_3 = \nu_{\tau_L}, \tau_L, \tau_R, (b_L, b_R, t_L, t_R)_\alpha \tag{2.10}$$

where $\alpha = 1, 2, 3$ is the colour index for the quark fields. The left-handed and right-handed fermion fields are:

$$\psi_L = \tfrac{1}{2}(1 - \gamma_5)\psi \tag{2.11}$$

$$\psi_R = \tfrac{1}{2}(1 + \gamma_5)\psi \tag{2.12}$$

respectively, i.e. $e_L = \frac{1}{2}(1-\gamma_5)e$ and $e_R = \frac{1}{2}(1+\gamma_5)e$.

The Lagrangian that describes electroweak interactions is:

$$L_{EW} = \sum_q \bar{\psi}(i\gamma^\mu D_\mu)\psi - \frac{1}{4}F^i_{\mu\nu}F^{i\mu\nu} - \frac{1}{4}G_{\mu\nu}G^{\mu\nu} \tag{2.13}$$

whereγ^μ are the Dirac matrices, the covariant derivative is,

$$D_\mu = \partial_\mu - igTA_\mu - ig'\frac{Y}{2}B_\mu. \tag{2.14}$$

and $F^i_{\mu\nu} = \partial_\mu A^i_\nu - \partial_\nu A^i_\mu + g\epsilon^{i,j,k}A^j_\mu A^k_\nu$ and $G_{\mu\nu} = \partial_\mu B_\nu - \partial_\nu B_\mu$. The A^i, i = 1, 2, 3, represents the gauge bosons associated with weak force interactions. In weak force interactions, *weak isospin* T, the third component of isospin, is conserved. Since the weak force only acts on left-handed particles, right-handed fermions have zero isospin and do not couple with W bosons. B_μ is the gauge boson corresponds to the $U(1)_Y$ factor, under which hypercharge, Y, is conserved. The hypercharge is defined by:

$$Q = \frac{Y}{2} + T, \tag{2.15}$$

where Q is the electric charge. The coupling constant for $SU(2)_L$ and $U(1)_Y$ are g and g', respectively.

The EW Lagrangian, Equation 2.13, is invariant under the local gauge transformations:

$$\psi_L \rightarrow e^{ig\alpha(x)T + ig'\beta(x)Y}\psi_L \tag{2.16}$$

$$\psi_R \rightarrow e^{ig'\beta(x)Y}\psi_R \tag{2.17}$$

where the left-handed fermion fields and the right-handed fermion fields are defined on Equation 2.11. Local gauge invariance of the L_{EW} results in the generation of

bosons associated with the electroweak force, the photon:

$$A_\mu = cos\theta_W B_\mu + sin\theta_W A^3_\mu \tag{2.18}$$

and the neutral Z boson and charged W bosons:

$$Z_\mu = -sin\theta_W B_\mu + cos\theta_W A^3_\mu \tag{2.19}$$

$$W^\pm_\mu = \frac{1}{\sqrt{2}}(A^1_\mu + A^2_\mu) \tag{2.20}$$

where the weak mixing angle, θ_W, is defined by $cos\theta_W = \frac{g}{\sqrt{g^2+g'^2}}$. According to these definitions, the gauge fields are predicted to be massless. However, experimental observations show that the $W^\pm$ and Z bosons are massive particles.

The Higgs mechanism was proposed in 1964 by Higgs and Englert [12, 13, 11] to generate the masses of the vector bosons mediating the electroweak interaction, Z and $W^\pm$. An additional term is introduced to the EW Lagrangian, L_{EW} defined by Equation 2.13,

$$L_{Higgs} = (D_\mu\phi)^\dagger(D^\mu\phi) - V(\phi) \tag{2.21}$$

where covariant derivative is defined by Equation 2.14 and the $V(\phi)$ is scalar potential

$$V(\phi) = \mu^2\phi^\dagger\phi + \lambda(\phi^\dagger\phi)^2 \tag{2.22}$$

and ϕ is an SU(2) complex doublet known as the Higgs field with weak hypercharge $Y = 1$:

$$\phi = \begin{pmatrix} \phi^\dagger \\ \phi^0 \end{pmatrix} \tag{2.23}$$

The mass of the Higgs field is represented by μ and λ is chosen to be positive in

order for the minimum energy to be bounded from below. By minimizing L_{Higgs} to obtain a ground state:

$$\phi^{\dagger}\phi = -\frac{\mu^2}{2\lambda} = \frac{v^2}{2} \tag{2.24}$$

The vacuum expectation value becomes:

$$\phi_0 = 0 \text{ for } \mu^2 > 0 \tag{2.25}$$

$$\phi_0 = \sqrt{\frac{\mu^2}{2\lambda}} e^{i\theta} \text{ for } \mu^2 > 0 \tag{2.26}$$

By choosing a vacuum state:

$$\phi_0 = \frac{1}{\sqrt{2}} \begin{pmatrix} 0 \\ v \end{pmatrix} \tag{2.27}$$

spontaneous symmetry breaking is introduced and the SM gauge is broken from $SU(3)_C \otimes SU(2)_L \otimes U(1)_Y$ into $SU(3)_C \otimes U(1)_Q$.

The original fields from the Higgs complex doublet (Equation 2.29) are parameterized in terms of four real fields:

$$\phi = \begin{pmatrix} \phi_1 + i\phi_2 \\ \phi_3 + i\phi_4 \end{pmatrix} \tag{2.28}$$

Then the fields are transformed into the unitary gauge:

$$\phi = \begin{pmatrix} 0 \\ \frac{v+\eta(x)}{\sqrt{2}} \end{pmatrix} \tag{2.29}$$

The Electroweak Lagrangian with the inclusion of the new scalar field becomes:

$$L = L_{EW} + L_{Higgs} + L_{Yukawa} \tag{2.30}$$

where L_{EW} is defined in Equation 2.13, L_{Higgs} is shown in Equation 2.21, and the Lagrangian due to Yukawa interactions. By expanding Equation 2.30 around $\phi(x) = v + \eta(x)$, where v is the ground state shown in Equation 2.27, a mass term for the Higgs field, $m_\eta = \sqrt{2}\mu$, appears predicting the existence of a new massive scalar boson. The masses for the vector bosons associated with electroweak theory to lowest order in perturbation theory become:

$$M_W = \tfrac{1}{2}gv = \tfrac{ev}{2sin\theta_W} \tag{2.31}$$

$$M_Z = \tfrac{1}{2}\sqrt{g^2 + g'^2}v = \tfrac{ev}{2sin\theta_W cos\theta_W} = \tfrac{M_W}{cos\theta_W} \tag{2.32}$$

$$M_\gamma = 0 \tag{2.33}$$

The fermion masses will be generated by the L_{Yukawa} component of the Electroweark Lagrangian. The Lagrangian due to Yukawa interactions is:

$$L_{Yukawa} = f^{(e)}\bar{l_L}\phi_{e_R} + f^{(u)}\bar{q_L}\tilde{\phi}_{u_R} + f^{(d)}\bar{q_L}\phi_{d_R} + h.c. \tag{2.34}$$

where $\tilde{\phi} = iT\phi^*$ is the isodoublet with hypercharge $Y(\tilde{\phi}) = -1$ and $q_L(l_L)$ and $u_R, d_R(e_R)$ are the quark (lepton) $SU(2)_L$ doublets and singlets. When the Higgs acquires a vacuum expectation value, fermions will acquire a mass defined by:

$$m_f = \frac{f^{(i)}v}{\sqrt{2}}. \tag{2.35}$$

On July 4th 2012, the European Organization for Nuclear Research (CERN) announced the observation of a new particle by the CMS and ATLAS experiments at the Large Hadron Collider (LHC). The new boson has a mass of approximately 125 GeV and closely resembles the hypothesized SM Higgs boson.

2.2 Physics Beyond the Standard Model and New Neutral High Mass Resonances

Even though the discovery of the SM-like Higgs may represent the last missing piece of the SM, there is a wealth of evidence indicating that our understanding of nature is incomplete. If the newly discovered particle is indeed the SM Higgs Boson, it will point to one of the main problems with the theory itself. The well-known *hierarchy problem* [30] stems from the quantum instability of scalar masses since the SM requires fine cancelation of large quantum corrections in order for the Higgs boson to have a mass at the electroweak symmetry breaking scale of order of a 100 GeV. These questions surrounding the mass value of the Higgs [31] as well as astrophysical evidence for dark matter [19] suggest that new particles and interactions may be awaiting discovery at higher energy and are within the reach of the LHC. Furthermore, the description of the gravitational force as a QFT is absent in the SM, suggesting that the SM is an incomplete theory of Particle Physics. Attempts to reconcile some of these difficulties led to a raise of models such as Grand Unified Theories (GUT's) [20], models with extra spatial dimensions [21], Supersymmetry (SUSY) [22], which all predict heavy neutral resonances [32, 33]. New neutral spin-1 bosons are associated with additional gauge groups that are added to extend the SM gauge sector in order to address the problems with the SM. Their heavy masses can emerge from new local broken symmetries, similar to the Higgs mechanism in EW theory. The most simple scenario would be incorporating an additional U(1) gauge group into the SM gauge structure, that can be broken at the TeV scale resulting in the prediction of one or more Z' bosons.

For a given model to be a candidate for an ultimate theory, the new gauge boson must satisfy certain theoretical restrictions such as

- the new gauge boson must be associated with a spontaneously broken gauge symmetry to be well-behaved at high energies
- the new boson couplings to fermions must satisfy anomaly cancellation conditions in order to preserve gauge invariance
- fermions must get their masses from gauge-invariant interactions with the Higgs field

Furthermore, theoretical models can have either generation-independent (universal) or generation dependent couplings of the new gauge boson to fermions. Because of the difficulty in the reconstruction of di-tau final states, Z′ with theories with universal couplings will most likely be discovered in searches with Z′ decaying into e^+e^- or $\mu^+\mu^-$ final states. However, searches with $\tau^+\tau^-$ final states are important to probe models with enhanced third generation couplings [34, 35, 36], in addition to testing the universitality of couplings. Furthermore, τ polarization assymetry can help determine Z′ couplings to SM fermions if a discovery is made in the $\tau^+\tau^-$ final state [37].

2.2.1 Sequential Standard Model

One of the most popular simplified phenomenological models introducing a new Z′ boson is the Sequential Standard Model (SSM) [32]. Z′ bosons predicted by SSM, Z'_{SSM}, emerges by extending the SM gauge group with an extra $U'(1)$ and has the same couplings to ordinary fermions as the Z-boson. The SSM will not satisfy the requirements stated above as it is not a gauge invariant model. However, it is useful as a reference model in the interpretation of the results from this analysis to be able to compare to Z′ searches from different experiments.

2.2.2 Grand Unified Theories

Grand Unified Theories (GUTs) [38] aim at unifying the fundamental forces of nature by modeling them as a single unified gauge group. A feature of a GUT would be the unification of the coupling constants at higher energies. As shown in Figure 2.2, in the standard model the gauge couplings are independent arbitrary parameters. However in models such as the E_6 GUT Model [20] the coupling constants will unify at some large energy scale.

In the case of the E_6 model, the additional gauge bosons will be generated by the extra two U(1) gauge groups resulting from the decomposition of the E_6 group as follows:

$$E_6 \rightarrow SO(10) \times U(1)_\psi \tag{2.36}$$

$$SO(10) \rightarrow SU(5) \times U(1) \rightarrow G_{SM} \times U(1)_\chi \tag{2.37}$$

where G_{SM} is the SM gauge group shown in Equation 2.1. The observable from $U(1)_\psi$ is denoted as Z'_ψ whereas $U(1)_\chi$ generates Z'_χ. In this analysis, Z'_ψ, with the assumption that it has Z-like couplings to standard model fermions, will be used as an additional benchmark.

2.2.3 Supersymmetry

The E_6 model is phenomenologically interesting because they can be related to superstring models [20]. These models have Supersymmetry build in to deal with the hierarchy and fine-tunning problems of the SM. Supersymmetry is a proposed symmetry between fermions and bosons that predicts the existance of "superpartners" associated with the SM particles. The "superpartners" are expected to have

the same quantum numbers as their SM counterparts with the exception of their spin, which will differ by $\frac{1}{2}$. Astronomical evidence for dark matter points to SUSY models where the lightest predicted supersymmetric particle (LSP) serves as a dark matter candidate. While the SM requires large quantum corrections in order for the Higgs boson to have a mass at the electroweak symmetry breaking scale of order 100 GeV, SUSY provides a solution through the cancellations of the quadratic divergences of the top-quark and top-squark loops. In supersymmetric models the mass parameter for supersymmetric Higgs bosons H_u and H_d, μ, must be on the order of the electroweak scale to ensure that H_u and H_d have non-zero vacuum expectation values after electronweak symmetry breaking. However, popular models such as the Minimal Supersymmetric Model (MSSM) [39] could have an arbitrarily large μ, possibly as large as the Planck scale. E_6-inspired SUSY models, such as the Next-to-Minimal Supersymmetric Model (NMSSM) [40, 41], provide a natural solution to the μ problem. Such theories predict the existence of $\mathrm{Z}'_{\ \eta}$ that corresponds to a linear combination of the already defined $\mathrm{Z}'_{\ \Xi}$ and Z'_{ψ} [42]. By this construction the μ term is forbidden by the $U'(1)$ and instead a new term related to a gauge singlet, S, under the SM emerges. This gauge singlet is charged under the new $U'(1)$ and is assumed to have family universal couplings to SM fermions. SUSY also predicts a variety of new particles whose decays have enhanced couplings to third generation SM fermions [36].

2.3 Previous Searches for Heavy Resonances

Searches for Z' production have been conducted at both e^+e^- colliders and hadron ($p\bar{p}$ and pp) colliders. Searches for direct Z' production followed by decays into dilepton (e^+e^-, $\mu^+\mu^-$, and $\tau^+\tau^-$) final states have been used for these searches due to their clean signatures and low background rates. Additionally, searches have also

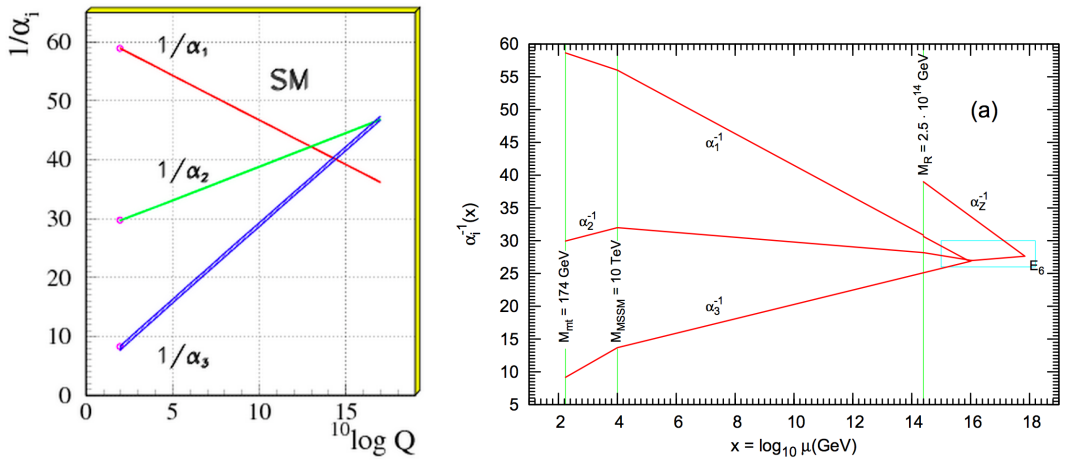

Figure 2.2: The Coupling Constants of the Fundamental Forces of Nature. These figures represent the running of the inverse coupling constants α^{-1} for the SM [1] (left) and for an example of a E_6 model (with Supersymmetry) [2] (right). The coupling constants for the strong (α_1), electromagnetic (α_2), and weak (α_3) forces. α_Z represents the gauge coupling constant of the E_6 gauge group.

been completed with $q\bar{q}$ final states. In the absence of an excess of data over SM hypothesis, stringent limits have been imposed on the Z$'$ mass. All limits presented here are calculated with a 95% confidence level and set on $\sigma(e^+e^- \to \mathrm{Z}') \times BR(\mathrm{Z}' \to f\bar{f})$ for e^+e^- searches, $\sigma(p\bar{p} \to \mathrm{Z}') \times BR(\mathrm{Z}' \to f\bar{f})$ for Tevatron searches and $\sigma(pp \to \mathrm{Z}') \times BR(\mathrm{Z}' \to f\bar{f})$ for LHC searches ($f = \tau^-, \mu^-, e^-$, or q). The limits discussed are based on the benchmark models, Z'_{SSM} and Z'_{ψ}, which assume universal couplings. Therefore, these limits are not reflective of models with enhanced couplings to third generation particles, where a ditau search has maximum sensitivity.

This section will review searches conducted prior to June 2012, which is when the results presented in this thesis were published [43]. Results published in 2012 represent searches completed with the full 2011 ($\sqrt{s} = 7$ TeV) LHC data set corresponding to ≈ 5.0 fb^{-1} of data collected by the CMS and ATLAS experiments. These results, as well as those from searches using 2012 ($\sqrt{s} = 8$ TeV) LHC, will be

summarized in the conclusion chapter of this thesis.

Data from the Large Electron Positron II (LEP-II) collider [44, 45] was used to search for direct Z′ production via $e^+e^- \rightarrow Z'$, where Z′ decays to dileptons ($Z' \rightarrow l^+l^-$, $l = \mu, e$, or τ). These searches determined that the mass of the theorized Z'_{SSM} must be larger than 209 GeV/c^2 [46]. Indirect searches for a Z′ were also conducted using LEP-II data. Limits on the Z′ mass can be set by studying constraints on Z - Z′ mixing [47]. Through indirect searches, LEP-II set limits on Z'_{SSM} and Z'_{ψ} of 1305 GeV and 475 GeV, respectively.

Searches for the production of new heavy neutral bosons at the Tevatron have been completed by the CDF and D0 collaborations using $p\bar{p}$ collision data. These searches include heavy resonances decaying into ditau ($\tau^+\tau^-$), dilepton (l^+l^-, where $l = e$ or μ), and dijet ($q\bar{q}$) final states. The CDF and D0 experiments published the most stringent results at the time before pre-LHC era, with Tevatron $p\bar{p}$ collision data with $\sqrt{s} = 1.96$ TeV. In January 2011, the CDF experiment published results from a search for heavy resonances decaying into $\mu^+\mu^-$ and excluded Z'_{SSM} masses below 1071 GeV/c^2 using 4.6 fb^{-1} total integrated luminosity [48]. In August 2010, the D0 collaboration reported an upper limit of 1023 GeV/c^2 on the mass of Z'_{SSM} using e^+e^- final states. In addition, the CDF collaboration had excluded Z'_{SSM} masses below 399 GeV/c^2 using 1.96 fb^{-1} of integrated luminosity [49] using Tevatron $p\bar{p}$ collision data. The CDF ditau search was the only previous result reported for Z′ bosons decaying into $\tau^+\tau^-$ final states. The CDF collaboration also had reported the largest restrictions on Z'_{SSM} using the $q\bar{q}$ channel [50] (2008), which excluded masses between 320 and 740 GeV/c^2 with 1.13 fb^{-1} of $p\bar{p}$ collision data.

At the Large Hadron Collider, direct searches for Z′ production have been performed by the ATLAS and CMS experiments using pp collision data with $\sqrt{s} = 7$ TeV. The first LHC Z′ results using dilepton final states were reported by the CMS

collaboration [51] in June 2011 and excluded masses below 1140 GeV/c^2 for Sequential Standard Model Z'_{SSM} and below 887 GeV/c^2 for the E_6 Z'_{ψ}. However, the most stringent limits on the mass of a Z'_{SSM} and a Z'_{ψ} resonance prior to 2012 were reported by the ATLAS collaboration [52] in August 2011. The search was performed with LHC pp collision data ($\sqrt{s}$ = 7 TeV) and included $Z' \rightarrow l^+l^-$ decays. It excluded Z'_{SSM} with masses below 1830 GeV/c^2 using data collected by the ATLAS experiment corresponding to a total integrated luminosity of 1.08 fb^{-1} in the $Z' \rightarrow e^+e^-$ channel and 1.21 fb^{-1} in the $Z' \rightarrow \mu^+\mu^-$ channel. Additionally, Z'_{ψ} resonances with masses below 1490 GeV/c^2 were also excluded by the combination of the $Z' \rightarrow l^+l^-$ channels. For studies with $\tau^+\tau^-$ final states, the analysis presented in this thesis is the most recent published result from the LHC experiments.

3. THE LARGE HADRON COLLIDER AND THE CMS DETECTOR

3.1 The Large Hadron Collider

The Large Hadron Collider (LHC) [53] accelerator has been designed to explore the fundamental properties of matter, search for the hypothesized SM Higgs boson, and address experimental observations not currently explained through the SM. The LHC is located at the European Center of Nuclear Research (CERN) on the border of France and Switzerland. It is contained inside the former Large Electron-Positron (LEP) [45] circular tunnel, which has a circumference of 27 km and is on average 100 meters underground. The four major experiments, A Large Ion Collider Experiment (ALICE) [54], LHC-b [55], A Toroidal LHC Apparatus (ATLAS) [56] and the Compact Muon Solenoid (CMS) [3], are located at different points around the main ring. The ATLAS and CMS are general purpose experiments searching for clues as to the nature of electroweak symmetry breaking, origin of mass, CP-violation, and dark matter. LHC-b focuses on exploring CP-violation in the interactions of b-hadrons, and ALICE is a heavy ion experiment studying quark-gluon plasma.

The CERN accelerator complex, shown in Figure 3.1, is an accelerator chain that accelerates protons to increasingly higher energies until they are ultimately delivered to the LHC ring. The protons originate from a simple bottle of hydrogen gas and are clustered into bunches that are accelerated until they reach 0.999999 of the speed of light, giving them a total energy of 3.5 TeV. To achieve these energies, they are first injected to LINAC2, a linear accelerator that accelerates them to energy of 50 MeV. The Proton Synchrotron Booster (PSB) then accelerates them to 1.4 GeV before being injected into the Proton Synchrotron (PS). The protons reach energies of 25 GeV by the time they exit the PS and enter the Super Proton Synchrotron (SPS),

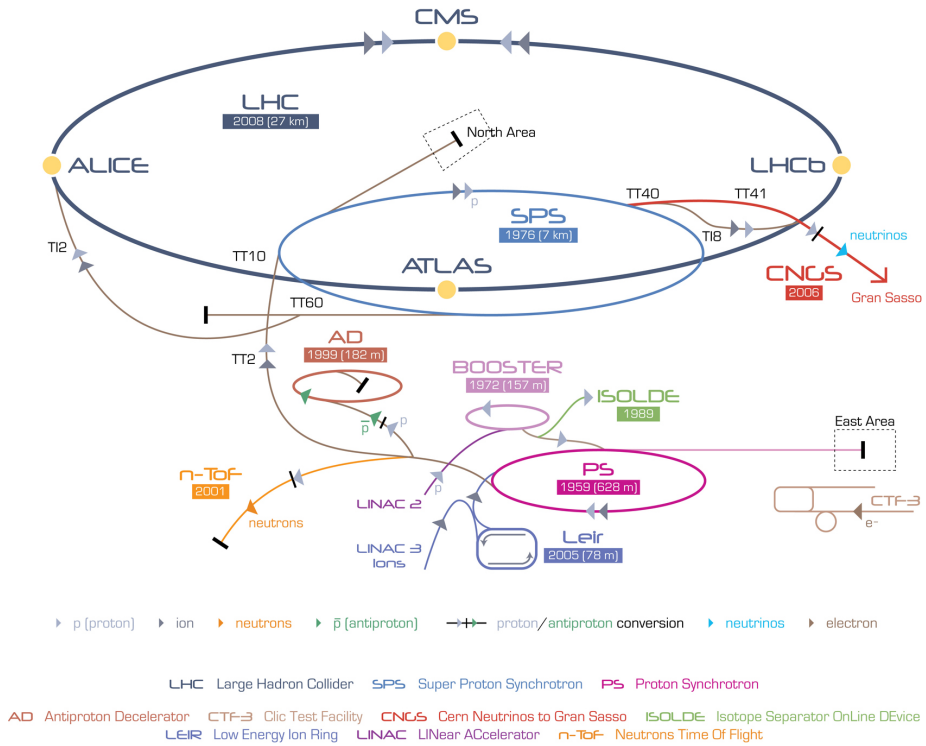

Figure 3.1: The Layout of the CERN Accelerator Complex. The accelerator chain consists of the Linear Accelerator (LINAC2), Proton Synchrotron Booster (PSB), Proton Synchrotron (PS), Super Proton Synchrotron (SPS), and the Large Hadron Collider (LHC). The protons injected into the accelerator chain reach velocities of 0.999999 of the speed of light, which correspond to a total energy of 3.5 TeV.

where they are accelerated to 450 GeV. After the SPS, the proton bunches enter the Large Hadron Collider.

In the LHC, the proton bunches travel inside two separate beam pipes in opposite directions. They are accelerated as they pass through radio frequency cavities and guided by dipole magnets around the ring. The superconducting coils making up the dipole magnets must be cooled down to a temperature near absolute zero at 1.9 K (-271.3°C) in order to be able to conduct electricity without resistance or loss of energy. In addition to the 1232 dipole magnets used to accelerate and guide the proton bunches, there are 392 quadrupole magnets used to focus the beam of proton

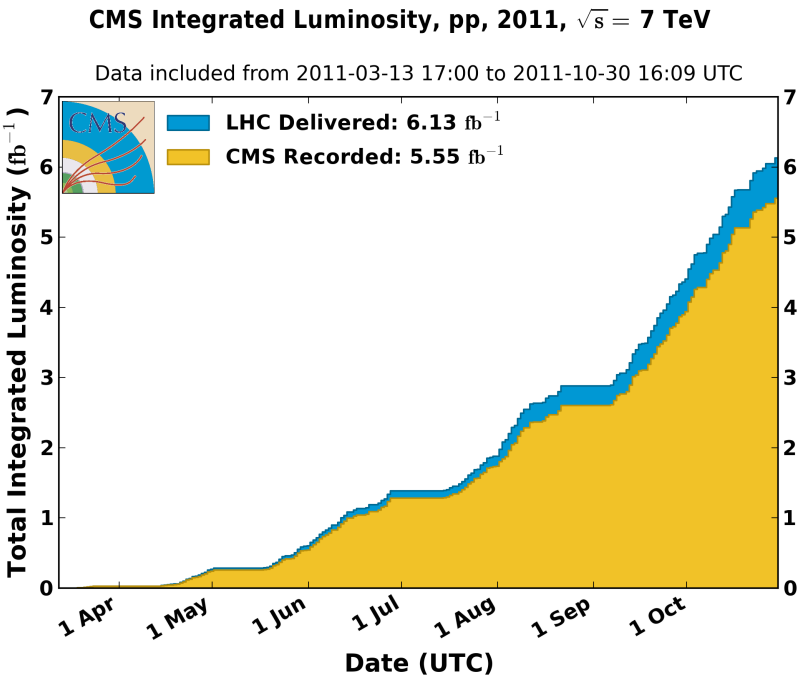

Figure 3.2: CMS Integrated Luminosity During the 2011 7 TeV Run (March - November 2011). The LHC delivered a total integrated luminosity of 6.13 fb^{-1} from pp collissions at $\sqrt{(s)}$=7 TeV center-of-mass energy to the CMS detector. CMS recorded 5.55 fb^{-1} of data.

bunches prior to collision. Once the proton bunches reach their maximum center-of-mass energy, the beams are adjusted to produce simultaneous collisions at each of the experimental points around the LHC ring. The LHC is designed for a 25 ns bunch-crossing window, gap between collisions. However, during the 2011 and 2012 physics runs, the LHC provided collisions every 50 ns.

In March 2011, the LHC began producing proton-proton collisions at center of mass energy $\sqrt{(s)} = 7$ TeV. The beam energies used in the 2011 and 2012 data runs (7 and 8 TeV, respectively) and the design luminosity of $10^{34} cm^{-2} s^{-1}$ were chosen in order to study physics at the TeV scale. Alternatives to the SM, such as models suggesting the existence of extra dimensions, require modifications of gravity

by invoking new symmetries and predict the existence of new gauge bosons at the TeV scale. This thesis presents a search for new neutral heavy resonance at the LHC using data collected by the CMS detector.

The LHC delivered a total integrated luminosity of 6.13 fb^{-1} of data between March - November 2011, see Figure 3.2, while the CMS detector recorded 5.55 fb^{-1}. However, only 4.94 fb^{-1} of the data was considered "good" for offline physics measurements, implying that all CMS subsystems were stable during this period, and thus used for this search. The systematic uncertainty of the luminosity measurement has been taken as 4%. The luminosity delived to CMS can be measured with two methods: i) data from the online Forward HCAL system (HF) or ii) by estimation of the production rate of primary vertices from *pp* collisions. Both these methods have shown good consitency and linearity over a wide range of luminosities. Calibration using Van der Meer scans is used to determine the absolute normalization for the luminosity measurement [57].

3.2 The Compact Muon Solenoid Detector

The Compact Muon Solenoid (CMS) Detector is one of the two general purpose detectors on the LHC accelerator ring, the other being ATLAS [56]. It is located near Cessy, France on the "Point 5" of the ring. It was built to search for the postulated Higgs Boson, explore the nature of electroweak symmetry breaking, and search for evidence of physics beyond the Standard Model.

The CMS Detector design includes:

- A pixel detector system close to the interaction region for efficient offline tagging of τ's and b-jets by providing efficient reconstruction of secondary vertices.
- A full-silicon-based inner tracking system that provides good charged-particle

momentum resolution and reconstruction efficiency.

- An Electromagnetic Calorimeter (ECAL) with excellent electromagnetic energy resolution and mass resolution of diphotons and dielectrons.

- A Hadronic Calorimeter (HCAL) with fine lateral segmentation for good missing-transverse-energy and dijet-mass resolution.

- A muon system to provide good muon identification as well as, in conjunction with the inner tracker, good momentum and dimuon mass resolution over a wide range of momenta with the ability to determine the charge of muons with momenta up to 1 TeV.

All of these subdetector systems must have a wide geometric coverage (4π solid angle) and maintain good resolutions over a wide range of particle momenta and directions. In addition to these subsystems, the CMS detector includes a unique high-field solenoid magnet currently operating at 3.8 Tesla (designed for up to 4 Tesla). The CMS solenoid makes up a large portion of the 12,500-tonne weight of the detector. Its 6-m-inner diameter and 13-m-length surrounds the hadronic calorimeter in the CMS barrel region (HB). By bending charged particle's tracks, it enables the measurement of momentum of high-energy charged particles. The solenoid surrounds the inner tracker and calorimeter systems while the muon detectors are located on the outside of the solenoid. A cross-sectional view of the CMS Detector is shown in Figure 3.3.

The CMS detector is the only detector in the LHC complex that was completely assembled on the surface. After assembly and testing above ground, it was disassembled into 15 separate large pieces, in addition to many smaller pieces, and lowered down 100 meters into the experimental cavern. CMS is also the heaviest of the LHC

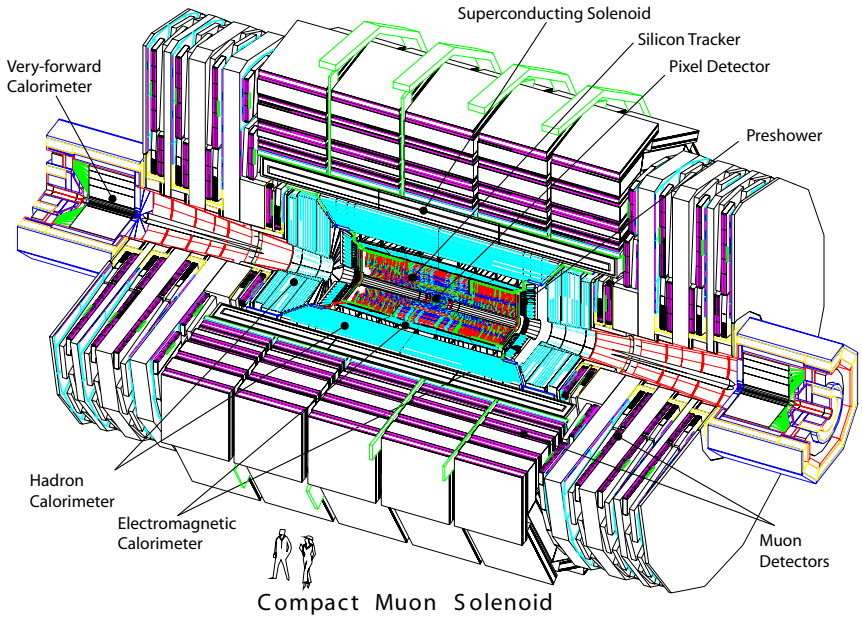

Figure 3.3: Cross-sectional View of the CMS Detector. The subdetectors in order from the interaction point outward are the pixel detector, the silicon tracker, the electromagnetic calorimeter, the hadronic calorimeter, and the muon detectors. The CMS solenoid magnet is located between the hadronic calorimeter and the muon detectors. Electrons, muons, photons, and hadrons are directly detected by the CMS detector and can be fully reconstructed. The image illustrates the subdetectors in which these particles will deposit their energy.

experiments, weighting 12,500-tonnes. It has a 15 m diameter and it is 21.5 m long. While it is almost 2 times heavier than ATLAS, the LHC's largest experiment, it is 1/3 of its size. CMS acquires its name from its high-density design, "Compact", high quality muon system, "Muon", and unique magnet, "Solenoid". The following subsections will give a brief overview of the detector subsystems. A more detailed description of the CMS detector can be found in [3].

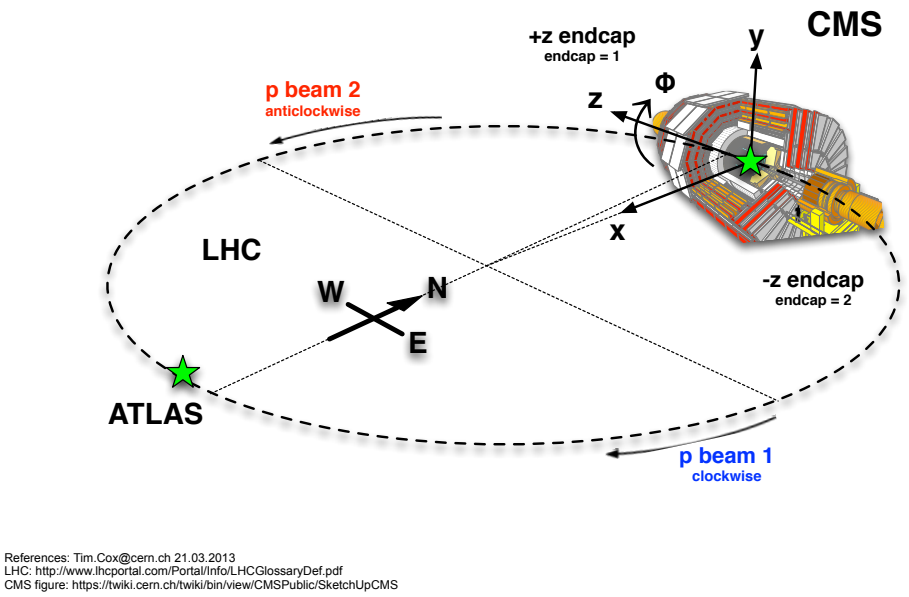

Figure 3.4: CMS Orientation in LHC and Global Coordinates System

3.2.1 The CMS Coordinate System

The CMS coordinate system, shown in Figure 3.4., is a right-handed coordinate system with its origin is at the nominal collision point inside the detector. The y-axis points vertically upward, the x-axis points radially inward towards the center of the LHC and its z-axis points along the anticlockwise-beam direction. The azimuthal angle, ϕ is measured in the x-y plane from the x-axis. The radial component of the x-y plane, measure from the center of the beamline, is denoted by r. The polar angle, θ is measured from the positive z-axis. However, at hadron colliders, a more convenient variable is often used, the pseudorapidity, η instead of θ. Pseudorapidity is defined as $\eta = -ln(tan\frac{\theta}{2})$. We measure the x and y components of momentum and energy to compute the momentum and energy in the transverse plane (perpendicular to the direction of the beam), p_T and E_T respectively.

3.2.2 The Trigger

For the design luminosity of the LHC, $10^{34} cm^{-2} s^{-1}$, an average of 20 overlapping proton-proton interactions are expected for every 25 ns bunch crossing. Each collision produces approximately 1000 particles, which translate roughly to 100MB of data. Due to computational limitations we can neither store nor process all data coming from collisions. Therefore, it is necessary to develop an online event selection process, referred to as the *trigger*, to ensure that potentially interesting events are recorded with high efficiency. The CMS trigger system is composed of the first level trigger (L1), implemented in the detector electronics, and the high-level trigger (HLT), implemented on a computer farm. Due to the good time resolution of the detector and the synchronization readout modules of the subsystems, the L1 trigger is able to select the most interesting events in a fixed time interval of 3.2μs. To achieve reduction from 40 MHz to an output rate of 30-100 kHz, the L1 trigger uses information from the calorimeters, muon systems, and global trigger processors. Once the L1 trigger reduces the rate, the events are processed by the HLT. The HLT uses nearly all offline-quality reconstruction to take advantage of the full detector information and data readout and decrease the event rate to around 100 Hz.

3.2.3 The Tracking System

The ambitious physics program of the CMS detector requires a tracking system that provides efficient reconstruction of the trajectories of charged particles as well as good impact parameter and momentum resolutions. Tracks are used to reconstruct primary and secondary vertices. A full-silicon tracking system located in the innermost part of the CMS detector. The tracker system surrounds the interaction point and has a length of 5.8 m and diameter of 2.5 m. It is composed of the pixel detector,

located closest to the interaction point, and the silicon strip detector, surrounding the pixel detector. The pixel detector is responsible for the accurate reconstruction of impact parameters and primary and secondary vertices while the silicon strip detector provides excellent reconstruction of charged particle trajectories prior to their interaction with calorimeter material. While the tracker's proximity to the point of interaction is beneficial for the functions of its subsystems, it also poses some design challenges. The tracker's material and electronic components must be able to:

- Withstand severe radiation damage due to high particle flux over a 10-yr lifetime
- Function in a high magnetic field environment since the CMS Solenoid provides a homogeneous magnetic field of 3.8 Tesla
- Reliably operate at high track multiplicities to identify individual particle trajectories and have fast enough response to attribute them to their correct bunch crossing.

The tracker system must cope with the highest particle occupancies since it is the subsystem closest to the point of interaction. For the design luminosity of the LHC, $10^{34} cm^{-2} s^{-1}$, an average of 1000 particles from more than 20 overlapping proton-proton interactions are expected in every 25 ns bunch crossing. While high granularity is required for the needed functionalities of the tracker system, an additional challenge is to keep the amount of material to a minimum in order to reduce the resolution degradation due to charged particle multiple scattering, bremsstrahlung, photon conversions and nuclear interactions. The design of the CMS's tracking system that combines the silicon pixel detector and the silicon strip detector, has been optimized to balance these requirements by taking advantage of a silicon design's fast response and high granularity.

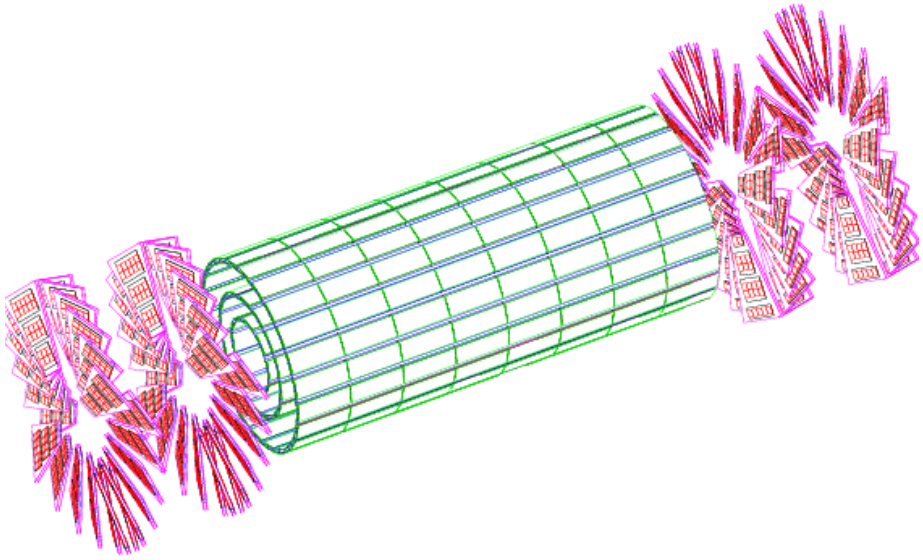

Figure 3.5: CMS Pixel Detector Geometry. The silicon pixel detector is located closest to the interaction point and is composed of three layers of silicon pixels and two endcap disks. It covers up to $|\eta| < 2.5$ and has a spatial resolution of 15 μm

The silicon pixel detector is made of 3 layers of silicon pixel detectors and two endcap disks placed close to the interaction region. It covers the region 4-15 cm in radius around the beam directions. The pixel detector layout is shown in Figure 3.5. Each pixel is 100 μm $\times$ 150 μm in order to achieve similar track resolution in both the r-ϕ and z directions. It provides a coverage up to $|\eta|$ <2.5 and has a spatial resolution of $\sim$ 15μm. The Lorentz drift due to the 3.8 T magnetic field leads to a spreading of the collected ionization charge over more than one pixel. Evidence of two or more hits per track in the pixel detector allows for the measurement of the impact parameter of charged-particle tracks, as well as the position of secondary vertices. This function is necessary for the efficient identification of b-quarks, which is needed in many of the interesting physics channels.

The silicon strip detector surrounds the pixel detector and makes up the rest of the tracker volume. It is composed of 10 layers of silicon microstrip detector in the

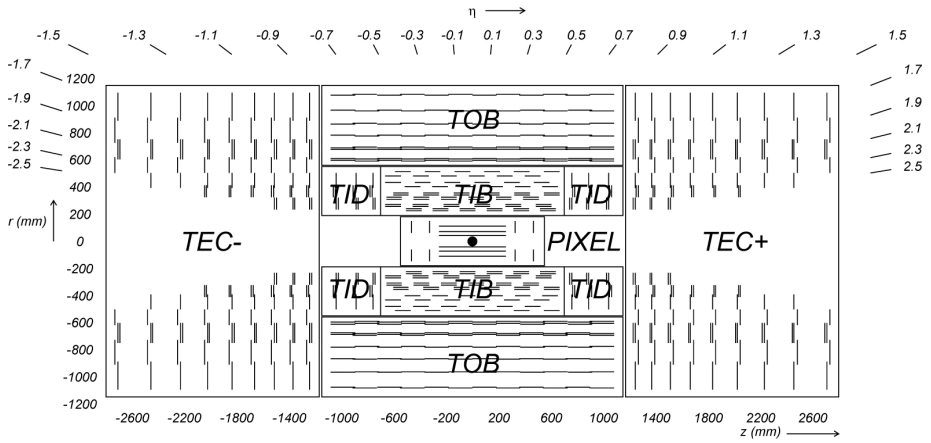

Figure 3.6: Layout of the CMS Tracker. The CMS silicon tracker system consists of the Tracker Inner Barrel (TIB), the Tracker Inner Disks (TID), the Tracker Outer Barrel (TOB), and the Tracker End Caps (TEC). It covers $|\eta| < 2.5$.

barrel region and two endcaps made up of 12 disks. The barrel is divided into the Tracker Inner Barrel (TIB), composed of 4 silicon strip layers and covering up to $|\eta| < 1.4$, and the Tracker Outer Barrel (TOB), composed of 6 silicon strip layers and covering $|\eta| < 1.8$. Similarity, the endcap is divided into the Tracker End Caps (TEC), with 9 disks and covering $1.0 < |\eta| < 2.5$, and the Tracker Inner Disks (TID) systems, with 3 disks and covering $1.2 < |\eta| < 2.1$. The *inner* systems have silicon sensors with 320 μm and the *outer* systems have sensors with 500 μm thickness. The sensor strip pitches vary from 80 to 120 μm in both cases. The silicon strip tracker illustration is shown in Figure 3.6.

The CMS inner tracker system provides a robust, efficient, and precise reconstruction of charged particles with $p_T > 1$ GeV and $|\eta| < 2.5$. It has a momentum resolution of $\sim 0.7\%$ at $|\eta| \approx 0$ increasing to 2% at $|\eta| = 2.5$ for single muons with transverse momenta of 10 and 100 GeV (Figure 3.7). The impact parameter resolution is 150 μm. In addition to meeting the physics needs for offline analysis, the tracker also plays an important role in the High Level Trigger (HLT) selections.

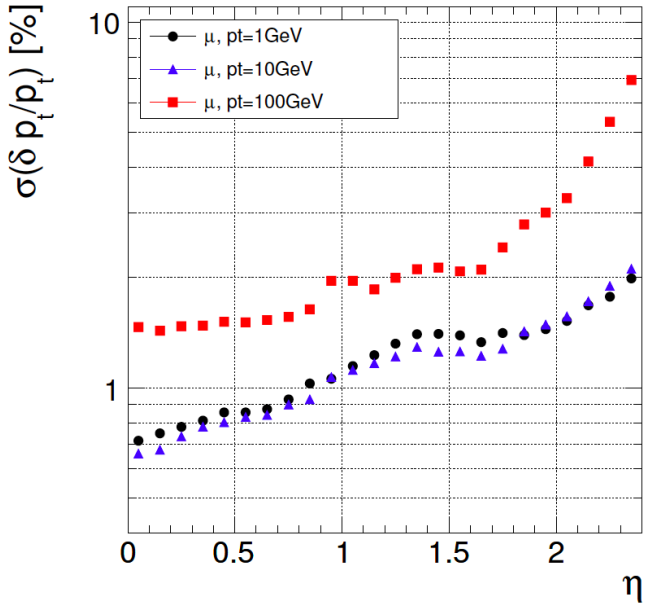

Figure 3.7: Momemtum Resolution for Reconstructed Muons. The CMS tracking system plays an important role in the reconstruction of muon candidates. To measure the performance of the tracking system, the transverse momentum resolution for reconstructed muons with various p_{T}'s (1, 10, and 100 GeV) is shown [3]

.

Tracking information is instrumental in the ability to reduce the rate of events from 40 MHz to 100 Hz.

3.2.4 The Electromagnetic Calorimeter

The CMS Electromagnetic Calorimeter is responsible for the identification and measurement of photons and electrons. It is a nearly hermetic homogeneous calorimeter surrounding the inner-tracker system and composed of 75848 lead tungstate ($PbWO_4$) crystals. The ECAL barrel (EB) covers the region up to $|\eta| = 1.48$ and consists of 36 supermodules. Each supermodule is made of 1700 tapered $PbWO_4$ crystals with a frontal area of approximately 2.2×2.2 cm^2 and a length of 23 cm.

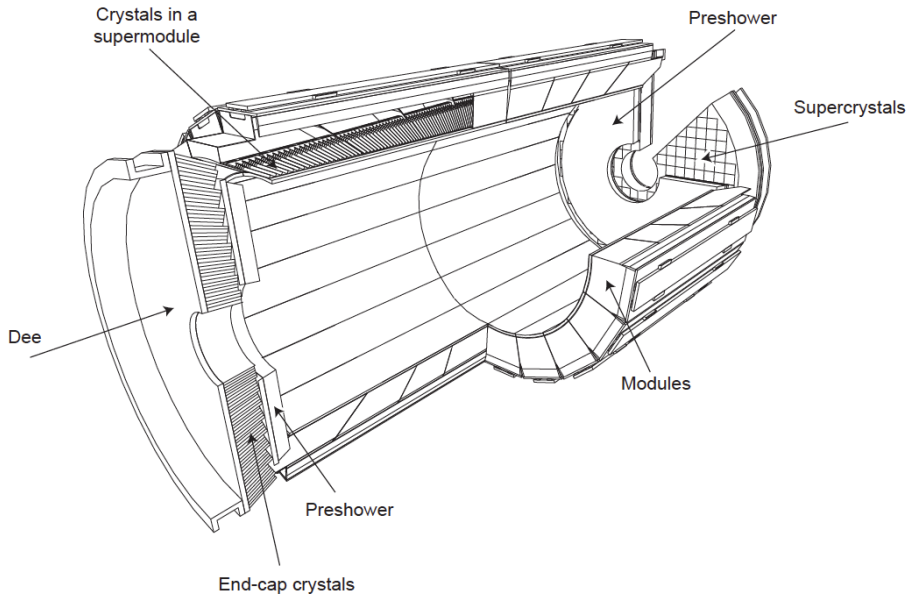

Figure 3.8: Electromagnetic Calorimeter (ECAL) Layout. The ECAL is composed of the ECAL Barrel (EB), the ECAL Endcap (EE), and the ECAL preshower detectors. It covers up to $|\eta| < 2.6$ with a gap between the EB and the EE at $1.4 < |\eta| < 1.6$.

The ECAL endcaps (EE) are composed of four half-disks (Dees). Each half-disk consists of 3662 tapered crystals with a frontal area of 2.64×2.68 cm^2 and a length of 22 cm. In addition to EB and EE, the ECAL system has preshower detectors, located in front of the ECAL endcaps. The preshower detector is a two layer detector composed of lead radiators and silicon strip sensors. It covers the region of $1.653 < |\eta| < 2.6$. It is used to distinguish electrons and photons from π^0's. A schematic view of the ECAL is shown in Figure 3.8.

The $PbWO_4$ crystal were chosen due to their radiation tolerance and ability to provide fast response and excellent energy measurement resolution. When high energy electrons and photons enter the ECAL, they interact with the material and generate electromagnetic showers. The advantage of $PbWO_4$ crystals is their short scintillation decay times, $\sim 80\%$ of the light is emitted within 25 ns. However, they

also have a relatively low light yield, requiring the use of avalanche photodiodes (APDs) in the barrel region and vacuum phototriodes (VPTs) in the endcaps to collect the scintillation light from the crystals. Another challenge of this system is to achieve the desired energy resolution, $\leq 1\%$ for high photon and electron energies, to be sensitive to $H \rightarrow \gamma\gamma$. The ECAL energy resolution is a function of many factors, including:

1. Event to event fluctuations in lateral shower containment, photo-statics and photodectector gain
2. Electronics Noise and Event Pile-Up
3. Non-uniformity of the longitudinal light collection
4. Leakage of energy from the rear face of the crystal
5. Accuracy of the detector inter-calibration constants.

The ECAL design takes into account 1-4. The effects due to inter-calibration constants are accounted for by using offline calibrations, e.g. [58]. One other challenge is the temperature dependence of the crystal light yield and the sensitivity of the APD gains to variations in both temperature and high voltage. This requires the ECAL detector temperature to be kept at a stable 18°C with a precision of 0.05% and stability of the high voltage applied to the APDs.

3.2.5 The Hadronic Calorimeter

The CMS Hadronic Calorimeter (HCAL) provides a measurement of energy and direction for neutral hadrons. Together with the ECAL and Muon systems, it is used in the identification of electrons, photons, and charged and neutral hadrons. The

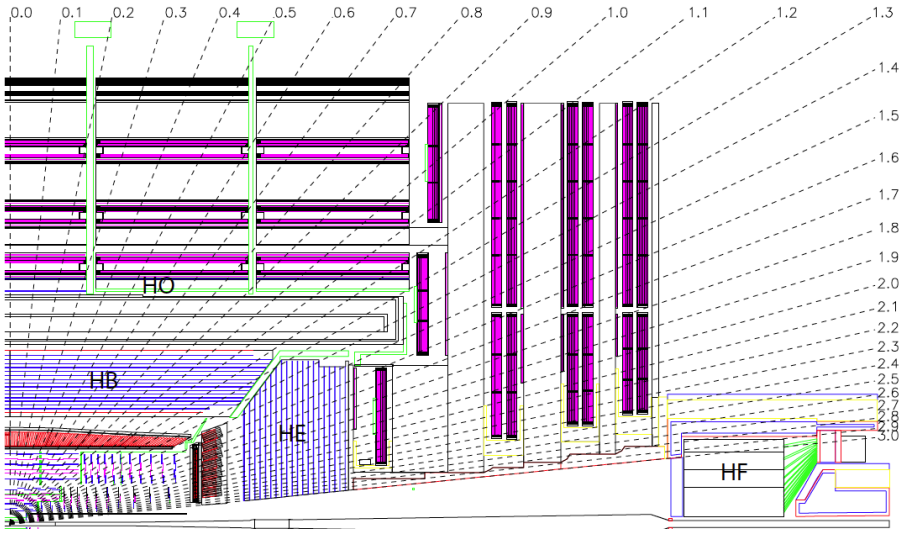

Figure 3.9: Layout of the Hadronic Calorimeter. The Hadronic Calorimeter (HCAL) consists of the HCAL Barrel (HB), the HCAL Endcaps (HE), the Outer HCAL (HO), and the Forward HCAL (HF). It covers up to $|\eta| < 5.0$.

HCAL provides small energy leakage by including central, outer, and forward systems. These systems are sampling calorimeters composed of layers of non-magnetic absorber material (copper alloy and stainless steel) with tiles of plastic scintillator in between. When the hadronic particle interacts with the absorber material, it creates a shower, which is then detected with the plastic scintillators.

The primary sections of the HCAL are the HCAL Barrel (HB) and the HCAL endcaps (HE). The longitudinal view of these systems is shown in Figure 3.9. HB and HE are located in between the ECAL and the solenoid magnet between radius R = 1.77 - 2.95 m. HB is divided into two half-barrels (HB+ and HB-). It is composed of a total of 36 identical azimuthal wedges covering a pseudorapidity range $|\eta| < 1.3$. Figure 3.10 shows the numbering scheme of the wedges, which are aligned parallel to the beam axis. The wedges are made of 8 flat brass absorber plates (50.5 mm thick) and the innermost and outermost plates are made of stainless steel (40 mm thick

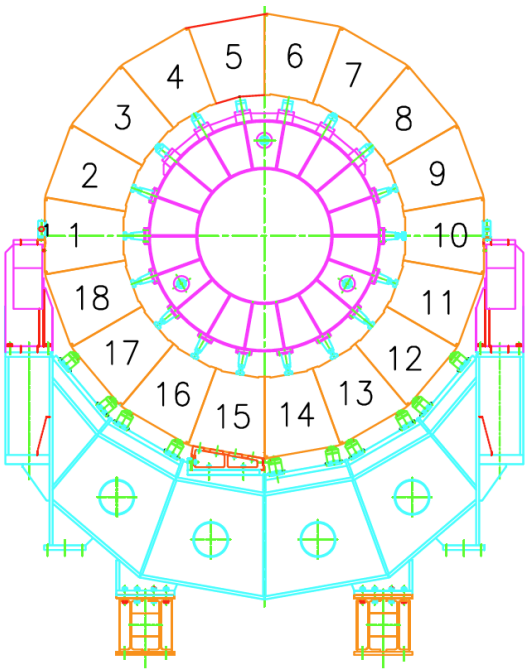

Figure 3.10: Numbering Scheme for HCAL Barrel Wedges. The Wedges are made out of flat brass absorber plates.

and 75 mm thick), for structural strength. The channel segmentation of the HB is $(\Delta\eta \times \Delta\phi) = (0.087 \times 0.087)$. To complete the near-$4\pi$ coverage, the HE is inserted into the ends of the solenoid magnet. It covers $1.3 < |\eta| < 3.0$, a region containing $\sim 34\%$ of the produced particle flux. The key challenges taken into account in the design of the system are: to overcome the high particle flux, heavy radiation, and high magnetic field environment without compromising energy resolution. The HE is constructed of brass plates of 79 mm thickness with 9 mm thick scintillators that are supported by 10 cm thick stainless steel outer layers. The granularity of the HE is $(\Delta\eta \times \Delta\phi) = (0.087 \times 0.087)$ for $|\eta| < 1.6$ and $(\Delta\eta \times \Delta\phi) \approx (0.17 \times 0.17)$ for $|\eta| \geq 1.6$.

The outer HCAL (HO) was added outside the solenoid magnet to increase the sampling depth of HCAL in order to provide sufficient containment of hadronic

showers [59]. It covers the pseudorapidity range of $|\eta| < 1.3$, where there is not enough sampling depth to completely contain occasional very high energy hadronic showers. The addition of HO is useful to decrease the leakage of hadronic shower energy, which has a direct effect on the missing transverse energy measurement. The HO uses a solenoid coil as an additional absorber to improve the identification of late starting showers and to measure hadronic shower leakage. The granularity for HO is also $(\Delta\eta \times \Delta\phi) = (0.087 \times 0.087)$.

The forward HCAL (HF) detector covers pseudorapidity range $3.0 < |\eta| < 5.0$. HF is located at 11.1 m away from the interaction point was added to improve the measurement of the missing transverse energy and to enable identification and reconstruction of very forward jets. Very forward jets are important signatures of interesting physics processes, such as the study of Vector Boson Fusion (VBF) Higgs production, which plays an important role in searches for the higgs boson and follow-up studies on its properties. HF can also be used to calculate the real-time relative instantaneous luminosity [3]. To account for the particle fluxes, almost 8 times higher than the rest of the CMS detector, radiation hard quartz fibers are used as active material. The fibers are inserted inside 5 mm thick grooved plates, which make up the HF steel absorber structure. The HF has granularity of $(\Delta\eta \times \Delta\phi) = (0.175 \times 0.175)$.

3.2.6 The Muon System

One of the "golden" channels for SM Higgs decay is $H \rightarrow ZZ \rightarrow 4\mu$ due to the relative ease in the reconstruction and identification of muons. The study of this golden channel and of other interesting scenarios with muon final states require precise and robust muon identification, momentum measurement, and triggering with a wide angular coverage. The muon system is composed of three types of gaseous particle

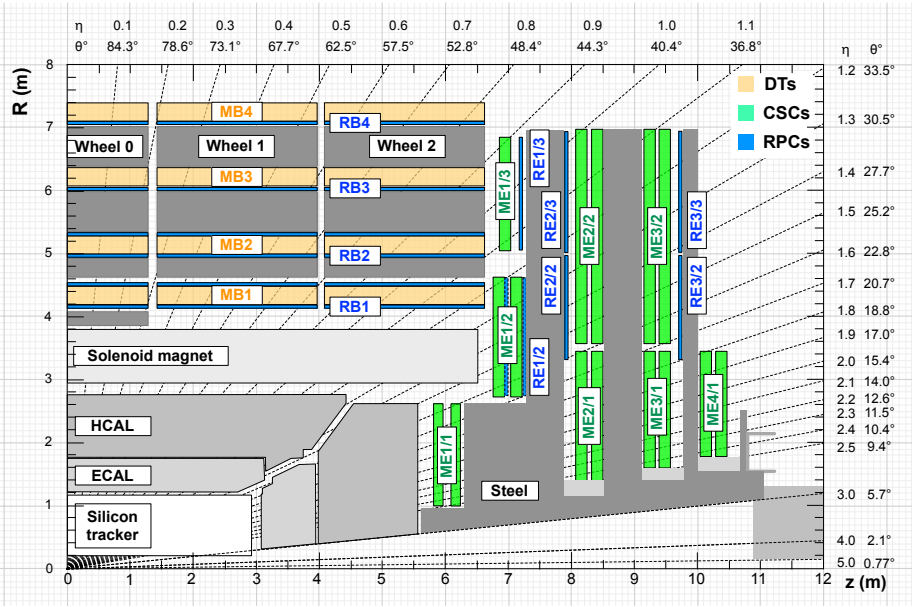

Figure 3.11: The CMS Muon System. CMS quadrant showing Drift Tubes chambers in orange, Cathode Strip Chambers in green, and Resistive Plate Chambers in blue. The Muon System covers up to $|\eta| < 2.4$.

detectors located at the outermost parts of the CMS detector. They are embedded in the iron return yoke outside the magnet, which together with the high field solenoid magnet enables good muon momentum resolution and trigger capability. The drift tube (DT) chambers, covering a pseudorapidity of $|\eta| < 1.2$, are located in the barrel region and the Cathode Strip Chambers (CSC's), which cover $0.9 < |\eta| < 2.4$, are in the endcap region. Additionally, the Resistive Plate Chambers (RPCs), covering $|\eta| < 1.6$, are included in both, the muon barrel and endcaps, to improve timing resolution. Figure 3.11 shows a schematic view of the muon detectors.

The DT chambers are divided into 4 stations in the barrel region forming concentric cylinders around the beamline. The 3 inner cylinders have 60 drift chambers each and the outer cylinder has 70. The DT system is made of ∼172,000 stainless-steel wires with a wire length of 2.4 m and aluminum cathodes. In the 3 inner stations,

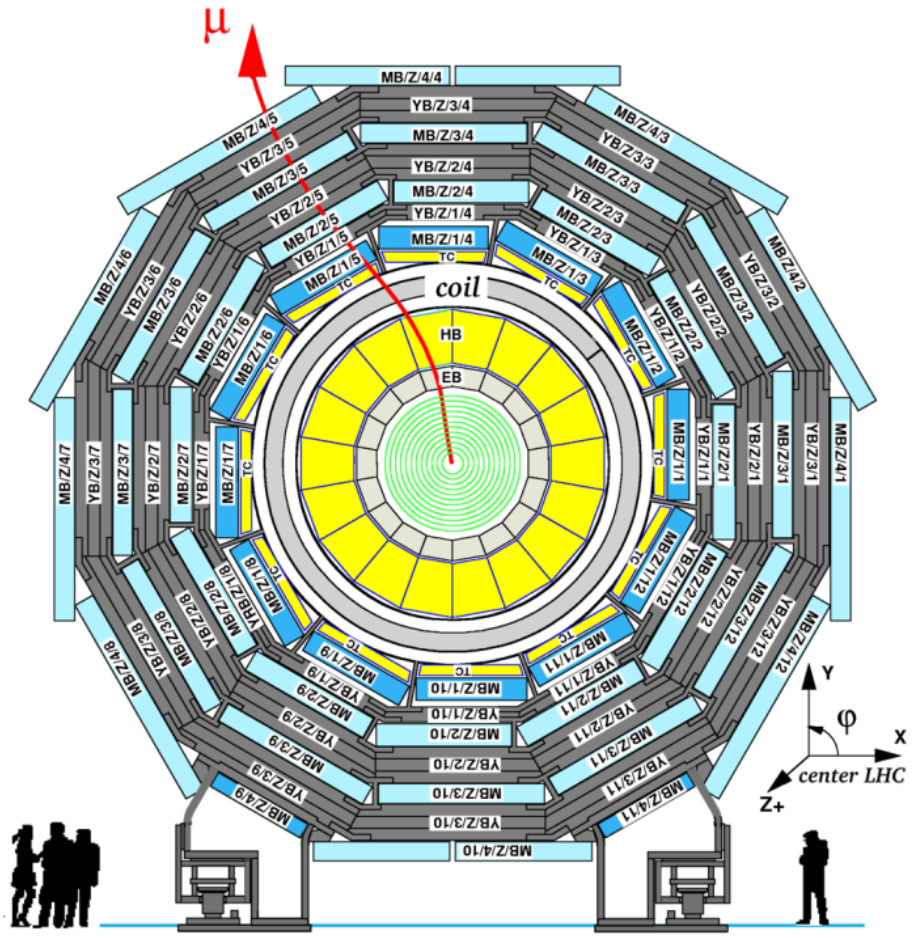

Figure 3.12: Muon Drift Tube Layout. The Barrel is made out of 5 wheels of Drift Tube chambers. The illustration shows the muon Drift Tube chambers in one of the 5 wheels.

each DT chamber is made of 3 superlayers (SL). The muon track measurement in the magnetic bending plane (r-ϕ) is provided by the 2 outer SLs that are parallel to the beam line. The inner SL measures the z position, which is orthogonal to the beam line. The fourth only has the 2 SLs parallel to the beam line. The gas mixture used for the drift cells is 85% Ar + 15% CO_2. Figure 3.12 shows a cross-sectional view of the muon DT barrel system.

The muon endcaps house the 473 Cathode Strip Chambers (CSCs). The CSCs

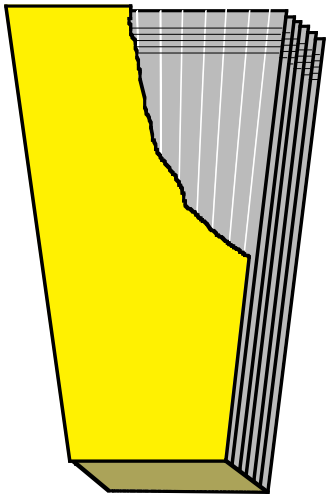

Figure 3.13: Layout of a Cathode Strip Chamber (CSC). The Muon Endcap is composed of 473 CSCs. The illustration shows the strip and wire orientation for the CSCs (with the exception of the ME1/1 CSCs).

are arranged into 4 stations on each endcaps with

- 72 ME1/1, 72 ME1/2, and 72 ME1/3 CSC detectors on station 1
- 36 ME2/1 and 72 ME2/2 CSC detectors on station 2
- 36 ME3/1 and 72 ME3/2 CSC detectors on station 3
- 36 ME4/1 and 5 ME4/2 CSC detectors on station 4

The CSCs are trapezoidal multiwire proportional chambers made of 6 anode wire planes between 7 cathode strip panels and placed between the iron disks. The strips run radially in the endcap geometry and provide the ϕ coordinate for muon hits. Wires run perpendicular to the strips and provide the radial coordinate. A schematic of CSC cathode strips and anode wires is shown in Figure 3.13.

Since the ME1/1 CSCs are subjected to a high 2.7 - 3.0 T B_z-field, the wires are tilted at a 29° angle to compensate for the skewed drift of electrons. The chambers

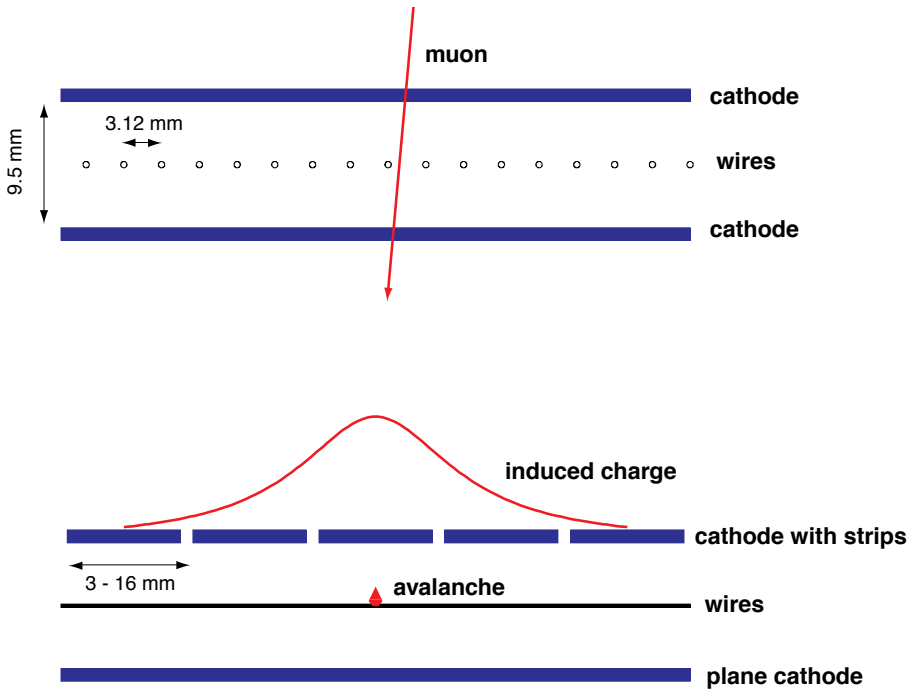

Figure 3.14: Muon Detection in the CSCs. The illustration shows a muon going across CSC wires (top) and inducing a charge on the cathode strips (bottom).

are filled with a gas mixture of 40% Ar + 50% CO_2 + 10% CF_4. When a muon hits a CSC, an avalanche is developed on the wires which then induces a distributed charge on the cathode with a well-defined shape (shown in Figure 3.14). By using the position of the induced charge in the cathode strips, one can reconstruct the track position along a wire. The closely spaced wires of the CSCs make it a fast detector.

The CSCs play a crucial role in the first-level muon trigger due to their:

- $\geq$ 99% efficiency per chamber for finding tracks
- $\geq$ 92% probability per chamber for identifying the correct bunch crossing. Since all the CSCs, except ME1/3, overlap in the ϕ direction, a muon track will cross 3-4 CSCs and be assigned the correct bunch crossing number in at least 99% of the cases.

- CSC electronics provides robust pattern recognition for rejection of non-muon backgrounds and efficient matching of hits to those in other stations and to the CMS inner tracker.

- 2 mm resolution in r-ϕ

In addition, the offline spatial resolution in r-ϕ of the CSCs is $\sim 74\mu$m for ME1/1 and ME1/2 chambers while 150 μm for all others. The momentum measurement resolution of the standalone CMS muon system is 8-15% for a muon with p_T = 10 GeV/c and 20-40% for a muon with p_T = 1 TeV/c. The global muon reconstruction, which adds information from the inner-tracker system, improves the momentum resolutions to 1.0-1.5% for a muon with p_T = 10 GeV/c and 6-17% for a muon with p_T = 1 TeV/c [60].

In addition to the DT and CSCs, the Resistive Plate Chambers are also part of the muon system. An RPC module consists of two parallel phenolic resin plates separated by a gas gap. The resin plates are coated with conductive graphite paint to form electrodes, and readout is made by means of aluminum strips outside the resin plates. The gas mixture for these detectors is 96.2% R134a ($C_2H_2F_4$), 3.5% iC_4H_{10} and 0.3% SF_6. The RPCs were added to the muon system in order to improve the timing resolution. These features are especially important for triggering in high rate environments. Six layers of RPCs are installed in the barrel region. The efficiency to reconstruct a high p_T muon track with a momentum measurement delivered by the muon system, with DTs and RPCs, alone is better than 95% at $|\eta| < 0.8$. In the endcap, there are 3 RPC stations (RE 1-3) whose locations are shown in Figure 3.11. The chambers are of trapezoidal shape and they overlap in ϕ as to avoid dead space at chamber edges.

4. EVENT RECONSTRUCTION AND OBJECT IDENTIFICATION

The event reconstruction used for the offline analysis of the data collected by the CMS detector is performed within the CMS software (CMSSW) framework. For each event, we reconstruct all particles and their momentum by using lower level objects, e g. calorimeter energy clusters or charged tracks. Stable particles (e.g. electrons and muons) or particles that decay into stable particles (e.g. jets and τ-leptons) reconstructed with a variety of sophisticated reconstruction algorithms. The properties of the reconstructed events are used to model the final selections (i.e. particle identification, calorimeter and track isolation, etc.) which optimize signal significance for different physics analysis, as will be described in the next chapter.

The analysis presented in this thesis uses the CMSSW_4_2_3 software release version. In this chapter, we will describe the reconstruction algorithms, compatible with this CMSSW release, for the physics objects that played a primary role in our search.

4.1 Muons

Muon reconstruction in CMS is completed by gathering information from the silicon tracker and the muon subsystems: drift tube chambers (DTs), Cathode Strip Chambers (CSCs), and Resistive Plate Chambers (RPC). As described in the previous chapter, these systems cover almost a 4π solid angle around the point of interaction and provide excellent spatial resolution. Muons are first locally reconstructed by identifying hits in the detection layers of each muon chamber and applying the pattern-finding algorithms of the muon subsystems. A linear fit between position of hits in each layer is used to construct *seeds*, position and direction vectors of a muon candidate in a chamber. The seeds are used to reconstruct *standalone muons* by us-

ing a Kalman Filter [61], mathematically equivalent to a least squares fit, to match hits from the innermost muon measurement to all other hits in the muon chambers. For each standalone muon, the innermost muon measurement of the standalone muon is matched to the outermost measurement of reconstructed tracker tracks. Using a Kalman Filter, the best matching track is selected for the reconstruction of a *global muon*. A final Kalman filter is used to fit all hits in both, the standalone muon track and the best matching tracker track, to complete the reconstruction of the global muon candidate. Combining the silicon tracking information with the muon subsystem reconstruction, i.e. Global muon reconstruction, improves the momentum measurement resolution over the standalone muon reconstruction. In addition to allowing to measure muon p_{T} well, it also reduces the probability for other objects to be misreconstructed/misidentified as muon candidates.

For **Muon Identification** in the μ final states included in this analysis, we use a subset of global muons passing the "Tight Muon Selection":

- ≥ 1 μ chamber hit included in the global-muon track fit
- ≥ 1 μ with tracker hits ≥ 10
- ≥ 1 μ with ≥ 2 matching segments (muon station hits)
- ≥ 1 μ with $\chi^2/\mathrm{ndof} < 10$
- ≥ 1 μ $|d_0| < 0.2$ cm, where d_0 is the transverse impact parameter with respect to the primary vertex.

As seen in Figure 4.1, muon reconstruction for the tight muon selection varies between 92% and 96% for μ's with $p_{\mathrm{T}} > 20$ GeV/c (the p_{T} threshold for this search).

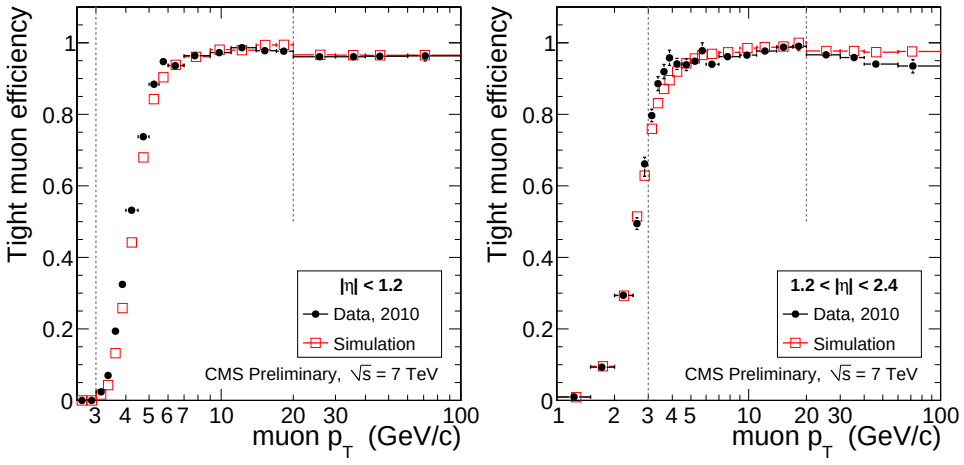

Figure 4.1: Efficiency for Tight Muon Selection. Shown is the muon "tight" selection efficiency as a function of muon p_{T} in 2010 data ($\mathrm{L}_{int} = 40pb^{-1}$) measured using the tag-and-probe technique to muons from $\mathrm{J}/\psi \to \mu\mu$ and from $\mathrm{Z} \to \mu\mu$ in the range of $p_{\mathrm{T}} < 20$ GeV for the barrel region (left), $|\eta| < 1.2$, and the endcap region (right), $1.2<|\eta|<2.4$. The Tight Muon Selection is used in many CMS physics analysis. [4]

4.2 Electrons

CMS electrons are reconstructed using information from the pixel detector, the silicon strip tracker and the electromagnetic calorimeter (ECAL). In this section, the ECAL seeded reconstruction algorithm will be explained as well as the components of the common electron identification algorithms used in CMS analyses.

4.2.1 ECAL Seeded Reconstruction

Electrons (or photons) reaching the ECAL will deposit their energy in an array of crystals. During test beam tests, electrons where shown to deposit the majority of their energy into simple fixed sized arrays of crystals [62]. However, in the case of the CMS detector, the electrons must transverse the tracker material before reaching the ECAL. As they pass through the tracker, and their paths are bent by the magnetic

field, the electrons will radiate photons. Once they reach the ECAL, their full energies will no longer be deposited into simple fixed arrays of crystals but instead will suffer large loses through the electron trajectory in the tracker. For about 35% of the electrons, less than 30% of their energy will reach the ECAL [5]. In addition, the Bremsstrahlung will cause the electron energy reaching the ECAL to have a large spread in the ϕ direction.

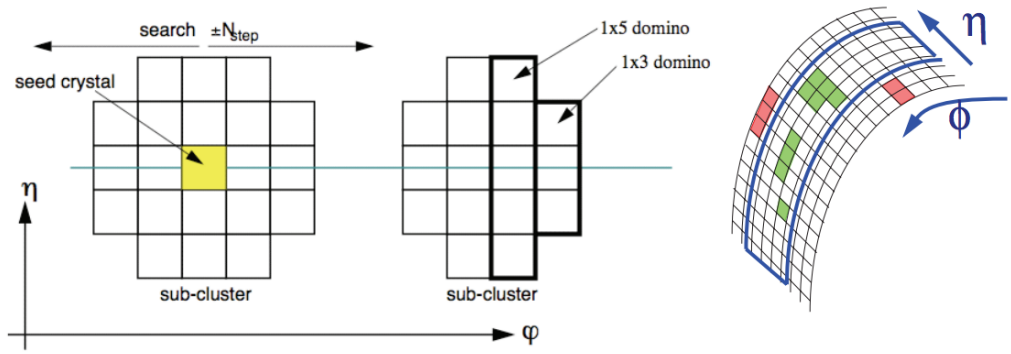

Figure 4.2: An Illustration of the Hybrid Clustering Algorithm. The hybrid clustering algorithm is used for the reconstruction of electrons in the barrel. It creates clusters by combining contiguous 1×5 and 1×3 dominos around a local maxima (shown on the left) and searches for a narrow spread in the η direction with a wide spread in ϕ (shown on the right).

A supercluster-driven, pixel-seed finding, GSF track reconstruction algorithm has been designed to fully reconstruct electron candidates in the CMS detector. The creation of *superclusters* through the Hybrid (barrel electrons) and Island (endcap electrons) clustering algorithms [63] has been designed to take into account the spread in ϕ in order to collect the radiated energy and minimize the cluster containment variations. The clustering algorithms first search for crystals above a certain threshold energy to utilize as *seed crystals* in both the ECAL barrel and endcap regions. The

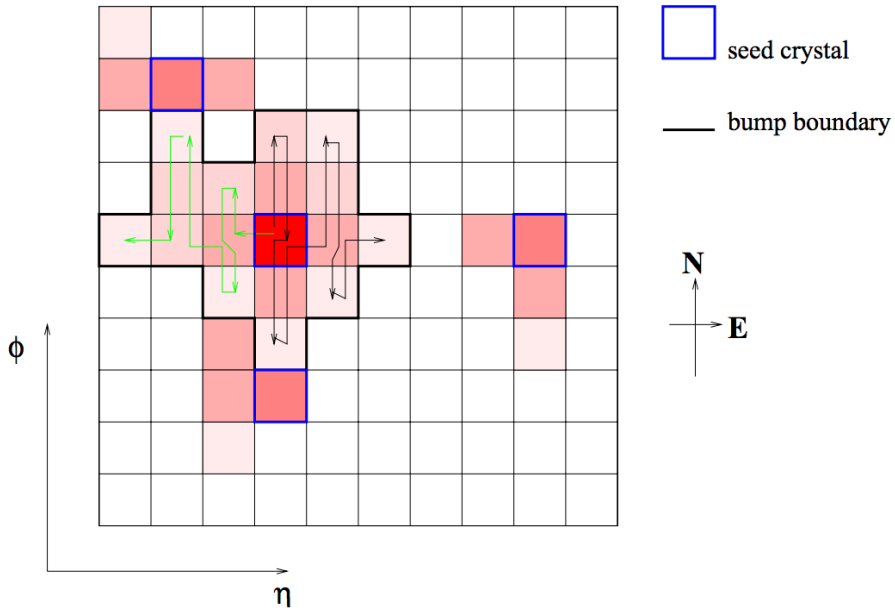

Figure 4.3: An Illustration of the Island Clustering Algorithm. The island clustering algorithm is used in to reconstruct electrons in the endcap. It groups rows of crystals containing energies decreasing monotonically as moving away from the seed crystal.

Hybrid cluster algorithm exploits the $\eta - \phi$ geometry of the barrel crystals to search for the lateral shower shape in the η direction while searching for separated energy in the ϕ direction. Seed clusters are constructed from contiguous dominoes made of 3-5 crystals in η whose energy is $\geq$ 100 MeV and originate from a seed crystal. A group of dominoes makes up a Hybrid supercluster. An illustration of the Hybrid clustering algorithm is shown in Figure 4.2. In the endcap, the Island clustering algorithm forms clusters by connecting rows of crystals containing energies decreasing monotonically as moving away from the seed crystal. Using the bremsstrahlung recovery procedure, it builds superclusters by collecting other island clusters in a ϕ road. An illustration of the Island clustering algorithm is shown in Figure 4.3.

ECAL superclusters and pixel hits are used to generate seeds for electron trajectory building in the first step of the electron track reconstruction. A seed is generated

when 2 pixel hits compatible with the beam spot are extrapolated from the superclusters by applying the supercluster-driven pixel matching algorithm used in the HLT [62]. The seeds are restricted to a region best matching the supercluster in the ECAL. This region is determined by the assumption that the electron resulting in the ECAL superclusters has the same impact point as a non-radiating electron of the same initial momentum. The energy weighted mean position of the supercluster is propagated towards pixel detector hits, taking into account the magnetic field. The supercluster is matched to the innermost measurement in the pixel detector that falls within a specified loose $\Delta\phi$ window and Δz interval. Then the first pixel hit and the ECAL supercluster information are used to propagate to the second pixel hit in order to create the seed.

The generated pixel-seeds are used to reconstruct the electron trajectory in the silicon strips using the Gaussian Sum Filter (GSF). A Bethe Heitler modeling is used to model Bremsstrahlung energy loss. Since energy distributions of electrons are highly non-Gaussian due to the bremsstrahlung energy loss as they propagate through matter, a Kalman Filter cannot be used to build the electron trajectory as is done for the muons. The electron tracks are best described by a Gaussian mixture rather than by a single Gaussian, thus we use a Gaussian Sum Filter for the reconstruction of electron tracks. Starting from the seed, a trajectory is build by matching to hits in the subsequent silicon tracker layers using the GSF algorithm. In each layer, more than one tracker hit can be found compatible with the previous layer's hit. To avoid the reconstruction of many parallel trajectories, only the best two tracker hits per layer, determined by the smallest χ^2 values, are used for trajectory building. A final requirement of at least 5 hits on the silicon strips is applied to determine the track candidates. The track that best matches the ECAL supercluster, determined by a final GSF fit, is chosen as the reconstructed electron

track.

Loose geometrical and energy-momentum matching pre-selections are imposed on the electron track and the corresponding supercluster after energy scale corrections are applied [63]. The energy-momentum matching is measured by taking the ratio of the corrected supercluster energy, E_{corr}, with the track momentum, p_{in}, measured at the closest position from the nominal vertex. The restriction on the geometrical matching is obtained by applying a cut on the difference between the ECAL supercluster parameters, η_{sc} and ϕ_{sc} and the extrapolated track parameters at the interaction vertex, $\eta_{in}^{extrap.}$ and $\phi_{in}^{extrap.}$. A final restriction is imposed on the ratio between the ECAL supercluster energy and the energy deposited in HCAL, which is expected to be small, $(\mathrm{H/E}_m)$.

Electron candidates are required to pass the criteria in Table 4.1. Figure 4.4 shows the absolute efficiency for electron candidates from $H \rightarrow ZZ^* \rightarrow e^+e^-e^+e^-$ after pre-selection [5]. The drop in efficiency at $1.4 \leq |\eta^e| \leq 1.6$ is due to the transition region between the ECAL barrel and the endcaps. The reconstruction efficiency of electrons is largely dependent on the electron track reconstruction and therefore has low efficiency in geometrical areas where tracking is not available. Due to the lack of coverage by the pixel endcap disks, making tracking unavailable, a second drop in efficiency is observed near $|\eta^e| = 2.4$. In addition to this, low p_{T} electrons also have low track reconstruction efficiency due to the high fraction of energy lost through Bremsstrahlung. For these studies, the reconstructed track parameters of the electron were measured at the point closest to the generated vertex.

Table 4.1: Electron Identification. Selections defining the basic electron identification criteria.

A reconstructed electron track must be initiated by the reconstruction of a supercluster in the ECAL matched with hits in the pixel detector
$\mathrm{E}_{corr}/\mathrm{p}_{in} < 3.0$
$\lvert\Delta\eta_{in}\rvert = \lvert\eta_{sc} - \eta_{in}^{extrap.}\rvert < 0.02$
$\lvert\Delta\phi_{in}\rvert = \lvert\phi_{sc} - \phi_{in}^{extrap.}\rvert < 0.15$
$\mathrm{H}/\mathrm{E}_{m} < 0.15$

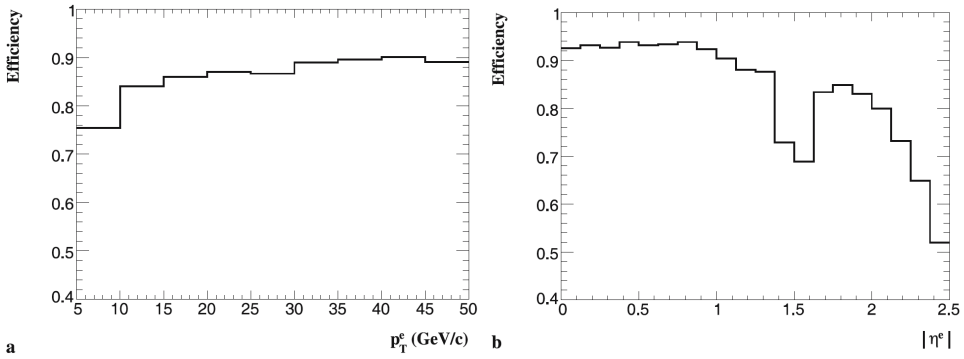

Figure 4.4: Efficiency of Electron Reconstruction. The efficiency for electrons from Higgs boson decays $H \to ZZ^* \to e^+e^-e^+e^-$ ($\mathrm{m}_H = 150$ GeV/c^2) to be reconstructed as a function of electron transverse momentum (left) and electron pseudorapidity (right). [5]

4.2.2 Electron Identification

For this analysis, we will apply tighter criteria to identify the electron candidates for the final states where τ-leptons decay to electrons. In CMS, electron identification is based on the following variables:

- **ECAL driven**, a reconstructed electron track must be initiated by the reconstruction of a supercluster in the ECAL matched with hits in the pixel

detector. Or **Tracker driven**, when tracker seeded reconstruction is used. Tracker seeded reconstruction is useful for low energy electrons whose electron energy is mismeasured due to their very broad calorimeter deposit.

- $|\boldsymbol{\Delta\eta_{in}}| = |\eta_{sc} - \eta_{in}^{extrap.}|$, the difference in pseudorapidity between the energy weighted position of the supercluster and the electron extrapolated track.

- $|\boldsymbol{\Delta\phi_{in}}| = |\phi_{sc} - \phi_{in}^{extrap.}|$, the difference in azimuthal angle, ϕ, between the energy weighted position of the supercluster and the electron extrapolated track at the interaction vertex.

- $\mathbf{H/E_m}$, the ratio between the energy deposited in the hadronic calorimeter within the supercluster area and the energy deposited in the electromagnetic calorimeter, used to describe the longitudinal shower profile

- $\boldsymbol{E_{corr}/p_{in}}$, ratio between corrected supercluster energy, E_{corr} and the track momentum, p_{in}, measured at the closest position from the nominal vertex used to measure ECAL-track compatibility.

- $\boldsymbol{\sigma_{i\eta i\eta}}$, transverse shower profile in the η direction. The difference in η between the seed crystal and the neighboring crystal is weighted by their energy ratio and summed over all crystals in the supercluster (shown in Equation 4.1).

$$\sigma_{i\eta i\eta} = \sum_{crystals} (\eta_{seed} - \eta_i)^2 \times \frac{E_i}{E_{seed}} \tag{4.1}$$

- $\mathbf{E^{n\times m}/E^{m\times m}}$, energy ratio between an array of crystals of size $n \times m$ in the electromagnetic calorimeter and one of size $m \times m$, where n < m, that allows us to measure the spread of the shower in the ECAL.

- $\boldsymbol{f_{brem}}$, the ratio between the momentum difference in the innermost state, measured by the tracker, and outermost state, a combination ECAL, HCAL, and tracker measurements, of the electron track and the inner state momentum
- $\boldsymbol{d_{xy}}$, transverse impact parameter between the track and the primary vertex
- Rejection against electromagnetic pair conversion by requiring 0 missing hits in the inner layer of the tracker and identification of a partner conversion track

The most important variables for electron identification are E_{corr}/p_{in}, $|\Delta\eta_{in}|$, $|\Delta\phi_{in}|$, $\sigma_{i\eta i\eta}$, and H/E. The d_{xy}, missing hits in the innermost tracker, and the identification of a partner conversion track can be used to reject electrons from conversions. The electron observables sensitive to the amount of bremsstrahlung are f_{brem} and E_{corr}/p_{in}. Additionally, the $\mathrm{E}^{n\times m}/\mathrm{E}^{m\times m}$ is a strong variable for the identification of high energy electrons. Since the energy deposits of high energy electrons are narrow then $\mathrm{E}^{n\times m}/\mathrm{E}^{m\times m} \approx 1$.

4.2.3 Electron Isolation

Electron isolation is calculated using tracker, HCAL, and ECAL information. Isolation is defined by placing a small cone around the energy deposit from the signal, known as the signal cone. A larger cone, the isolation cone is then placed around the signal cone. The sizes of the signal and isolation cone are optimized for different analysis. In addition, you can impose threshold requirements on the isolation candidates, particles that fall between the isolation cone and the signal cone, or the isolation region. For ECAL isolation, the signal cone is drawn around the supercluster with the highest energy deposit. ECAL isolation is the defined as the sum of the transverse energy of the photon candidates, above a defined threshold,

that fall in the isolation region. For HCAL isolation, we take the transverse energy sum of the HCAL hits above a defined threshold. Finally, for track isolation, the signal cone is placed around the electron track candidate. The track isolation is the sum of the p_{T} of tracks above a defined threshold in the isolation region. Relative isolation (Equation 4.2) or absolute isolation, which measures the amount of energy surrounding the electron candidate, can be used to discriminate against electrons coming from heavy flavor decays or conversions, as is the case in QCD-multijet events.

$$I^{e}_{rel} = \frac{\Sigma p_{\mathrm{T}}^{track} + \Sigma E_{\mathrm{T}}^{ECAL} + \Sigma E_{\mathrm{T}}^{HCAL}}{p^{e}_{\mathrm{T}}} \tag{4.2}$$

In the analysis presented in this thesis, absolute isolation is applied (ECAL and track isolation).

4.3 Particle Flow Reconstruction

For the search of heavy resonances with opposite-sign τ-leptons, it is crucial to have a reconstruction method that will provide high quality reconstructed τ_h candidates with good p_{T} resolution and a precise measurement for missing transverse energy, $\not\!\!E_{\mathrm{T}}$ (Section 4.7), to account for the neutrino energy in τ decays. Efficient and robust τ_h reconstruction is important for background rejection against SM processes with hadronic jets, whose cross-section is $\sim 10^6$ times higher than τ_h cross-section. Good p_{T} and $\not\!\!E_{\mathrm{T}}$ resolution are needed for the reconstruction of the ditau mass, a key feature in our analysis that uniquely helps to separate our signal from background (more details in Section 4.7). The reconstruction algorithm must also quantify charged lepton isolation for the cases where the τ-lepton decays into electrons and muons to reduce the contamination from events with jets faking leptons

in the final analysis selections. Finally, the efficient identification of b-jets is also a requirement for our analysis since we employ b-jet vetoes to reduce backgrounds from top decays. The Particle-Flow (PF) framework provides high level reconstruction algorithms that meet the physics needs for the search presented in this thesis. Furthermore, PF reconstruction is an important part of many physics searches with τ-leptons, $\not\!\!E_{\mathrm{T}}$, and top decays, all key signatures to many proposed scenarios of physics beyond the SM.

4.3.1 Particle Flow Algorithm

The PF algorithm must provide a global, coherent, and accurate event description for the reconstruction of particle-based objects, such as jets, $\not\!\!E_{\mathrm{T}}$, τ's, etc. In order to accurately reconstruct and identify as many of the stable particles in a final state as possible, the PF reconstruction algorithm combines information from all CMS sub-detectors. By doing so, it creates mutually exclusive collections of reconstructed PF electrons, muons, photons, and charged and neutral hadrons. In this analysis, PF was used for the reconstruction of τ-candidates and $\not\!\!E_{\mathrm{T}}$. However, electron and muon candidates used in the analysis were reconstructed with the methods previously discussed since PF reconstructed objects were not well-developed for high energy electrons and muons.

The PF particle collections are then used as inputs to higher-level reconstruction algorithms that are used to:

- build hadronic jets
- determine the missing transverse energy
- reconstruct and identify τ-leptons from their decay products

- quantify charged lepton isolation with respect to other particles
- tag b-jets

The development of PF takes advantage of the CMS detector's excellent tracker and calorimeter system resolutions.

Charged particles constitute about two-thirds of jet energy and due to jet fragmentation, their p_{T}'s can vary from a few MeV/c up to hundreds of GeV/c. PF exploits the tracker's momentum resolution and precise measurement of the charged-particle direction. For stable particle constituents with low p_{T}'s, it also takes advantage of the superior tracker resolution over the calorimeters, particularly the EM compartment. The PF algorithm applies an iterative-tracking strategy to achieve high efficiency in charged-particle tracks reconstruction and small misidentification rate for a wide range of p_{T}'s and for $|\eta| < 2.5$. In order to achieve this, it first seeds and reconstructs tracks using stringent criteria. This first iteration selects lightest quality tracks and is designed to minimize the misidentification rate. To accomplish high track-reconstruction efficiency, the following iterations loosen the track seeding criteria to look at the remaining hits to reconstruct tracks that have been missed, in particular it allows for the reconstruction of tracks that have no hits in the inner layers of the tracker. Additionally, they remove hits unambiguously assigned to the tracks found to keep a low fake rate due to reduced combinatorics. After the last iteration, the track finding efficiency is $\sim$99.5% for muons with $p_{\mathrm{T}} > 5$ GeV/c and >90% for charged hadrons from jets with $p_{\mathrm{T}} > 1$ GeV. The fourth and fifth iterations have relaxed requirements on the origin vertex to allow for the reconstruction of secondary charged particles to account for photon conversions, nuclear particles in the tracker material, and decays of long-lived particles, e.g. K^0_S's, Λ's. From this iterative-tracking algorithm, the PFRecTracks collection is created.

The next step in the PF algorithm is to apply a calorimeter clustering algorithm in order to:

- measure the energy and direction of stable neutral particles
- allow for stable neutral particle energy deposits to be separated from those originating from charged hadrons
- reconstruct and identify electrons and all accompanying bremsstrahlung photons
- measure the energy for charged hadrons for which the track parameters were not determined properly (low-quality and high-pT tracks)

and is performed separately for ECAL barrel, ECAL endcap, HCAL barrel, and the HCAL endcap. The algorithm first identifies local calorimeter-cell energy maxima above a given energy as *cluster seeds*. The cluster seeds are then used to formulate topological clusters. Each topological cluster originates at a cluster seed and grows by adding neighboring cells to those already included in the topological cluster. The neighboring cells are defined as cells with at least one side in common and energy thresholds of two standard deviations of the electronics noise in the ECAL (order of 10 keV) and 800 MeV in the HCAL.

Finally, the PF applies a linking algorithm to fully reconstruct each single particle and remove double counting from different subdetectors. Links are established between tracks, calorimeter clusters, and muon tracks in the muon system by extrapolating between tracker/muon hits and calorimeter energy clusters. First, tracks are extrapolated from their last measured hit in the tracker to the calorimeters. They are linked to a given calorimeter cluster, i.e. a cluster in ECAL corresponding to an electron shower profile or a cluster in the HCAL corresponding to a typical

hadron shower, if the position in the corresponding calorimeter is within the cluster boundaries. Similarly, in order to collect bremsstrahlung photons emitted by a electrons, a link is established between the tangent to the tracks and the ECAL. The extrapolated tangent position must fall within the boundaries of the cluster. For the linking between calorimeters, the ECAL cluster, which has higher granularity, must fall within the HCAL. Finally, a global fit between a charged-particle track in the tracker and a muon track in the muon system is used to generate a link between the tracker and the muon systems. The fit is required to return an acceptable χ^2 value. Whenever multiple muons can be linked to several tracker tracks, the combination with the lowest χ^2 is chosen. Through these linking procedures, the algorithm produces *block* of elements linked directly or indirectly. These blocks are then used for the reconstruction and identification of stable particles.

4.3.2 PF Muons and Electrons

To create *PF Muons*, PF uses global muons with the additional restriction that their combined momentum is compatible with that solely determined from the tracker within 3σ. The tracks and muon hits that were part of the PF Muons collection are removed from the blocks before further processing of the event. PF Electrons are reconstructed using the tracks and calorimeter information. As they make their way to the calorimeter, many electrons will leave short tracks in the tracker as they interact with the silicon strip detectors and undergo Bremsstrahlung. Once these short tracks are pre-identified as electron tracks, they are refitted with a Gaussian Sum Filter to help trace the electron's path all the way to the ECAL. The *PF Electron* is a combination of the fitted tracks and ECAL clusters. After the final identification of the PF Electrons, all corresponding tracks and ECAL clusters (including those

accounting for Bremsstrahlung photons) are removed from the blocks.

4.3.3 PF Charged and Neutral Hadrons, and PF Photons

The remaining tracks in the blocks are used to reconstruct *PF Charged Hadrons*. Tracks are removed if the relative uncertainty of the track p_{T} is larger than the relative calorimeter energy resolution for charged hadrons. This quality criteria removes 0.2% of the tracks belonging to hadronic jets, 90% of them being fake tracks. However, the energy of the remaining 10% of the rejected tracks, originating from real particles, will not be lost since they deposit their energy in the calorimeter, where they will be measured with higher precision. The remaining tracks are extrapolated to calorimeter clusters. Whenever a track can be linked to more than one ECAL/HCAL cluster, the link to the closest cluster is kept. ECAL clusters that emerge from overlapping photons, and not hadronic showers, are excluded from the linking procedure to preserve efficient photon detection. In order for a track to be identified as a PF Charged Hadron, its total calibrated calorimetric energy must be within 3σ of the track momentum. The tracks rejected by this last requirement can be either muons or fake tracks. In order to recover the remaining muons, which were missed during the PF muon reconstruction, a relaxed search for muons is performed. At this stage, the PF Charged Hadrons have been identified and a large portion of the fake tracks have been removed, therefore with a relaxed search, muon reconstruction efficiency can be increased without jeopardizing the low muon fake rate. All reconstructed PF Charged Hadrons are considered to be pions.

The remaining calorimeter clusters and tracks in the blocks are considered for the reconstruction of *PF Neutral Hadrons* and *PF Photons*. HCAL clusters not linked to any tracks will create PF Neutral Hadrons. ECAL clusters not linked to tracks or

remaining from removed links will be attributed to PF Photons. In the case where a charged particle is nearby and the calibrated energy of the calorimeter clusters is significantly larger than track p_{T}, then the energy excess will be used to create both a PF Photon and a PF Neutral Hadron. The PF Photon energy will be that of the ECAL energy, where we expect excellent resolution, whereas the PF Neutral Hadron will be assigned the remaining amount of the energy excess. More details on the PF calibration procedures can be found in reference [6].

4.4 Jet Reconstruction

The efficient reconstruction of jets is important for the identification of b-jets and hadronically decaying τ-leptons, which are crucial tools in the search for high mass resonances decaying to τ-leptons. This section will describe the jet reconstruction algorithm used to create the *PF Jets* collection. Then Section 4.5 will explain the use of b-quark properties used to identify jets that arise from bottom quark hadronization (b-jets), which are used in this analysis as a means to reject events with top decays. Hadronically decaying τ-leptons, τ_h, are reconstructed PF Jets at particle-level, thus we apply an identification algorithm to create the *PF Tau* candidates which we use in the final selections . In Section 4.6, we will describe the Hadron-Plus-Strips Algorithm, used to identify τ_h and veto against hadronic jets using particle isolation.

Jets are reconstructed at particle level by clustering four-momentum vectors of PF candidates using the anti-k$_T$ algorithm [64]. Since charged particles and photons compose $\sim$ 90% of jet energy, PF particles provide excellent precision for the jet-energy, while only 10% of the jet energy measurement, belonging to neutral hadrons, is compromised by poor HCAL resolution. The reconstruction of jets using the anti-k$_T$ algorithm provides robust discrimination against the presence of soft particles

radiated by partons and ensures that partons that have split into a pair of collinear partons are recombined to form the original parton. The algorithm finds the highest p_{T} entity and searches for softer particles around it to create a cluster. Through several iterations, it evaluates two effective distances, the distance between two jet entities (particles or pseudojets):

$$d_{ij} = min(\frac{1}{k_{t,i}^2}, \frac{1}{k_{t,j}^2})\frac{\Delta_{ij}^2}{R^2} \tag{4.3}$$

and the distance between the entity i and the beam:

$$d_{iB} = \frac{1}{k_{t,i}^2} \tag{4.4}$$

where $\mathrm{k}_{t,i/j}$ is the transverse momentum, R is the radius parameter set to 0.5, and Δ_{ij} is the distance in $\eta - \phi$ space between entity i and entity j:

$$\Delta_{ij} = \sqrt{(\eta_i - \eta_j)^2 + (\phi_i - \phi_j)^2} \tag{4.5}$$

The anti-k_T initially defines PF objects as *preclusters* and calculates d_{iB} for each of them. Additionally it calculates d_{ij} for each pair of preclusters. For each precluster i, it chooses the jth combination that gives the smallest d_{ij} value. If this combination satisfies: $\mathrm{d}_{iB} < \mathrm{d}_{ij}$, then preclusters i and j are removed from the set of preclusters and a new precluster is included in the set of preclusters. The new precluster is defined as the combination of the i and j preclusters. The algorithm will continue iterations until no preclusters. However, if $\mathrm{d}_{iB} > \mathrm{d}_{ij}$, then a new jet is created.

Jets are subjected to three types of corrections:

- L1 Pileup Correction, removes additional jet energy contributions originating from pile-up events and noise

- L2 Relative Jet Correction, makes jet energy response uniform as a function of η
- L3 Absolute Jet Correction, makes jet energy response flat as a function of p_{T}

For more details on Jet energy corrections, please see [65].

4.5 b-jet Identification

A robust algorithm is needed for the identification of b-jets. CMS analyses use a Particle Flow based algorithm that exploits the hard fragmentation functions of b quarks as well as their semileptonic decays, long lifetime, and relatively large mass. The analysis presented in this thesis uses an identification algorithm based on track impact parameters called Track Counting High Efficiency (TCHE) [66].

The TCHE algorithm takes advantage of the excellent spatial resolution of the silicon track to determine the impact parameter of a track with respect to the primary vertex. The IP and its estimated uncertainty are used to distinguish decay products of a b hadron from prompt tracks. The ratio of the IP and its uncertainty is defined as the IP significance. The high efficiency of the TCHE algorithm is achieved by ranking tracks in a jet in order of decreasing IP significance. Light-flavour jets have low probability of having several tracks with high positive values of IP significance; therefore the TCHE algorithm selects the jet with the second and third track as the discriminator. The discriminators are chosen such that there is a 10%, 1%, and 0.1% mis-tag rate for the loose (L), medium (M), and tight (T) working points, respectively.

4.6 Tau Reconstruction and Identification

Hadronically decaying taus, which will be referred to as τ_h in the remainder of the paper, most often decay into one or three charged hadrons possibly accompanied by a number of π^0's (in addition to the neutrinos). In this subsection, we will describe the properties of τ-leptons and the τ_h reconstruction algorithms used in CMS τ analyses.

4.6.1 Properties of Tau Leptons

> *"We have found 64 events of the form* $e^+ + e^- \rightarrow e^\pm + \mu^\mp + \geq 2$ *undetected particles, for which we have no conventional explanation. ... A possible explanation for these events is the production and decay of a pair of new particles, each having a mass in the range of 1.6 to 2.0 GeV/c."* [67]

The above statements are the first and last sentences of the τ discovery paper [67] published in 1975. The undetected particles are what we refer to as τ leptons, the heaviest of the lepton family. The τ-leptons have indeed shown to be unconventional fundamental particles, with a mass of 3477 $m_e (m_\tau = 1.777 GeV/c^2)$, they are the only ones in the lepton family that decay to hadrons. The τ's will decay hadronically $\sim 65\%$ of the time and leptonically, into the lighter leptons e and μ, $\sim 35\%$ of the time. As shown in Figure 4.5 the $\tau^\pm$ decays via the weak interaction through the emission of a $W^\pm$ and a ν_τ. The W can decay leptonically, $W \rightarrow e + \nu_e$ or $W \rightarrow e + \nu_e$, or hadronically, $W \rightarrow q + q'$. Additionally, 45% of hadronic τ decays are characterized by the production of intermediate resonances, $\rho(770)$ and $a_1(1260)$ (figure 4.6).

The hadronic τ decays into an odd number of charged hadrons, often accompanied by one or more π^0 to conserve electric charge. Hadronically decaying τ's, τ_h, decaying into n-charged hadrons are classified as n-prong taus, i. e. a τ_h decaying into one

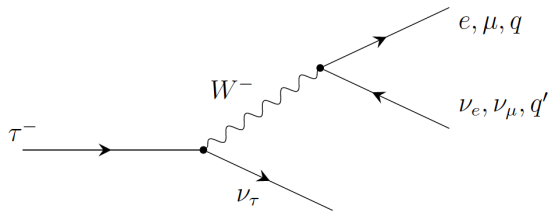

Figure 4.5: τ Decays. Feynman diagram illustrating allowed τ-lepton decays. The τ-lepton decays can either be leptonic ($\tau^- \to e^- \bar{\nu}_e \nu_\tau$ or $\tau^- \to \mu^- \bar{\nu}_\mu \nu_\tau$) or hadronic ($\tau^- \to q\bar{q}\nu_\tau$).

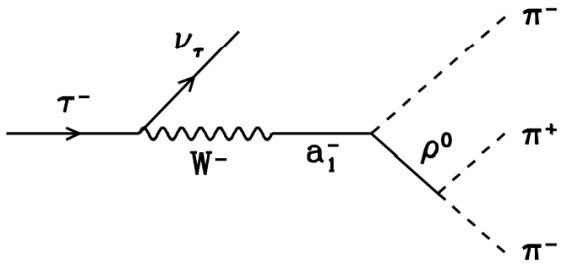

Figure 4.6: τ Hadronic Decay. Feynman diagram illustrating τ-lepton hadronic decay via $\tau^- \to a_1(1260) + \nu_\tau$.

charged hadron is referred to as a 1-prong τ_h. Close to 100% of all τ_h's are 1 or 3 prong τ's. Table 4.2 shows the predominant τ decays along with their perspective branching ratios, where the h denotes a $\pi^{\pm} or K^{\pm}$ hadron.

Due to their short lifetime of 2.9×10^{-3} s or ct $\sim 87\mu$m, τ-leptons decay almost instantaneously and must be identified by their decay products. This poses some challenges in the identification of τ-leptons at hadron colliders. In the case of leptonic decays, there is no way to determine if an electron or a μ candidate are produced directly or are products of a τ decay. For hadronic decays, the signature of a τ_h is very similar to that of a quark/gluon QCD jet. The QCD jets are produced at a rate of several orders of magnitude higher than new physics signatures at hadron

Table 4.2: Decays for τ-leptons. Shown are the dominant leptonic and hadronic τ-lepton decay modes with their perspective branching ratios.

Decay Mode	Resonance	BR[%]
$e^-\bar{\nu}_e\nu_\tau$		17.9
$\mu^-\bar{\nu}_\mu\nu_\tau$		17.4
Total Leptonic		35.3
$h^-\nu_\tau$		11.5
$h^-\pi^0\nu_\tau$	$\rho(770)$	26.0
$h^-\pi^0\pi^0\nu_\tau$	$a_1(1260)$	9.5
$h^-h^-h^+\nu_\tau$	$a_1(1260$	9.8
$h^-h^-h^+\pi^0\nu_\tau$		4.8
Total hadronic		61.6
other hadronic		3.1

colliders. However, since τ's produced in decays of heavy particles, as such is the case in our search, are heavily boosted, their decay products will be boosted along the original direction of the τ. The collimated object composed of charged hadrons, neutrinos, and neutral hadrons resulting from the hadronic decay of the τ-lepton is a unique signature that helps us differentiate between QCD-jets and τ_h-jets. This characteristic has been exploited at experiments such as CDF [49] at the Tevatron and CMS [6] at the LHC to design a robust and efficient τ ID algorithm (explained in detail in the next subsection).

4.6.2 The HPS Reconstruction Algorithm for Hadronic Decays of Tau Leptons

CMS uses the Hadron-Plus-Strips (HPS) τ_h identification algorithm based on PF reconstruction. HPS [6] searches for PFJets that satisfy the τ_h decay modes defined in Table 4.2. Isolation is applied using ECAL and tracker information, in a similar way as done for the electron. Finally, the HPS algorithm also provides tunable parameters to discriminate against electrons and muons from being misidentified as

genuine τ_h candidates.

4.6.2.1 Decay Mode Finding

HPS combines 0-2 π^0 candidates with 1 or 3 charged hadrons to identify τ_h candidates by reconstructing the hadronic decay modes for 1 or 3 prong taus. The charged hadrons and, if available, π^0 candidates must be present in a narrow signal cone with $\Delta R = (2.8\,\mathrm{GeV}/c)/p_T^{\tau_h}$ centered around the leading track since the decay products of the τ_h are boosted in the direction of the original τ-lepton. Genuine π^0's will decay into 2γ's that can undergo conversions in the tracker material. Therefore, they deposit their energies into rectangular strips that spread along the ϕ direction in the ECAL and have a narrow spread in η, $\Delta\eta = 0.05$, due to the bent of the electrons/positrons by the high magnetic field. The algorithm searches for associated electromagnetic PF particles within a $\Delta\phi = 0.20$ in the strip to create the π^0 candidate. A τ_h candidate is then composed of strips and 1-or-3 PF charged hadrons, as shown in Figure 4.7. If the τ_h candidates successfully reconstruct the hadronic decay modes show on Table 4.2, then they pass the "Decay Mode Finding" requirement. The performance of the "Decay Mode Finding" is shown in Figure 4.8 for τ_h with $p_\mathrm{T} > 20$ GeV and $|\eta| < 2.3$.

4.6.2.2 Tau Isolation

HPS τ_h isolation defined an isolation cone of ΔR_{iso} size around the leading charged hadron. There must be no neutral or charged candidates found inside the isolation cone with transverse momentum higher than $p_\mathrm{T}^{h^\pm}$, for charged hadrons, and p_T^{γ}, for neutrals. Different isolation working points are defined by ΔR_{iso}, $p_\mathrm{T}^{h^\pm}$, and p_T^{γ} requirements defined in Table 4.3.

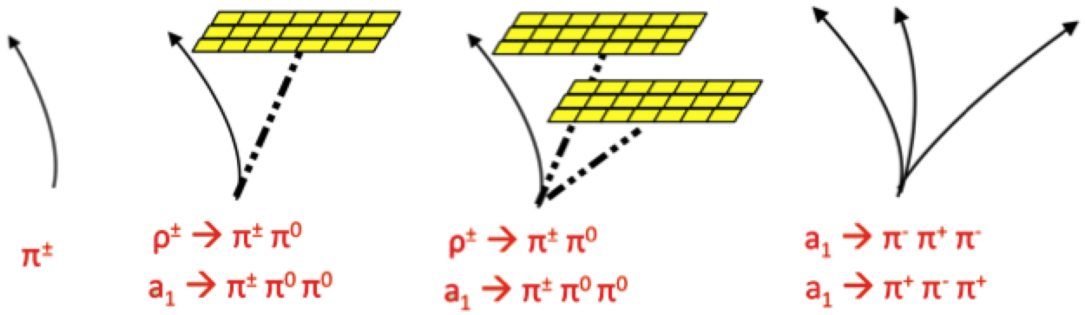

Figure 4.7: Decay Mode Finding. The CMS Hadron-Plus-Strips algorithm is used to identify hadronically decaying τ-leptons by using their visible decay products to reconstruct various decay modes. The illustration shows the reconstruction of one and three prong τ_h decays using the Hadron-Plus-Strips Decay Mode Finding algorithm. It selects charged hadrons (1 or 3) and combines them with π^0's, which deposit their energy into ECAL strips with a spread along the ϕ direction.

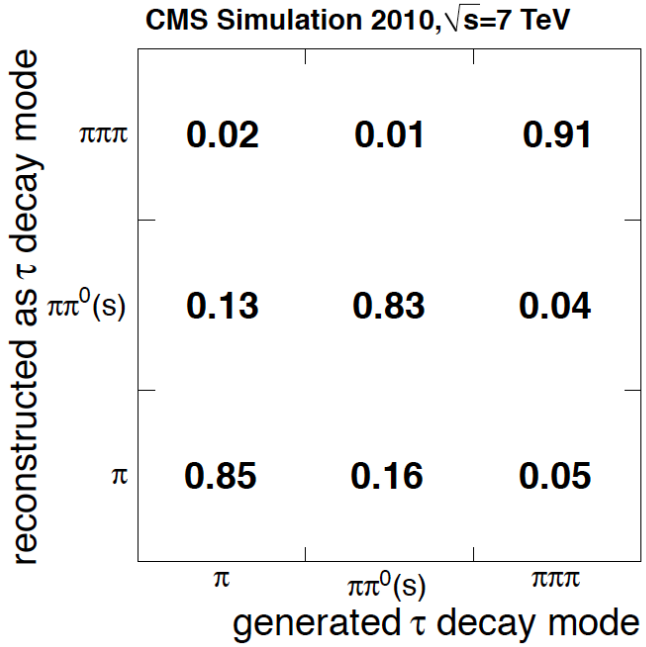

Figure 4.8: τ_h Reconstruction Efficiency. An illustration of the τ_h reconstruction efficiency for dominant hadronic decay modes using the HPS Decay Mode Finding algortihm with simulation data [6].

Table 4.3: Parameters Used to Define the Working Points for HPS τ_h Isolation. Each HPS discriminant is defined to have an isolation cone of ΔR_{iso} size and require no PF charged hadron candidates with $p_{\mathrm{T}} > p_{\mathrm{T}}^{h^{\pm}}$, and no PF gamma candidates with $E_{\mathrm{T}} > p_{\mathrm{T}}^{\gamma}$ in the isolation cone

Working Point	ΔR_{iso}	$p_{\mathrm{T}}^{h^{\pm}}$	p_{T}^{γ}
ByVLooseIsolation	0.3	1.5 GeV/c	2.0 GeV
ByLooseIsolation	0.5	1.0 GeV/c	1.5 GeV
ByMediumIsolation	0.5	0.8 GeV/c	0.8 GeV
ByTightIsolation	0.5	0.5 GeV/c	0.5 GeV

The $\Delta\beta$ correction is applied to minimize the effect due to the increased number of particles in the isolation region due to pile-up. This correction is applied by identifying particles in the isolation region coming from other primary vertices and summing their p_T. and Table 4.4. Isolation discriminants that include $\Delta\beta$ corrections are defined by ΔR_{iso}, $p_{\mathrm{T}}^{h^{\pm}}/E_{T,min}^{\gamma}$, $(\Sigma p_{\mathrm{T}}^{iso}/E_{\mathrm{T}}^{iso})^{\Delta\beta}$, where $(\Sigma p_{\mathrm{T}}^{iso}/E_{\mathrm{T}}^{iso})^{\Delta\beta}$ are the sum of the ratio between the transverse momentum and energy including the subtraction of the isolation candidates emerging from PU.

The performance of some of the most commonly used HPS isolation working points are shown in Figure 4.8.

4.6.2.3 Muon and Electron Rejection

HPS anti- electron and muon vetoes have been developed to reject events where electrons and muons are misidentified as τ_h candidates. One of the largest irreducible backgrounds for this search, and for Higgs searches, is a Z boson decaying into two electrons. The reason for this is because electrons can easily be reconstructed as one-prong τ_h candidates. The detector signature for an electron is an energy spread

Table 4.4: Parameters Used to Define the Working Points for HPS τ_h Isolation. Each HPS discriminant is defined to have an isolation cone of ΔR_{iso} size and thresholds are applied on the $p_{\mathrm{T}}^{h^{\pm}}/E_{T,min}^{\gamma}$ and the sum of the ratio between the transverse momentum and energy with $\Delta\beta$ corrections, $(\Sigma p_{\mathrm{T}}^{iso}/E_{\mathrm{T}}^{iso})^{\Delta\beta}$, for charged hadron and gamma candidates in the isolation cone

Working Point	ΔR_{iso}	$p_{\mathrm{T}}^{h^{\pm}}/E_{T,min}^{\gamma}$	$(\Sigma p_{\mathrm{T}}^{iso}/E_{\mathrm{T}}^{iso})^{\Delta\beta}$
ByVLooseIsolationDBSumPtCorr	0.3	0.5 GeV/c	3.0 GeV
ByLooseIsolationDBSumPtCorr	0.5	0.5 GeV/c	2.0 GeV
ByMediumIsolationDBSumPtCorr	0.5	0.5 GeV/c	1.0 GeV
ByTightIsolationDBSumPtCorr	0.5	0.5 GeV/c	0.8 GeV

in ϕ or in an ECAL strip in addition to a charge track. Therefore, the electron veto plays a very important role in all τ_h analyses. In addition, the removal of the barrel-endcap crack region, where track reconstruction is not available, and checks for Bremsstrahlung (BS) patterns are used as part of the discriminators. An MVA algorithm is used for the development of loose, medium, and tight electron vetoes, shown in Table 4.5.

Table 4.5: HPS Anti-Electron Vetoes. The HPS anti-electron vetoes used to reject electrons misidentifed as τ_h candidates. Each discriminant is developed by an MVA algorithm and may have checks for Bremsstrahlung (BS) patterns or remove the crack region ($1.4442 < |\eta| < 1.566$).

Discriminant	MVA_{max}	Other
AgainstElectronLoose	0.6	N/A
AgainstElectronMedium	-0.1	$!(1.4442 < \|\eta\| < 1.566)$
AgainstElectronTight	-0.1	$!(1.4442 < \|\eta\| < 1.566)$, BS pattern checks

Events where muons are misidentified as τ_h candidates arise whenever there is

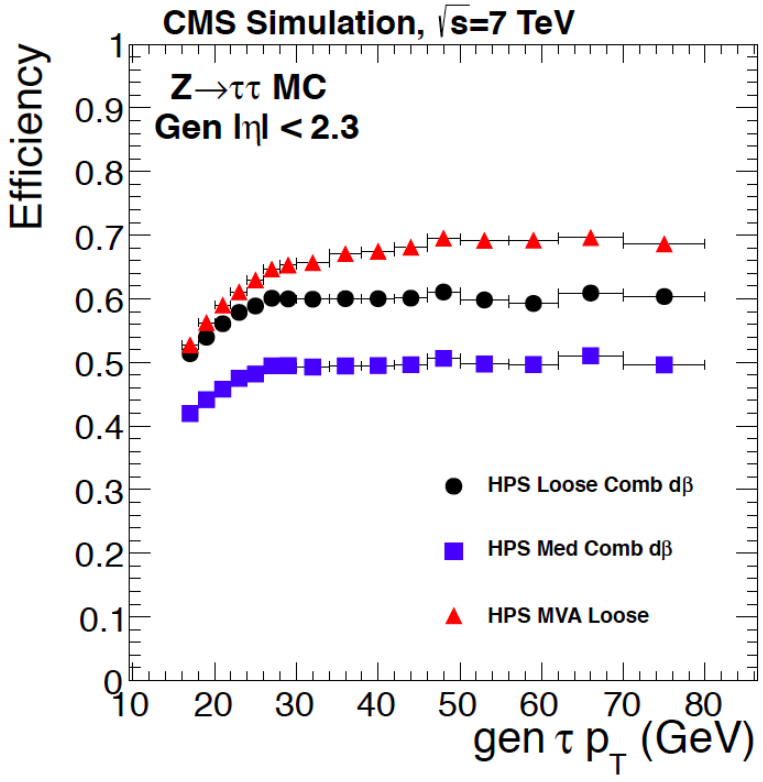

Figure 4.9: Performance of HPS τ_h Isolation. The τ_h isolation efficiency for commonly used HPS isolation discriminators was calculated using $Z \to \tau^+\tau^-$ simulation data [6]. An illustration of the performance for the loose and medium (with $\Delta\beta$ corrections) working points is shown for τ_h candidates with different p_{T}'s within the $|\eta| < 2.5$ region.

substantial energy in the calorimeter. To veto against events where a μ fakes a τ_h candidate, the against-muon discriminants were developed by a ΔR match between the τ_h leading track and the μ-track and μ chamber hits and energy deposits in the ECAL + HCAL (since μ's do not loose energy as they pass through calorimeter material). The HPS discriminants are shown in Table 4.6.

Table 4.6: HPS Anti-Muon Vetoes. The HPS anti-muon vetoes used to reject muons misidentifed as τ_h candidates. Each discriminant is developed by using tracks and muon hits to discriminate againts muons, as well as ECAL + HCAL energy deposits.

Discriminant	Requirements
AgainstMuonLoose	τ_h leading track not matched to μ chamber hits
AgainstMuonMedium	τ_h leading track not matched to Global/tracker μ
AgainstMuonTight	τ_h leading track not matched to Global/tracker μ, large energy deposits found in ECAL + HCAL

4.7 MET Reconstruction

Neutrinos (or generally speaking, any weakly interacting neutral particles) travel through the CMS detector without creating a direct response from the subdetectors. Their presence results in an imbalance of total momentum in the event reconstruction. Determining the four-momentum vectors due to unseen particles is crucial for searches of new physics. Since τ-leptons decay to neutrinos in conjunction with visible particles (e. g. electrons, muons, and hadrons), the precise measurement of momentum imbalance is crucial for the selection of final states involving τ-leptons. In a search for heavy resonances decaying into high-p_{T} τ-lepton pairs, high $\not\!\!E_{\mathrm{T}}$ is expected since neutrinos will take a large percentage of the energy. Requiring large $\not\!\!E_{\mathrm{T}}$ can help discriminate against irreducible backgrounds, such as $\mathrm{Z}/\gamma^* \rightarrow \tau^+\tau^-$, which have, in this case, have the exact same signature but low $\not\!\!E_{\mathrm{T}}$.

The four-momentum vectors due to weakly interacting particles cannot be reconstructed from conservation of the total momentum at hadron colliders. Thus, it is the partons of the protons that interact with each other. Unlike in lepton colliders, where fundamental particles are collided and their initial energies are well known, it is impossible to determine the initial four-momentum vector of the partons mak-

ing up the proton. However, since the colliding beams are carefully steered along the z-axis, there is little to no momentum components in the direction orthogonal to the beamline, the transverse plane. By taking advantage of the conservation of momentum in the transverse plane, we can deduce:

$$\overrightarrow{p_{\mathrm{T}}}^{initial} = 0 = \overrightarrow{p_{\mathrm{T}}}^{final} = \sum_i \overrightarrow{p_{\mathrm{T}}}_i^{visible} + \sum_j \overrightarrow{p_{\mathrm{T}}}_j^{invisible} \tag{4.6}$$

The *Missing Transverse Energy*, symbolizing the momentum imbalance, becomes

$$\overrightarrow{\not{E}_{\mathrm{T}}} = \sum_j \overrightarrow{p_{\mathrm{T}}}_j^{invisible} = -\sum_i \overrightarrow{p_{\mathrm{T}}}_i^{visible} \tag{4.7}$$

$\not{E}_{\mathrm{T}}$ can either be calculated using calorimeter towers, CaloMET, or using PF candidates. Since PF reconstruction is less susceptible to pileup or random calorimeter spikes and mismeasurements, superior energy resolution and excellent measurement of the direction of all the visible objects in an event is achieved. In this analysis, PF based $\not{E}_{\mathrm{T}}$ will be used. Thus, the index i in Equation 4.7 will run over all PF candidates in an event to calculate the *raw* $\overrightarrow{\not{E}_{\mathrm{T}}}$. Corrections are applied to the raw $\not{E}_{\mathrm{T}}$ in order to acquire the best estimate of the *true* value of $\not{E}_{\mathrm{T}}$ carried by the invisible particles. Type-I correction is applied to propagate the jet energy corrections (JEC) to the $\not{E}_{\mathrm{T}}$. Type-0 corrections are applied to account for the effects of pile-up. Additionally, $\not{E}_{\mathrm{T}}$ filters are used to correct for detector effects such as cracks, dead material, tracking failure, electronics noise, and dead ECAL cells. For more details on $\not{E}_{\mathrm{T}}$ reconstruction, corrections, and filters refer to [68].

5. SEARCH FOR NEUTRAL HEAVY RESONANCES DECAYING TO DI-TAU PAIRS ANALYSIS

This chapter describes the search for heavy neutral resonances decaying to pairs of τ-leptons using 4.94 fb^{-1} of proton-proton collision data collected by the CMS detector. The ditau final states under study are defined by the hadronic and leptonic decays of τ-leptons. The biggest challenge for analyses with ditau final states is suppressing the QCD-multijet production since 88% of ditau decays include at least one τ_h. QCD-multijet events in ditau analyses emerge from the high probability of a jet to be misidentified as a hadronically decaying τ-lepton (τ_h) candidate. The individual sensitivity of the ditau final states included in this analysis has been determined by the branching ratio, signal acceptance, and expected background event rates. The four most relevant ditau final states (i.e. $\tau_{\rm h}\tau_{\rm h}$, $\mu\tau_{\rm h}$, $e\tau_{\rm h}$, and $e\mu$) are statistically combined to maximize the sensitivity of the analysis. The $lepton + \tau_h$ channels ($e\tau_{\rm h}$ and $\mu\tau_{\rm h}$) drive the power of the overall search. About 46% of $\tau^+\tau^-$ decays have $lepton + \tau_h$ final states, therefore together the $e\tau_{\rm h}$ and $\mu\tau_{\rm h}$ channels have a higher branching ratio than the $\tau_{\rm h}\tau_{\rm h}$ (BR($\tau^+\tau^- \to \tau_{\rm h}\tau_{\rm h}$) $\sim 42\%$). In the $lepton + \tau_h$ channels, the requirement of a prompt lepton, e or μ, present in the event (as opposed to the τ_h) removes a substantial amount of backgrounds from QCD-multijet production. On the other hand, the $\tau_{\rm h}\tau_{\rm h}$ final state, which gains in sensitivity from its high branching ratio, suffers from the highest QCD-multijet contamination. The $e\mu$ channel has the least contamination from backgrounds due to the requirement of two prompt leptons but also has a much smaller branching ratio than the other channels (BR($\tau^+\tau^- \to \tau_{\rm h}\tau_{\rm h}$) $\sim 6\%$). This chapter focuses on the $e\tau_{\rm h}$ final state, where one τ decays leptonically into an electron, and the other into hadronically (τ_h). The $e\tau_{\rm h}$

channel, of which this author was the primary analyst, has been combined with the other ditau final states under investigation to search for an excess of observed events over the SM hypothesis. While this search has been designed as model independent, the Sequential Standard Model (SSM) Z′ production is used as a benchmark model to set a limit on the Z′ mass in the absence of a discovery. The SSM Z′ allows for easy comparison of the results with those in other final states and with measurements performed at different experiments. The current best limit comes from the Collider Detector at Fermilab (CDF-II) that set the lower mass bound of 399 GeV/c^2 for such resonance using the Sequential SM Z′ boson [49]. Therefore, the analysis targets hypothetical production of Z′ resonances with masses higher than 350 GeV/c^2.

5.1 Analysis Strategy

In the occurrence of Z′ production in a pp collision, such event can be reconstructed by identifying the new resonance's decay products. However, in searches involving τ-leptons, the τ's decay almost instantaneously due to their short lifetime (2.9×10^{-13} s). Therefore, unlike searches for Z′ production with ee and $\mu\mu$ final states where the electrons and muons live long enough to be directly detected by the CMS detector, the final states for $\tau^+\tau^-$ analyses are defined by τ decay products. There are six very distinct channels defined by the leptonic and hadronic decays of τ-leptons and characterized by different leads of background. As mentioned in Section 4.6.1, τ-leptons decay leptonically $\sim 35\%$ of the time ($\tau \to e\nu_e\nu_\tau, \tau \to \mu\nu_\mu\nu_\tau$) or hadronically $\sim 65\%$ of the time (n$\pi^\pm$ m$\pi^\mp$ k$\pi^0\nu_\tau$, where n+m = 2i+1 and i, k are integers). The six possible final states of ditau decays are:

- $\tau_{\rm h}\tau_{\rm h}$ channel: $Z' \to \tau^+\tau^- \to \tau_h^+\tau_h^-\nu_\tau\bar{\nu_\tau}$
- $\mu\tau_{\rm h}$ channel: $Z' \to \tau^+\tau^- \to \mu^+\tau_h^-\bar{\nu_\mu}\nu_\tau$ (or $\mu^-\tau_h^+\nu_\mu\bar{\nu_\tau}$)

Table 5.1: Di-Tau Final States. The final states of a hypothetical resonance decaying into a $\tau^+\tau^-$ final state are defined by the leptonic and hadronic decay products. The six allowed final states for a hypothetical resonance decaying into a pair of tau leptons and their perspective branching fractions is shown in the table.

Final State	Branching Fraction
$\tau\tau \to \tau_{\rm h}\tau_{\rm h}$	42%
$\tau\tau \to \mu\tau_{\rm h}$	22.5%
$\tau\tau \to e\tau_{\rm h}$	23.1%
$\tau\tau \to e\mu$	6.2%
$\tau\tau \to ee$	3.1%
$\tau\tau \to \mu\mu$	3.1%

- $e\tau_{\rm h}$ channel: $\mathrm{Z}' \to \tau^+\tau^- \to e^+\tau_h^-\bar{\nu}_e\nu_\tau$ (or $e^-\tau_h^+\nu_e\bar{\nu}_\tau$)
- $e\mu$ channel: $\mathrm{Z}' \to \tau^+\tau^- \to e^+\mu^-\bar{\nu}_e\nu_\mu\nu_\tau\bar{\nu}_\tau$ (or $e^-\mu^+\nu_e\bar{\nu}_\mu\nu_\tau\bar{\nu}_\tau$)
- ee channel: $\mathrm{Z}' \to \tau^+\tau^- \to e^+e^-\bar{\nu}_e\nu_e\nu_\tau\bar{\nu}_\tau$
- $\mu\mu$ channel: $\mathrm{Z}' \to \tau^+\tau^- \to \mu^+\mu^-\bar{\nu}_\mu\nu_\mu\nu_\tau\bar{\nu}_\tau$

where τ_h denotes the visible decay products of a hadronically decaying τ-lepton. The respective branching ratios of these decays are shown in Table 5.1.

The analysis combines the four most sensitive ditau final states: $\tau_{\rm h}\tau_{\rm h}$, $\mu\tau_{\rm h}$, $e\tau_{\rm h}$, and $e\mu$. The contribution of ee and $\mu\mu$ ditau final states to the statistical significance of the measurement is negligible due to their small branching ratios and very large Drell-Yan background contamination; therefore, they are not included in this search. The $e\mu$ final state, whose significantly lower branching ratio is compensated by its exceptionally clean signature (low background contamination) is the only fully leptonic ditau final state included in this search. Of the four final states under study, the $\tau_{\rm h}\tau_{\rm h}$ channel has the highest branching ratio ($\sim 42\%$); however the signal sensitivity is significantly affected by the large QCD-multijet contamination due to the

high probability of quark or gluon jets to be misidentified as a τ_h. On the other hand, the lower probability of a jet to be misidentified as a lepton (e, μ) results in a significantly smaller QCD-multijet contamination in the lepton+τ_h channels. Thus, the $e\tau_{\rm h}$ and $\mu\tau_{\rm h}$ final states provide most sensitivity for the combined search. The $\mu\tau_{\rm h}$ final state is the cleanest of the lepton+τ_h channels. The requirement of an isolated muon candidate heavily suppresses the QCD-multijet background. Even though the $e\tau_{\rm h}$ and $\mu\tau_{\rm h}$ have similar topologies and common backgrounds, the background contamination in the $e\tau_{\rm h}$ channel is larger. The difficulty in the $e\tau_{\rm h}$ final state emerges from the larger probability of a jet to be misidentified as an electron candidate, compared to that for a muon candidate. To improve the significance in the $e\tau_{\rm h}$ channel, a tighter isolation criteria is applied on the electron candidate, in comparison to the isolation applied to the muon candidate in the $\mu\tau_{\rm h}$ channel, to suppress QCD-multijet background. Additionally, a strong anti-electron veto is applied on the τ_h candidate to suppress background due to $\rm Z/\gamma^* \rightarrow e^+e^-$ production (note that the electron signature in the detector is almost identical to that of a 1-prong τ_h candidate). This allows the $e\tau_{\rm h}$ channel to maintain comparable signal significance with the $\mu\tau_{\rm h}$ and $\tau_{\rm h}\tau_{\rm h}$ channels. After appropriate optimization, the $e\tau_{\rm h}$ final state contributes significantly to the overall sensitivity of this search. This thesis focuses on the signal selections, optimization, and background estimation methods of the $e\tau_{\rm h}$ channel.

The main challenges in this analysis are to successfully reconstruct and identify τ decay products, reduce contamination due to standard model backgrounds, and construct an effective ditau mass estimator to maximize discrimination against low energy backgrounds. Efficient and robust identification of electron and τ_h objects helps reduce backgrounds from non-heavy flavor QCD-multijet production. Isolation requirements are imposed the candidates identified as the electron and τ_h objects to

select particles from prompt decays and removes events with jets, including those with heavy flavor jets decaying into leptons. To further suppress SM backgrounds, a set of topological discriminators has been developed as part of the event selections. These topological requirements play a crucial role in the analysis since the expected backgrounds are produced at much higher rates than the theoretical Z′ resonance. The topological requirements include (1) the removal of events with $b-jets$ to suppress events where $b-jets$ produce electrons associated to jets (QCD-multijet and $t\bar{t}$), (2) the selection of events where the decay products of the two τ-leptons from the Z′ decay are back-to-back in the ϕ direction to remove events with a W boson decaying into well-isolated electrons and a jet misidentified as a τ_h ($W+jets$ and $t\bar{t}$), (3) a missing energy threshold to remove SM backgrounds with little or no $\not{E}_{\mathrm{T}}$ ($\mathrm{Z}/\gamma^* \rightarrow e^+e^-$ and QCD), and (4) the selection of electron and τ_h candidates with opposite electric charge to select pairs coming from neutral resonance decays. Additionally, the event selections are carefully chosen to remain effective for the low energy region, which is used for calibration. The reconstruction of $\mathrm{Z}/\gamma^* \rightarrow \tau^+\tau^-$ events in the low mass region is used for validation of the analysis selections. It also ensures the robustness of the analysis and τ_h identification algorithm. Additional sensitivity for this analysis is gained by the inclusion of the $\not{E}_{\mathrm{T}}$ in the invariant mass calculation provides the advantage of using the signal shape as tool to separate signal from low energy SM backgrounds, explained in more detail in Section 5.2.

The analysis is performed in a quasi-blind fashion to avoid unintended human bias in event selections. Several control regions have been created to study and estimate the expected SM backgrounds. Section 5.7 will describe the data-driven background estimation methods employed in this search as well as the methods for the validation of signal selections in the $e\tau_{\mathrm{h}}$ final state. Data in the signal region is looked at only after all validations and background studies have been completed. Final fit of the

data to the background or signal+background hypothesis is traditionally performed using a suitably defined Z′ mass estimator discussed in the next section. The statistical method is applied for each of the four ditau final states and for their combination taking into account systematic uncertainties and correlations. In the absence of a statistically significant excess over the background-only hypothesis, the results are interpreted in terms of 95% CL upper limits on the ditau invariant mass.

5.2 Di-Tau Invariant Mass Reconstruction

Unlike the case of $Z' \to \mu^+\mu^-$ or $Z' \to e^+e^-$, the mass of a heavy resonance decaying to two τ-leptons cannot be fully reconstructed as the invariant mass of the visible decay products. A large amount of energy is lost due to the neutrinos, which escape detection. To achieve an invariant mass distribution whose mean value resembles the true mass of the resonance, $\not\!\!E_{\mathrm{T}}$ can be included into the mass reconstruction. However, $\not\!\!E_{\mathrm{T}}$ represents a single vector of the overall missing transverse momentum per event. In events with multiple neutrinos present, as is the case in $\tau^+\tau^-$ events, the invisible momenta of the individual neutrinos partially cancels each other. Adding $\not\!\!E_{\mathrm{T}}$ into the ditau invariant mass reconstruction does not provide an accurate reconstruction of the Z′ mass. Despite this, the invariant mass calculation using $\not\!\!E_{\mathrm{T}}$ gives a closer value to the true resonance mass and is well correlated to the true mass value. Most importantly, the simple addition of $\not\!\!E_{\mathrm{T}}$ into the calculation of the invariant mass allows for effective separation of possible signal from background. Using $\not\!\!E_{\mathrm{T}}$, the new resonance will manifest itself as a broad enhancement in the high mass region ($M > 250$ GeV/c^2). Background contributions in the high mass region come only from the tails of the SM background shapes. Therefore, a broad resonance in the high mass region would symbolize a sign of physics beyond the SM. The collinear

approximation technique [69, 70], which is often applied in collider experiments to reconstruct the invariant mass, is not applicable in this analysis. First, the τ-leptons from a heavy resonance are heavily back-to-back due to kinematics. In addition, the ϕ dependent vetoes that are critical for the reduction of $W + jets$ backgrounds preferentially select back-to-back pairs. In this scenario, collinear approximation will fail to adequately reconstruction the ditau invariant mass spectrum. Instead we use:

$$M(\tau_1, \tau_2, \not{E}_{\mathrm{T}}) = \sqrt{(E_{\tau_1} + E_{\tau_2} + \not{E}_{\mathrm{T}})^2 - (\overrightarrow{p_{\tau_1}} + \overrightarrow{p_{\tau_2}} + \overrightarrow{\not{E}_{\mathrm{T}}})^2} \tag{5.1}$$

With the inclusion of $\not{E}_{\mathrm{T}}$ into the invariant mass calculation, the invariant mass shape naturally helps separate signal from SM backgrounds. While SM backgrounds are typically steeply falling functions in the tails, a new high mass resonance decaying to opposite-sign di-taus will exhibit itself as a broad distribution in the high mass region. Figure 5.1 shows the invariant mass shapes (normalized to 1) for one of the main irreducible backgrounds that has no true $\not{E}_{\mathrm{T}}$, $\mathrm{Z}/\gamma^* \to e^+e^-$, a narrow shape peaking near the Z mass (91.2 GeV/c^2) with a tail extending into the high mass region; however, the signal shape for a Z$'$ resonance with a 750 GeV/c^2, where $\mathrm{Z}'(m = 750) \to \tau\tau$, is reconstructed as a wide resonance in the high mass region peaking $\sim 460 GeV/c^2$. The accuracy of mass reconstruction can be calibrated by reconstructing the $\mathrm{Z}/\gamma^* \to \tau^+\tau^-$ events.

5.3 Review of Major Backgrounds

The Z'_{SSM} bosons are produced via $q\bar{q}$ interactions in proton-proton collisions, as shown in Figure 5.2. In the CMS detector the $e\tau_{\mathrm{h}}$ channel decays ($\mathrm{Z}' \to \tau\tau \to e\tau_h + 3\nu$) are characterized by an electron and a τ_h candidate which have opposite electric charge and back-to-back directions of the visible τ momenta. Additionally,

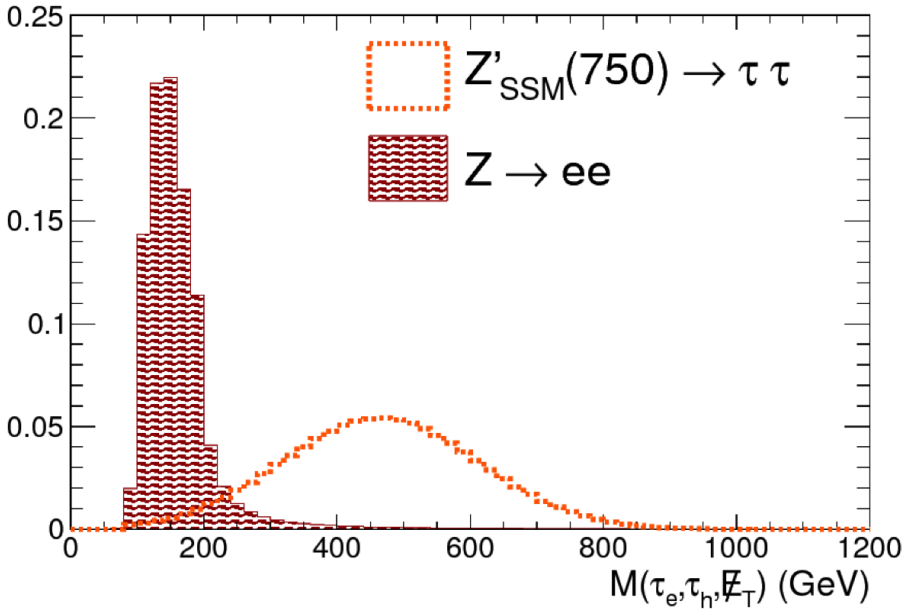

Figure 5.1: The Distribution of the Reconstructed Invariant Mass, M(τ_1,τ_2,$\not{E}_{\rm T}$). The τ_1 candidate is a reconstructed electron, τ_e, and the τ_2 candidate is a reconstructed τ_h. The contribution due to the irreducible Z/γ^* $\rightarrow$ e^+e^- background process is reconstructed as a narrow resonance peaking at m$_Z$($91.2GeV/c^2$). Good resolution and mean value of the reconstructed mass distribution is achieved since there are no neutrinos in the Z/γ^* $\rightarrow$ e^+e^- decay and thus little to no measured $\not{E}_{\rm T}$. On the other hand, the Z$'$ signal distribution where the τ_1 candidate decays leptonically to e + $\nu_e + \nu_\tau$ and τ_2 candidate decays hadronically to $\tau_h + \nu_\tau$, has large $\not{E}_{\rm T}$ due to the 3 neutrinos in this decay. The reconstructed distribution for a Z$'$ resonance with a 750 GeV/c^2 is a wide resonance overlapping with the tail of the Z $\rightarrow$ ee distribution and peaking at $\sim 460GeV/c^2$.

the final states contain significant $\not\!\!E_{\mathrm{T}}$ after being reconstructed due to the momenta taken by the neutrinos in the τ decays. Many SM processes have similar signatures and can be misidentified as Z′ candidates. In the $e\tau_{\mathrm{h}}$ channel, the SM backgrounds include:

- Drell-Yan (Z/γ^*) processes:$\mathrm{Z}/\gamma^* \to \tau^+\tau^-$, $\mathrm{Z}/\gamma^* \to e^+e^-$
- $t\bar{t}$ production
- $W + jets$
- QCD-multijet

Due to the abundance of these SM backgrounds in p-p collisions, it is important to understand how they may mimic the CMS detector response of a genuine Z′ decaying into an e-τ_h pair in order to develop effective event selections discriminating signal from background. It is also crucial to accurately evaluate the rates of the remaining background events after all signal event selections have been made.

5.3.1 $\mathrm{Z}/\gamma^* \to l^+l^-$ Production

The Z/γ^* backgrounds share closely related signatures and topologies with the Z′ signal. The estimation of the invariant mass described in the previous section allows for an effective separation of possible signal from these irreducible backgrounds. By this construction, the $\mathrm{Z}/\gamma^* \to \tau^+\tau^-$ and $\mathrm{Z}/\gamma^* \to e^+e^-$ invariant mass distributions peak near or below the $m_Z = 91.2$ GeV/c^2, which is much lower than the considered Z′ mass range (> 350 GeV/c^2), and have a long tails from γ^* that extends into the signal region. Additionally, the large mass difference between $m_{\mathrm{Z}'}$ and m_Z will result in higher p_{T}'s, on average, for the visible objects in the final state as well as higher

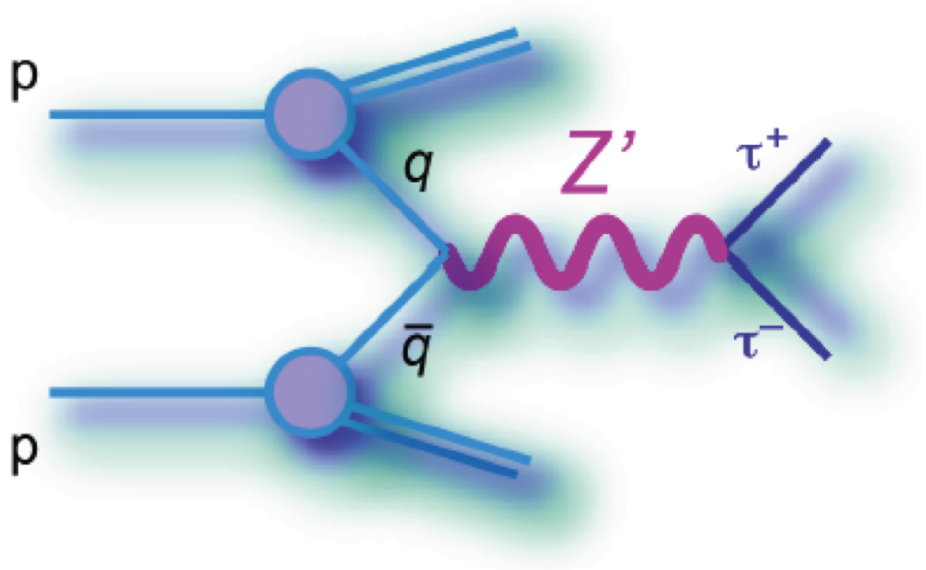

Figure 5.2: Z′ Production at the LHC. Illustration of the leading order feynman diagram for the direct Z′ production followed by the decay into $\tau^+\tau^-$ final state.

$\not{E}_{\mathrm{T}}$. Although requiring higher p_{T} thresholds can greatly reduce the contributions from these backgrounds, a low threshold requirement is maintained to validate the robustness of the signal selections with $\mathrm{Z}/\gamma^* \to \tau^+\tau^-$ events. Preserving the low mass region to calibrate the analysis is possible without any reduction in signal sensitivity because the invariant mass shape helps to clearly distinguish signal from events from $Z \to \tau^+\tau^-$ production.

$Z \to \tau^+\tau^-$ events are used for the calibration of this analysis because their signature, back-to-back τ candidates decaying into an $e\tau_{\mathrm{h}}$ pair with $\not{E}_{\mathrm{T}}$, is identical to that of a Z′ decaying into a pair of τ-leptons. In addition to the validation of signal selections, the efficient reconstruction of the $\mathrm{Z}/\gamma^* \to \tau^+\tau^-$ events will also validate tau identification algorithm used in this analysis. In the $e\tau_{\mathrm{h}}$ channel, events from $\mathrm{Z}/\gamma^* \to \tau^+\tau^-$ production (shown in Figure 5.3) is expected to have the largest back-

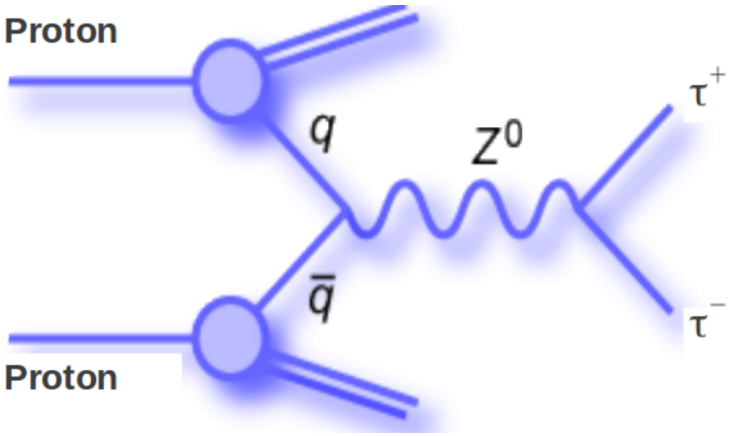

Figure 5.3: $Z/\gamma^* \to \tau^+\tau^-$ Process. Feynman diagram illustrative of the processes that contribute to the leading order production of the neutral weak Z boson decaying to a pair of oppositely charged tau leptons. The $Z/\gamma^* \to \tau^+\tau^-$ background process highly resembles the signature from the Z′ signal.

ground contribution to the signal region. The next largest background contribution in the $e\tau_{\mathrm{h}}$ channel is expected from $Z/\gamma^* \to e^+e^-$, in which the two electrons produced directly from Z decay. A $Z/\gamma^* \to e^+e^-$ event (Figure 5.4) can be misidentified as a signal event whenever one of the electrons has been severely misreconstructed, typically because it is undergoing a strong bremsstrahlung or late showering, fakes a τ_h. Unlike events coming from Z′ decays into $\tau^+\tau^-$, there are no neutrinos in the $Z/\gamma^* \to e^+e^-$ decay. Since $Z/\gamma^* \to e^+e^-$ do not have true $\not{E}_{\mathrm{T}}$, the imposed $\not{E}_{\mathrm{T}}$ threshold helps to suppress these events from entering the signal region and the HPS e-veto helps to further reduce this background contribution.

5.3.2 QCD-multijet Production

The misidentification of jets as electrons or τ_h's gives rise to extensive contamination from QCD-multijet production. While the probability for the misidentification,

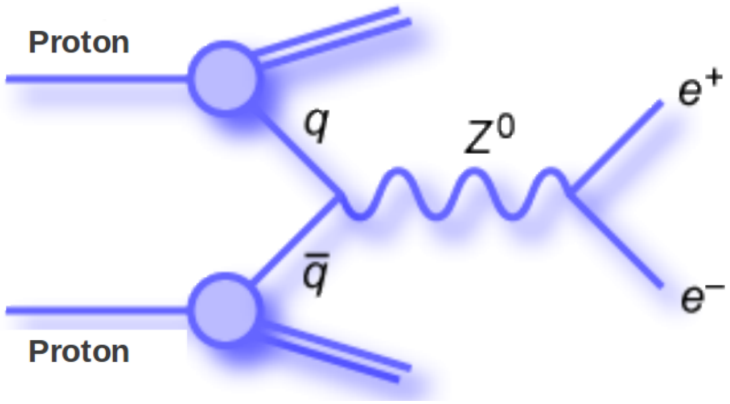

Figure 5.4: $Z/\gamma^* \rightarrow e^+e^-$ Process. Feynman diagram illustrative of the processes that contribute to the leading order production of the neutral weak Z boson decaying to a pair of oppositely charged electrons. Events from $Z/\gamma^* \rightarrow e^+e^-$ can be misidentified as Z' events whenever an electron is misidentified as a τ_h candidate.

or fake rate, is on the order of 10^{-1} for the τ_h and 10^{-3} for the electron, the large cross-section for QCD-multijet introduces a significant background in the signal region. QCD-multijet events (Figure 5.5) arise from direct production of quarks and gluons. Because quarks and gluons do not exist as free particles, they produce additional quark and gluon pairs as they go through a process of hadronization. Thus, QCD-multijet events are characterized by a high multiplicity of low momentum tracks clustered in jets. Jets resulting from the hadronization process typically leave a broad signature in the detector.

Events from non-heavy flavor QCD-multijet production pass the signal event selections when a pair of jets is misidentified as $e\tau_{\mathrm{h}}$ pair. This type of events is greatly reduced by the efficient and robust identification of electron and τ_h objects. QCD-multijet events with heavy flavor jets decaying into leptons also enter the signal region when a high p_{T} electron is produced by a jet emerging from a heavy quark decay (i. e. $b \rightarrow e\nu_e c$). Electrons from heavy flavor decays, as well as electrons

from $\pi^0 \to \gamma\gamma$ followed by conversions, can be misidentified as prompt electrons. Additionally, hadrons in a QCD-jet can be misidentified as the visible products of a τ_h candidate. Due to the broad signature in the detector of the quark and gluon jets, the lepton isolation will play a large role in the discrimination against the QCD-multijet background.

Strong topological discriminators are needed to further suppress QCD-multijet production. Because fragmentation effects largely wash out correlations of the overall jet charge with the parent quark or gluon that originated the jet, there is approximately equal probability for $e\tau_{\rm h}$ candidates with same-sign and opposite-sign electric charge to be selected. This analysis is a search for neutral bosons, thus rejecting same-sign events will allow for a significant suppression of the QCD-multijet background. $\not\!\!E_{\rm T}$ related cuts also help to achieve this since QCD-multijet events have no true intrinsic momentum imbalance and therefore typically have low measured $\not\!\!E_{\rm T}$.

5.3.3 $W + jets$ Production

Events from W boson production in association with jets, $W + jets$ (Figure 5.6), when the associated quark/gluon jets is misidentified as an electron or τ_h candidate and the W boson decays into a well isolated lepton (i.e. $W \to \tau\nu_\tau \to \tau_h\nu_\tau\bar{\nu_\tau}$, $W \to \tau\nu_\tau \to e\nu_e\nu_\tau$ or $W \to e\nu_e$). $W + jets$ contamination can also come from events with a jet from hadronic W decays ($W \to q\bar{q}$) faking a τ_h candidate that passes the event selections if one of the other jets is misidentified as an electron, although at a lower rate than the previous case.

The probability for a quark/gluon jet to be misidentified as a τ_h is typically $\sim 10 - 100$ times higher than for it to be misidentified as an electron. Therefore, the dominant $W + jets$ background emerges when a well-isolated electron from a W de-

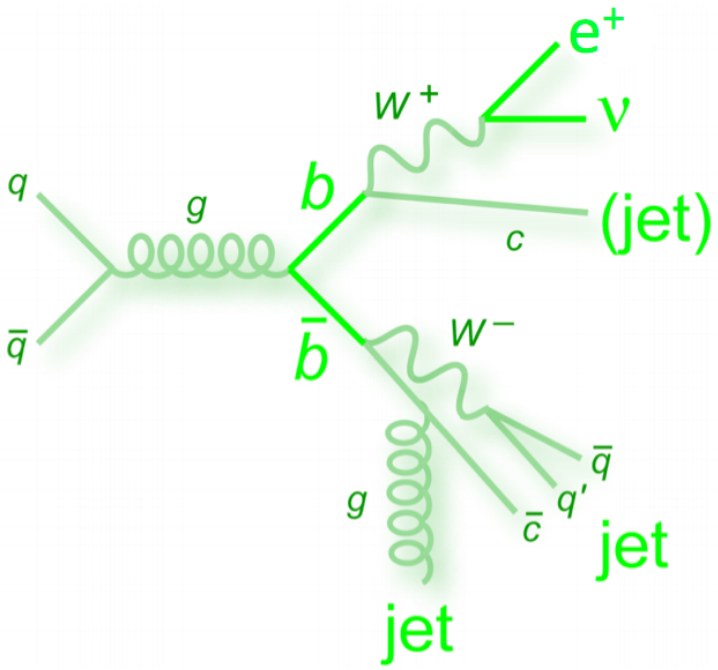

Figure 5.5: QCD-multijet Process. Feynman diagram illustrative of the processes that contribute to the leading order production of QCD-multijet events. Jets from this process can be misidentified as τ_h and electron candidates and heavy quark decays can produce leptons. Combinations of misidentification and leptons from heavy quark decays can mimic the Z′ signal signature.

cay is identified as the electron candidate and one of the associated quark/gluon jets is misidentified as the τ_h candidate. The robust τ identification algorithm and the isolation imposed on the identified τ_h candidates significantly reduces these events. Because of the large mass of the W boson, the prompt electron from the W-decay and the jet do not share the back-to-back topology seen in genuine $e\tau_{\rm h}$ pairs coming from Z$'$ decays. This characteristic will be the basis for the development of topological discriminators against $W + jets$ events. Although $W + jets$ events have real $\not\!\!E_{\rm T}$ due to the neutrino(s) from the W leptonic decays, selections based on $\not\!\!E_{\rm T}$ still have discriminating power. As neutrino(s) take $p_{\rm T} = m_W/2 \sim 40$ GeV/c^2 roughly, the expected $\not\!\!E_{\rm T}$ will be much lower for $W + jets$ events than for Z$'$ events. $W + jets$ events with lower $p_{\rm T}$ jets, such as events with hadronically decaying W bosons, are removed by the applied $p_{\rm T}$ thresholds.

5.3.4 $t\bar{t}$ Production

Events from top pair production ($t\bar{t}$) production (Figure 5.7) have both irreducible and reducible components. The reducible contamination emerges from jets misidentified as prompt lepton (including hadronically decaying tau) candidates. The dominant reducible background comes from a W boson decaying into a well-isolated electron and a jet faking a τ_h. The irreducible part comes from events with the two W bosons decaying to a light lepton (e or μ) and a τ-lepton. $t\bar{t}$ events can also satisfy the event selections since the b-quarks are also produced in top decays ($t \rightarrow bW$) and b's can decay into electrons or into hadrons (faking a τ_h). Isolation requirements greatly suppress the reducible component of the $t\bar{t}$ background. Similar to $W + jets$ events, $t\bar{t}$ events have low correlation between the direction of the lepton and τ_h candidates. Therefore the same topological discriminators can be used to remove them

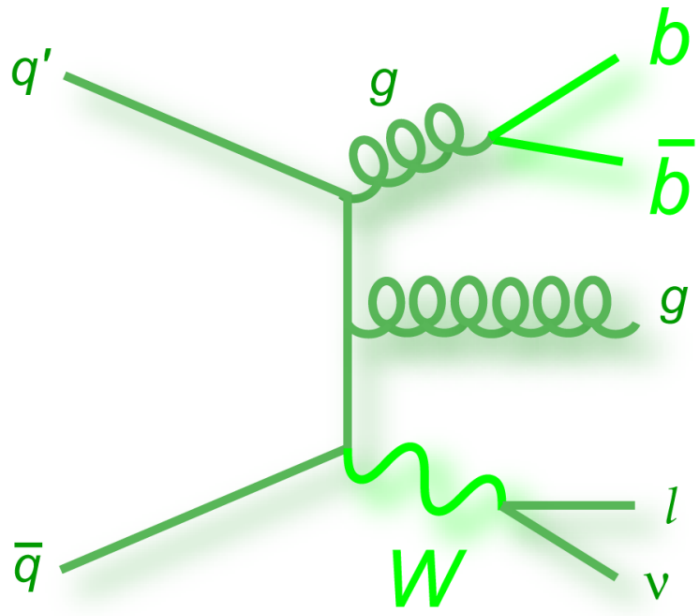

Figure 5.6: $W + jets$ Process. Feynman diagram illustrative of the processes that contribute to the leading order production of the charged weak W boson accompanied by jets. The $W + jets$ events can be misidentifed as Z′ signal events whenever a W decays into a prompt electron and a jet is misidentified as a τ_h candidate.

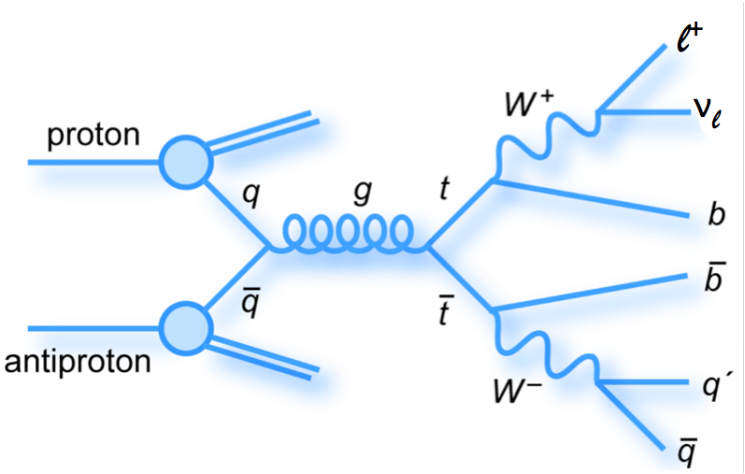

Figure 5.7: $t\bar{t}$ Process. Feynman diagram illustrative of the processes that contribute to the leading order production of top pairs. $t\bar{t}$ events can be misidentified as Z′ signal events whenever the W bosons from top quark decays ($t \to Wb$) produce a prompt light lepton and a τ_h candidate.

from the signal region without significant effect on the signal acceptance. Irreducible $t\bar{t}$ events are introduced in the signal region whenever the two W bosons decay into an electron and a τ_h.

In addition, as events from top pair production will be accompanied by two b-quarks, $b - jet$ identification can be used to distinguish $t\bar{t}$ events from the signal event. The excellent tracking of the CMS detector allows for the robust identification of $b - jets$. The Track Counting High Efficiency (TCHE) b-jet identification algorithm [66] is used for the removal of events with b-jets and plays an important role in suppressing the $t\bar{t}$ background.

5.4 Monte Carlo Simulation Samples

Monte Carlo (MC) simulation is used to mimic actual data events for different production processes, including signal events. We use simulated data to optimize

the analysis techniques and study the properties of the background events. The MC samples have been generated using PYTHIA and MADGRAPH event generators. PYTHIA [71] is a leading order (LO) event generator used to simulate parton-level processes corresponding to tree level Feynman diagrams followed by the Lund string-model based fragmentation, it also emulates effects of higher orders by adding initial and final state QCD radiation. PYTHIA has been used for the generation of the Drell-Yan ($q\bar{q} \rightarrow Z/\gamma^* \rightarrow ll, l = e, \mu, \tau$), QCD-multijet, $t\bar{t}$, WW, and WZ background samples as well as the signal samples (Z'_{SSM}, Z'_{ψ}, Z'_{Stu}).

While PYTHIA provides an accurate description of $2 \rightarrow 2$ processes, being a LO MC, it has deficiencies in simulating events with multiple energetic jets. MADGRAPH [72], which is based on explicit matrix element calculation for X+N jets final states, is better suited for generation of final states including multiple high p_{T} jets. Thus, the $W + jets$ events are modeled with MADGRAPH. MADGRAPH is interfaced with PYTHIA after the initial generation of events in order to perform the parton shower and hadronization. Decays of τ-leptons have been simulated with the TAUOLA [73] package. The TAUOLA package provides the correct branching fractions for τ-lepton decays as well as a proper description of decay kinematics taking into account the tau polarization. Improper modeling of the tau polarization can affect the momentum distribution of the corresponding decay products, reducing accuracy of such simulation.

The generated MC samples also include simulation of multiple interactions per bunch crossing, or *pile-up*. There are two types of pile-up effects, *in-time* and *out-of-time* pile-up. The largest contribution is due to the in-time pileup. In-time pile-up is due to soft pp collisions that happen in the same bunch crossing as the hard scatter. The additional soft collisions create energy deposits that can alter the measurement of $\not\!\!E_{\mathrm{T}}$ or can be merged into the τ or electron reconstruction. Collisions occurring in

bunch-crossings just before and after the collision of interest are the source of *out-of-time* pile-up. Due to the slow drift of some subdetectors, out-of-time pile-up energy deposits can spill into adjacent events. It is necessary to properly add pile-up to the MC samples to appropriately model important physics quantities, such as lepton isolation and $\not\!\!E_{\mathrm{T}}$. The collision data pile-up distribution had not yet been known at the time of the MC sample generation. The samples have been generated with a pile-up distribution expected to cover the range of possible distributions in collision data. In order to accurately account for the pile-up distribution not defined observed in data, it is necessary to re-weight the MC samples. The pile-up distribution in data is estimated using the instantaneous luminosity, as measured by HF, and the total *pp* inelastic cross-section. A ratio between the pile-up distribution in data and in MC is used to determine the resulting weight:

$$w(i) = H^{\mathrm{Data}}(i)/H^{\mathrm{MC}}(i), \tag{5.2}$$

where i denotes the number of pile-up interactions in the event. The effect of the procedure is illustrated in Fig. 5.8.

The signal MC samples are summarized in Table 5.2, while the background sources are summarized in Table 5.3.

5.5 Collision Data Samples and Trigger Paths

The analysis presented in this thesis is based on the data collected by the CMS detector between March and November of 2011. Only data collected during the periods when all essential subdetectors were on and functioning properly have been used for physics analysis. The total integrated luminosity validated for this run

Table 5.2: The Predicted Values of the Production Cross-Section $\sigma(pp \to Z')$ as a Function of the Z′ Mass in the Context of the Sequential Standard Model (SSM) and E_6 Grand Unified Theory. The SSM and E_6 are used as benchmark models for the statistical interpretation of this analysis.

Signal	Mass (GeV/c^2)	σ (pb)
Z'_{SSM}	350	7.51
Z'_{SSM}	500	1.87
Z'_{SSM}	750	0.35
Z'_{SSM}	1000	0.09
Z'_{SSM}	1250	0.028
Z'_{SSM}	1500	0.0093
Z'_{SSM}	1750	0.0037
Z'_{ψ}	350	2.37
Z'_{ψ}	500	0.58
Z'_{ψ}	750	0.10
Z'_{ψ}	1000	0.03
Z'_{ψ}	1250	0.0084
Z'_{ψ}	1500	0.0027
Z'_{ψ}	1750	0.0009
Z'_{Stu}	350	0.0067
Z'_{Stu}	500	0.0064
Z'_{Stu}	600	0.0067

period is 4.94 fb^{-1}.

CMSSW software has been used to reconstruct events in the datasets shown in Table 5.4. High Level Triggers (HLT) performs a pre-selection of raw events to be stored into data samples. For the $e\tau_{\mathrm{h}}$ analysis, we have chosen the data filtered by the various e+τ_h HLT, shown in Table 5.5. A combination of these trigger paths was available during the whole run period. The HLT filtering applied for these triggers preselects events based on the following requirements:

- at least one electron candidate with $p_{\mathrm{T}} > 15$ GeV, 18 GeV, or 20 GeV

Table 5.3: A List of the Simulated Samples for Some of the Dominant Background Processes. These simulated samples have been used in optimizing analysis selections. The table also shows the production cross-section for the corresponding process and the number of simulated events generated.

Sample	σ (pb)	Number of Events
$Z/\gamma^* \to \tau^+\tau^-$	1666	2032536
$Z/\gamma^* \to e^+e^-$	1666	2262653
$W + jets$	31314	81352581
$t\bar{t}$	165	3701947

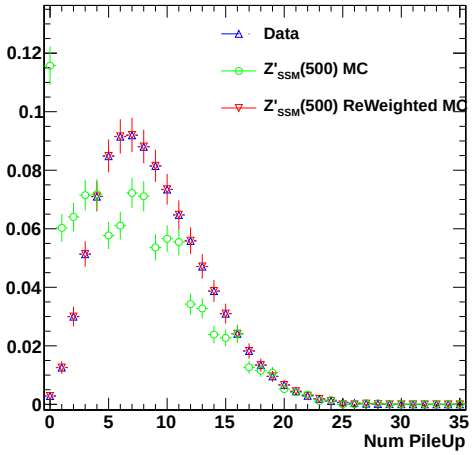

Figure 5.8: Illustration of Pile-up Reweighting. The number of pile-up interactions measured in collision data is shown in the blue open triangles up. This distribution is used to reweight the number of pile-up interactions generated for the Z'_{SSM} (M = 500 GeV/c^2) simulation sample (green open circles). The reweighted number of pile-up interactions for the Z'_{SSM} (M = 500 GeV/c^2) simulation sample is shown in the red triangles pointing down.

- at least one τ candidate with $p_{\mathrm{T}} > 15$ GeV, or 20 GeV and HPS loose or medium isolation, depending on the run period

The trigger efficiency for a true electron to pass the e+τ_h trigger, $\epsilon_e(p_{\mathrm{T}})$, is shown

in Figure 5.9 for the barrel and endcap regions. Figure 5.10 shows the efficiency for a genuine τ_h to pass the e+τ_h trigger, ϵ_{τ_h}, in the barrel and endcap regions. These efficiencies were calculated using the tag and probe method [7]. The measurements of these efficiencies are mutually independent since the trigger paths used to select the electron candidate and tau candidates are uncorrelated. Therefore, the total efficiency for a e+τ_h pair to pass the trigger can be factorized as $\epsilon_{e+\tau_h}(p_{\mathrm{T}}^{e}, p_{\mathrm{T}}^{\tau_h}) = \epsilon_e(p_{\mathrm{T}}^{e}) \times \epsilon_{\tau_h}(p_{\mathrm{T}}^{\tau_h})$. To avoid any large systematic effects and biases due to trigger inefficiency, the p_{T} and η thresholds were chosen where the trigger efficiency reaches a plateau.

Table 5.4: The List of the Datasets. The datasets in this table, which have been used in the analysis, are shown for each of the data taking periods.

Channel	Data Set	$\int \mathcal{L}$
$\ell\tau_{\mathrm{h}}$	/TauPlusX/Run2011A-May10ReReco-v1 /TauPlusX/Run2011A-PromptReco-v4 /TauPlusX/Run2011A-PromptReco-v5 /TauPlusX/Run2011A-PromptReco-v6 /TauPlusX/Run2011B-PromptReco-v1	4.94 fb^{-1}

5.6 Event Selection in the Signal Region

The region where an excess of signal events can be expected if a Z′ exists, the *signal region* (SR), is defined by post-reconstruction event selections that aim to maximize signal sensitivity. The criterion for selecting signal events has been optimized using the MC simulation for signal and background processes. Through the study of backgrounds using simulation, we have developed a set of topological discriminants

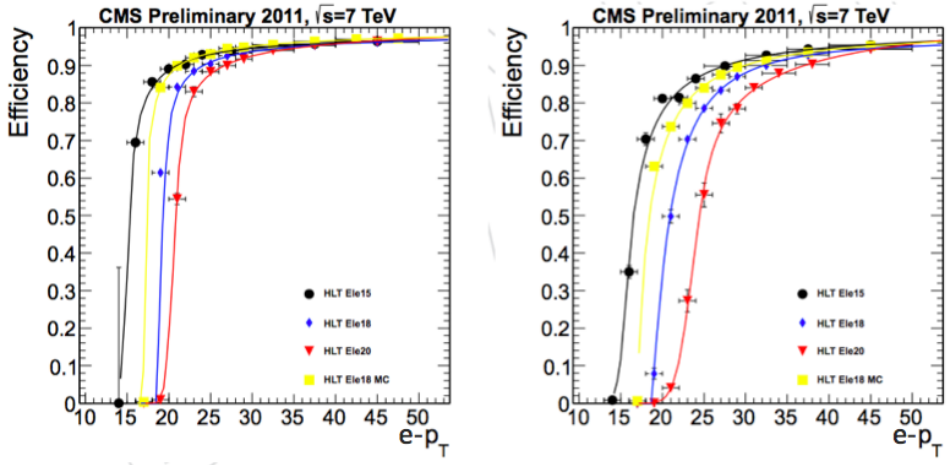

Figure 5.9: Trigger Efficiency Curves for the Electron Candidate of the e-τ_h HLT Trigger as a Function of Electron p_{T} in the Barrel (left) and in the Endcap (right). [7]

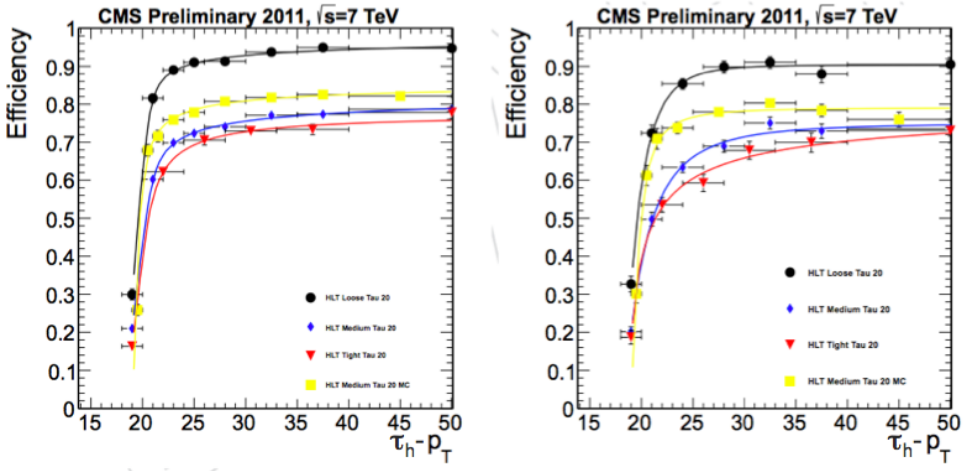

Figure 5.10: Trigger Efficiency Curves for τ_h Candidate of the e-τ_h HLT Trigger as a Function of τ_h p_{T} in the Barrel (left) and in the Endcap (right). [7]

Trigger Path	Run Period
HLT_Ele15_‡_LooseIsoPFTau15*	163269-163869
HLT_Ele15_‡_LooseIsoPFTau20*	165071-167913
HLT_Ele18_‡_LooseIsoPFTau20*	170249-176309
HLT_Ele15_CaloIdVT_TrkIdT_LooseIsoPFTau15*	163269-176309
HLT_Ele18_‡_MediumIsoPFTau20*	175832-180252
HLT_Ele20_‡_MediumIsoPFTau20*	175832-180252

Table 5.5: The List of Trigger Paths Used to Preselect the Events Used in the $e\tau_{\rm h}$ Final State for All Run Periods. (‡CaloIdVT_CaloIsoT_TrkIdT_TrkIsoT)

to reject and minimize the SM background contributions. The requirements used to select events in the $e\tau_{\rm h}$ channel are factorized into four categories: geometric and kinematical acceptance, electron identification and isolation, τ_h identification and isolation, and topological selections. The goal of this analysis is to maximize the selection of signal events with $e\tau_{\rm h}$ final state, while minimizing contributions from all known backgrounds. In addition, we chose event selections that would also preserve the pp$\rightarrow$ Z/$\gamma^* \rightarrow \tau^+\tau^-$ contribution in the low mass region for calibration purposes.

5.6.1 Acceptance Selections

The acceptance requirements are design to avoid kinematic and geometrical regions where the reconstruction and triggering efficiency of physics objects is low and can introduce large systematic uncertainties. A ΔR requirement, where $\Delta R = \sqrt{\Delta\eta^2 + \Delta\phi^2}$, is used to select well separated candidates. Applying a separation in the $\eta - \phi$ space helps to reject $W + jets$ and $t\bar{t}$ events, where a jet that is misidentified as a τ_h candidate is uncorrelated with a well-isolated lepton coming from W decays. Furthermore, it also removes events where a single object passes the selections for electron and τ_h candidates simultaneously resulting in a pair formed by the same

object. The $\Delta R(e, \tau_h) > 0.7$ is well outside the isolation cones of the candidates, $\Delta R < 0.5$ ensuring that the two candidates are not overlapping.

The p_{T} thresholds applied are driven by the p_{T} requirements used to reduce high trigger rate by the $e\tau_{\mathrm{h}}$ trigger paths (Section 5.5). For $p_{\mathrm{T}} > 20$ GeV, both the electron and the τ_h legs of the $e\tau_{\mathrm{h}}$ trigger are on the trigger efficiency plateau (Figures 5.9 and 5.10), which minimizes additional systematic effects due to the knowledge of trigger inefficiency. The sufficiently low p_{T} selection also allows to reconstruct the $\mathrm{Z}/\gamma^* \to \tau^+\tau^-$ peak, where a characteristic average p_{T} scale of τ_h with $p_{\mathrm{T}} \sim 23$ GeV ($\sim$1/2 of $m_Z/2$) and an electron with $p_{\mathrm{T}} \sim 15$ GeV ($\sim$1/3 of $m_Z/2$) are expected, with the rest of the energy being taken up by the neutrinos in the decay. The p_{T} cut also helps us reject events with a soft jet faking an electron from QCD-multijet, $W + jets$ and $t\bar{t}$ backgrounds.

For the reconstruction of electrons and τ_h candidates, which is highly dependent on the limitations of the tracker, η cuts are imposed to avoid geometrical regions where tracking is not available. The detector region covered by the silicon tracker, $|\eta| < 2.5$. Since the isolation cones used in this analysis have a $\Delta R = 0.5$ spread, an $|\eta|$ threshold is chosen to be at 2.1 to avoid effects on due to the track isolation region extending beyond the edge of the silicon tracker.

A summary of the kinematic and geometric acceptance requirements are defined in Table 5.6.

5.6.2 Electron Identification and Isolation Selections

The efficient identification of the electron candidate ensures high efficiency in the selection of a prompt electron. For electron identification, electron candidates are required to be reconstructed by the Gaussian-sum filter (GSF) algorithm (described

Table 5.6: A List of Selections Defining the Kinematic and Geometrical Acceptance of the Analysis.

Candidate	Acceptance Selections
eτ_h	≥ 1 eτ_h pair $\Delta R(e, \tau_h) > 0.7$
electron	≥ 1 e candidate $E_{\mathrm{T}} > 20$ GeV $\lvert\eta\rvert < 2.1$
τ_h	≥ 1 τ_h candidate $p_{\mathrm{T}} > 20$ GeV $\lvert\eta\rvert < 2.1$

in Subsection 4.2.1). In this analysis, the High Energy Electron Pairs (HEEP) selection criteria developed to identify high p_{T} electrons, shown in Table 5.7, are used to identify electron candidates.

Table 5.7: Electron ID and Isolation Selections

ID Variable	Barrel	Endcap
isEcalDriven	1	1
$\lvert\Delta\eta_{\mathrm{in}}\rvert$	< 0.005	< 0.007
$\lvert\Delta\phi_{\mathrm{in}}\rvert$	< 0.09	< 0.09
H/E	< 0.5	< 0.5
$\sigma_{i\eta i\eta}$	N/A	< 0.03
$\mathrm{E}^{n\times m}/\mathrm{E}^{m\times m}$	$\mathrm{E}^{2\times5}/\mathrm{E}^{5\times5} > 0.94$ || $\mathrm{E}^{1\times5}/\mathrm{E}^{5\times5} > 0.83$	N/A
missing hits in inner layer of tracker	0	0

For electron isolation (subsection 4.2.3), absolute isolation on track and electro-

magnetic calorimeter deposits is applied. The isolation is defined within a $\Delta R_{iso} = 0.4$ cone with the following requirements:

- For ECAL isolation: $\sum_{\Delta R<0.4} E_{\mathrm{T}}^{hits} < 4.5$ GeV
  (with thresholds $E_{barrel}^{hit} > 0.08$ GeV, $E_{\mathrm{T}endcap}^{hit} > 0.1$ GeV)

- For the tracker isolation: $\sum_{\Delta R<0.4} p_{\mathrm{T}}^{trk} < 3.5$ GeV/c
  (with thresholds $p_{\mathrm{T}}^{trk} > 0.7$ GeV/c)

Electron isolation efficiently suppresses backgrounds dominated by events where a jet is misidentified as an electron.

5.6.3 Hadronic Tau Identification and Isolation

Efficient and robust hadronic τ reconstruction and identification is crucial for background rejection against SM processes with hadronic jets. The HPS tau reconstruction algorithm (Section 4.6) has been used for τ_h identification. First, PFTau candidates are required to pass the "Decay Mode Finding" HPS discriminant (subsection 4.6.2.1), then the following lepton vetoes are applied:

- ≥ 1 τ passing the HPS "tight" electron veto (see Subsection 4.6.2.3).

- ≥ 1 τ_h passing the HPS "tight" muon veto (see Subsection 4.6.2.3).

The HPS "tight" electron veto is efficient against $\mathrm{Z}/\gamma^* \rightarrow e^+e^-$ events, where an electron can be misidentified as a 1-prong τ_h.

The HPS "medium" isolation working point (subsection 4.6.2.2) is used to select well-isolated τ_h candidates. HPS medium isolation requires no PF charged hadron candidates with $p_{\mathrm{T}} > 0.8\,\mathrm{GeV}$, and no PF gamma candidates with $E_{\mathrm{T}} > 0.8\,\mathrm{GeV}$ in the isolation cone. While HPS medium isolation has a relatively low efficiency

for signal events, 30-40%, it is highly efficient in rejecting multijet backgrounds, for which the selection efficiency is only 1-2%. Since the rate of SM backgrounds is driven by the multiplicity of jets and the large cross-section of backgrounds where a jet is misidentified as a τ_h candidate (QCD-multijet, $W + jets$, and $t\bar{t}$), the jet to τ_h fake rate must be suppressed as much as possible. The selected HPS medium isolation working point is a good balance between maintaining acceptable signal selection efficiency and the strength of the background rejection.

5.6.4 Topological Discriminators

Additional topological selections to target contaminations from specific SM backgrounds have been applied. The topological selections are applied to events that have at least one electron candidate passing acceptance, electron ID and isolation selections and at least one hadronically decaying tau candidate passing acceptance, tau ID and isolation selections.

The new resonance being sought is expected to be very heavy, thus it decays into objects that are back-to-back in the ϕ direction (Figure 5.2). When the heavy resonance under study decays into two τ-leptons with high p_{T}, its neutrinos and visible decay products are highly boosted and collimated along the direction of the mother τ particle. Figure 5.11 illustrates the $\Delta\phi(e, \tau_h)$ separation for a signal and for the $W + jets$ (which is one of the backgrounds this selection allows to suppress), where the uncorrelated jet is not back-to-back with the isolated electron from the W decay. To exploit the back-to-back topology in the ϕ direction of the visible decay products of the τ-leptons a cut on $\cos\Delta\phi(e, \tau_h)$ is applied:

- $\cos\Delta\phi(e, \tau_h) < -0.95$

Since the neutrinos from τ-lepton decays are also boosted along the direction of

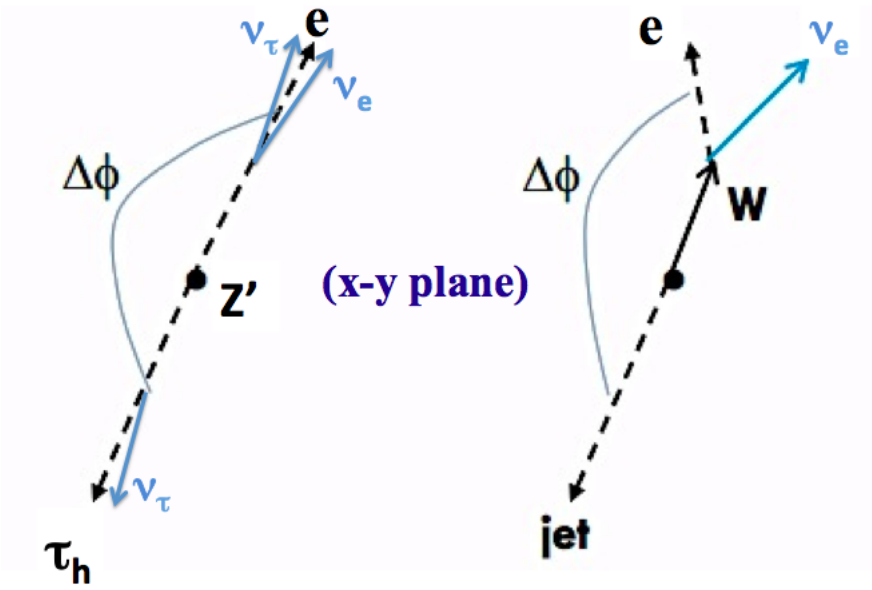

Figure 5.11: An Illustration of the $\Delta\phi(e, \tau_h)$ Separation for Signal and Background Events. The figure illustrates the $\Delta\phi(e, \tau_h)$ separation for the Z′ back-to-back topology (left) and for the $W + jets$ (right), where the uncorrelated jet is not back-to-back with the isolated electron from the W decay.

their mother particle, a discriminator to focus on the back-to-back topology of the neutrinos coming from τ decays, developed by CDF, has been deployed. The CDF p_{zeta} cut [74] is based on two variables, p_ζ and p_ζ^{vis} (equations 5.3 and 5.4).

$$p_\zeta = \vec{p_{\mathrm{T}}^{e}}\hat{\zeta} + \vec{p_{\mathrm{T}}^{\tau_h}}\hat{\zeta} + \vec{\not{E}_{\mathrm{T}}}\hat{\zeta} \tag{5.3}$$

$$p_\zeta^{vis} = \vec{p_{\mathrm{T}}^{e}}\hat{\zeta} + \vec{p_{\mathrm{T}}^{\tau_h}}\hat{\zeta} \tag{5.4}$$

where $\hat{\zeta}$ is the unit vector along the bisector of the visible tau decay products, or the e and τ_h candidates. By projecting the $\not{E}_{\mathrm{T}}$ and visible transverse momenta on the ζ axis, the topology of the neutrinos coming from τ-lepton decays can be used as a discriminator against those coming from W-decays (common to both $W + jets$ and

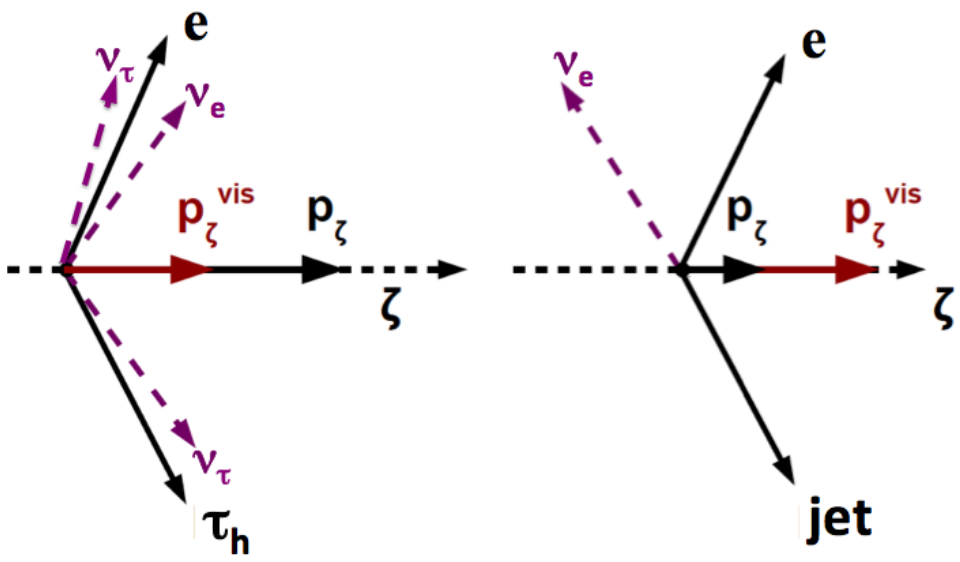

Figure 5.12: An Illustration of the p_ζ Variable. The figure illustrates the p_ζ variable for a typical $Z' \rightarrow \tau^+\tau^-$ event in the back-to-back topology (left) and a typical $W + jets$ event (right)

$t\bar{t}$ backgrounds). The p_ζ cut for this analysis is defined as:

- $p_\zeta - 0.875 \times p_\zeta^{vis} > -7$ GeV

This requirement greatly reduces $W + jets$ and $t\bar{t}$ background contribution in the signal region, where the uncorrelated jet and neutrinos from W-decays give rise to topologies where the jet and the lepton are not back-to-back. Figure 5.12 illustrates the definition of the p_ζ cut variables for a Z′ event and a $W + jets$ event. Since the $\not{E}_{\mathrm{T}}$ due to neutrinos coming from τ decays is expected to be collinear with the visible tau decay products, we expect more positive p_ζ for signal than for a $W + jets$ event. The angle in the $W + jets$ event between the lepton and the neutrino results in a smaller p_ζ.

The search for neutral resonances decaying to two τ-leptons implies opposite-

sign decay products and large missing transverse energy coming from neutrinos, $\not\!\!E_{\rm T}$. Thus, the selected events must have:

- $Q(e) \times Q(\tau_h) < 0$, where $Q(\tau_h)$ is the charge of the τ_h leading track and $Q(e)$ is the charge of the electron candidate
- $\not\!\!E_{\rm T} > 30$ GeV

to reduce QCD-multijet background contribution. While we expect large $\not\!\!E_{\rm T}$ resulting from heavy resonance (for masses $\geq$ 350 GeV/c^2) decays, we select a $\not\!\!E_{\rm T}$ cut low enough to preserve the $Z/\gamma^* \to \tau^+\tau^-$ contribution in the low mass region. As it will be shown in Table 5.9, we can sufficiently reduce backgrounds without harsher cuts.

After the selections described above, $t\bar{t}$ production remains a large background. To reduce this contribution, the presence of $b-jet$ candidates in reconstructed events is used to suppress the remaining contribution of the $t\bar{t}$ contribution in the signal region without damaging signal efficiency since there are no $b-jets$ present in $Z' \to \tau^+\tau^-$ decays. To identify $b-jets$, the medium working point of the CMS b-tagging algorithm, Track Counting High Efficiency (TCHEM), has been used. Jets with $p_{\rm T} > 20$ GeV/c and $|\eta| < 2.5$ are tagged as $b-jets$ if they pass the TCHEM discriminator [66]. By requiring:

- 0 jets tagged as $b-jets$

$t\bar{t}$ contamination and QCD-multijet background with semileptonic $b-jets$ are heavily suppressed without sacrificing signal efficiency. The mis-tag rate of TCHEM is 1% [66].

5.6.5 Selection Efficiencies

Relative efficiencies for the $e\tau_{\mathrm{h}}$ final state selections for simulated SM background samples are shown in Table 5.9. Similarly, Table 5.8 shows the relative efficiencies for simulated SSM Z′ samples with different Z′ masses.

Table 5.8: Relative Efficiency of Each of the Analysis Selection Cuts for Signal Events for Several Choices of the Z′ Mass. The efficiency values shown are obtained using simulation and do not include corrections for known data/simulation differences. The uncertainties shown are statistical only.

Cut/Selection	Z'(350)$\rightarrow \tau\tau$	Z'(500)$\rightarrow \tau\tau$	Z'(750)$\rightarrow \tau\tau$	Z'(1000)$\rightarrow \tau\tau$
$\Delta R(e,\tau_h) > 0.7$	84.67 ± 0.32	87.70 ± 0.29	90.57 ± 0.26	92.11 ± 0.25
$p_{\mathrm{T}}^{e} > 20$	78.47 ± 0.40	84.30 ± 0.35	89.52 ± 0.29	91.47 ± 0.28
$\lvert\eta^{e}\rvert < 2.1$	93.16 ± 0.28	94.59 ± 0.24	95.84 ± 0.20	96.36 ± 0.19
$p_{\mathrm{T}}^{\tau_h} > 20$	78.35 ± 0.47	84.63 ± 0.39	88.23 ± 0.33	89.99 ± 0.32
$\lvert\eta^{\tau_h}\rvert < 2.1$	91.93 ± 0.35	93.39 ± 0.29	95.18 ± 0.23	96.54 ± 0.20
e EcalDriven	98.35 ± 0.17	98.56 ± 0.14	98.26 ± 0.14	98.48 ± 0.14
e $H/E < 0.05$	96.51 ± 0.25	96.84 ± 0.21	97.07 ± 0.19	97.11 ± 0.19
e $\Delta\eta_{\mathrm{in}}$	96.57 ± 0.25	97.19 ± 0.20	97.79 ± 0.17	97.96 ± 0.16
e $\Delta\phi_{\mathrm{in}}$	99.05 ± 0.13	99.12 ± 0.12	99.33 ± 0.09	99.48 ± 0.08
e $\sigma_{i\eta i\eta}$	99.65 ± 0.08	99.75 ± 0.06	99.79 ± 0.05	99.73 ± 0.06
e E^{nxm}/E^{mxm}	97.53 ± 0.22	98.12 ± 0.17	98.24 ± 0.15	98.45 ± 0.14
e MissHits < 1	99.82 ± 0.06	99.79 ± 0.06	99.75 ± 0.06	99.83 ± 0.05
e EcalIso < 4.5	93.26 ± 0.36	91.52 ± 0.36	87.04 ± 0.39	82.39 ± 0.45
e TrkIso < 3.5	98.05 ± 0.20	98.00 ± 0.19	98.08 ± 0.17	98.17 ± 0.17
τ electron veto	71.61 ± 0.67	70.85 ± 0.61	70.58 ± 0.58	71.30 ± 0.59
τ μ veto	96.92 ± 0.30	95.87 ± 0.32	94.2 ± 0.35	92.59 ± 0.41
τ Medium Isolation	37.03 ± 0.86	35.98 ± 0.78	34.12 ± 0.74	33.72 ± 0.76
$\cos\Delta\phi(e,\tau_h) < -0.95$	90.21 ± 0.87	92.49 ± 0.72	94.06 ± 0.63	95.35 ± 0.59
$Q(e) * Q(\tau jet) < 0$	91.72 ± 0.85	92.52 ± 0.75	94.21 ± 0.64	93.58 ± 0.70
$\not\!\!E_{\mathrm{T}} > 30$ GeV	68.46 ± 1.50	76.35 ± 1.25	86.19 ± 0.97	88.36 ± 0.94
$P_\zeta - 0.875 P_\zeta^{vis} > -7$	84.85 ± 1.39	88.95 ± 1.06	88.80 ± 0.96	90.27 ± 0.93
0 b-tagged $jets$	99.46 ± 0.31	98.98 ± 0.36	98.54 ± 0.39	98.47 ± 0.40

Table 5.9: Relative Efficiency of Each of the Analysis Selection Cuts for Background Events for the Dominant SM Background Processes. The efficiency values shown are obtained using simulation and do not include corrections for known data/simulation differences. The uncertainties shown are statistical only.

Cut/Selection	$Z/\gamma^* \to \tau^+\tau^-$	$Z/\gamma^* \to e^+e^-$	$W + jets$	$t\bar{t}$
$\Delta R(e, \tau_h) > 0.7$	100.00 ± 0.00	100.00 ± 0.00	99.99 ± 0.00	100.00 ± 0.00
$p_{\mathrm{T}}^{e} > 20$	44.70 ± 0.12	89.59 ± 0.03	68.33 ± 0.02	61.96 ± 0.03
$\lvert\eta^{e}\rvert < 2.1$	89.47 ± 0.11	95.31 ± 0.02	88.84 ± 0.02	96.83 ± 0.02
$p_{\mathrm{T}}^{\tau_h} > 20$	64.69 ± 0.19	84.06 ± 0.04	50.92 ± 0.03	91.47 ± 0.02
$\lvert\eta^{\tau_h}\rvert < 2.1$	92.65 ± 0.13	86.98 ± 0.04	92.32 ± 0.02	98.16 ± 0.01
e EcalDriven	93.16 ± 0.13	99.18 ± 0.01	96.57 ± 0.02	92.28 ± 0.02
e $H/E < 0.05$	82.69 ± 0.20	99.40 ± 0.01	89.53 ± 0.03	73.01 ± 0.04
e $\Delta\eta_{\mathrm{in}}$	78.46 ± 0.24	98.55 ± 0.02	91.27 ± 0.03	80.61 ± 0.04
e $\Delta\phi_{\mathrm{in}}$	95.47 ± 0.13	98.98 ± 0.01	97.95 ± 0.02	96.25 ± 0.02
e $\sigma_{i\eta i\eta}$	97.75 ± 0.10	99.75 ± 0.01	99.00 ± 0.01	98.76 ± 0.01
e E^{nxm}/E^{mxm}	88.23 ± 0.22	99.14 ± 0.01	95.45 ± 0.02	88.64 ± 0.04
e MissHits < 1	98.69 ± 0.08	100.00 ± 0.00	99.60 ± 0.01	99.57 ± 0.01
e EcalIso < 4.5	94.86 ± 0.16	97.55 ± 0.02	91.65 ± 0.03	78.52 ± 0.06
e TrkIso < 3.5	97.38 ± 0.12	99.26 ± 0.01	97.77 ± 0.01	94.50 ± 0.04
τ electron veto	67.46 ± 0.35	11.10 ± 0.05	78.40 ± 0.05	82.57 ± 0.06
τ μ veto	96.57 ± 0.17	98.99 ± 0.04	98.75 ± 0.01	96.88 ± 0.03
τ Medium Isolation	31.47 ± 0.43	12.79 ± 0.15	1.31 ± 0.02	1.60 ± 0.02
$\cos\Delta\phi(e, \tau_h) < -0.95$	68.40 ± 0.77	65.1 ± 0.59	20.58 ± 0.48	16.27 ± 0.52
$Q(e) * Q(\tau jet) < 0$	91.36 ± 0.56	72.79 ± 0.68	78.70 ± 1.07	83.37 ± 1.30
$\not{E}_{\mathrm{T}} > 30$ GeV	8.88 ± 0.60	4.38 ± 0.37	34.52 ± 1.40	85.34 ± 1.36
$P_\zeta - 0.875 P_\zeta^{vis} > -7$	76.50 ± 2.99	60.29 ± 4.20	48.24 ± 2.51	51.20 ± 2.07
0 b-tagged $jets$	99.35 ± 0.65	100. ± 0.00	97.92 ± 1.03	24.16 ± 2.48

5.7 Background Estimation

The estimation of background rates cannot be taken directly from simulation due to the inevitable imperfections in the modeling as the surviving events are usually very atypical, representing the difficult to model tails of the parameter space. For $\tau^+\tau^-$ final states, a large source of backgrounds is due to misidentification of quark and gluon jets as tau leptons. Such misidentifications happen as a result of rare fluctuations in the process of fragmentation. These rare fluctuations are difficult to model due to complex non-perturbative effects of hadronization. Therefore, simulation predictions for processes where jets from fragmentation are misidentified as τ_h and electron candidates are not expected to agree perfectly with observations in pp collisions. For backgrounds not emerging from jets faking electron or τ_h candidates, such as $\mathrm{Z}/\gamma^* \to \tau^+\tau^-$ and $\mathrm{Z}/\gamma^* \to e^+e^-$, simulation is expected to model both the production and the detector response correctly. However, the reliability of the background estimation given by simulation must still be verified. For example, in the case of $\mathrm{Z}/\gamma^* \to e^+e^-$ complexities in modeling events with an electron being misidentified as a τ_h may arise from the imprecise knowledge of the material and magnetic field or from imperfections in the modeling of electron Bremsstrahlung.

In this analysis, data-driven techniques have been carried out to determine the contributions of SM processes in the signal region. *Control Regions* (CR) are created to study the properties of backgrounds and provide quantitative comparisons between data and predictions of the simulation. The CR selections are chosen to be minimal modifications to signal region selections such that the events in the control region:

- must be kinematically similar or equivalent to the events in the signal region
- do not overlap with the events in the signal region

- are enhanced in background composition, i.e. expected to be mostly events produced from the background under investigation

The contribution of the background in question can be evaluated by using the control regions to extrapolate to the signal region. More than one control region may be required depending on the variables that will need to be evaluated. The main control region represents a collision data sample with high purity of events produced by the background in question. A ratio, determined by the efficiencies of the modified selections used to create the control regions, is used to weight the high purity sample and determined the contribution of the background in the signal region. Additional control regions are created to measure the efficiencies used to extrapolate to the signal region. If control regions show that the background in question is reliably predicted by simulation, a scale factor approach may be used. In this case, the ratio will be a scale factor between collision data and background expectations in the control region.

5.7.1 $t\bar{t}$ Background Estimation

The important characteristics of $t\bar{t}$ events in the signal region are:

- 2 $b-jets$ in top pair production in the final state from top-quark decay ($t \rightarrow bW$).
- the objects identified as the electron and τ_h candidates do not have back-to-back topology.
- the $\not{E}_{\mathrm{T}}$ associated with $t\bar{t}$ events is not collinear with the identified electron or τ_h candidates.

To create a control region where $t\bar{t}$ is enhanced, the following modifications to the signal region are applied:

- remove the $\cos\Delta\phi(e,\tau_h) < -0.95$ requirement, used to eliminate events from the signal region whose identified electron and τ_h candidates do not have back-to-back topology

- remove the p_ζ cut, $p_\zeta - 0.875 \times p_\zeta^{vis} > -7$, used to reject events where the $\not{E}_{\mathrm{T}}$ is not collinear with the identified electron or τ_h candidates

- remove the $0 - bjet$ requirement using a "medium" (TCHEM) b-tagging [66] discriminant is used to reject events with $b - jets$ in the final state

- require ≥ 1 jet tagged as a $b - jet$ using the TCHEM working point with a $\Delta R(e,\tau_h,jet) > 0.5$ to select final states with at least one $b - jet$.

The removal of the $\cos\Delta\phi(e,\tau_h)$ and p_ζ cuts results in a sample dominated by the $W+jets$ and $t\bar{t}$ contributions. The $b-jet$ requirement ensures that the control region maintains a high statistics sample of $t\bar{t}$ while decreasing the $W+jets$ contamination in the region. Figure 5.13 illustrates regions where signal is expected as well as regions 1a and 1b, where $t\bar{t}$ is enhanced by these modifications. Region 1a contains events that fail the $\cos\Delta\phi(e,\tau_h)$ and p_ζ cuts and have at least one jet tagged as a $b - jet$. Whereas region 1b is composed of events pass the $\cos\Delta\phi(e,\tau_h)$ and p_ζ cuts and have at least one jet tagged as a $b - jet$. The $t\bar{t}$-CR1 is defined as a combination of regions 1a and 1b.

The expected event rates obtained using simulation and the observed events in collision data are shown in table 5.10. The contributions due to other SM backgrounds in this control region ($\mathrm{Z}/\gamma^* \rightarrow \tau^+\tau^-$, $\mathrm{Z}/\gamma^* \rightarrow e^+e^-$, and $W+jets$) are predicted by MC are subtracted from the observed data events to calculate the purity in this control region. $\mathrm{Z}/\gamma^* \rightarrow \tau^+\tau^-$ and $\mathrm{Z}/\gamma^* \rightarrow e^+e^-$ are expected to be reliably predicted by simulation. A purity of 72% is achieved in the control region

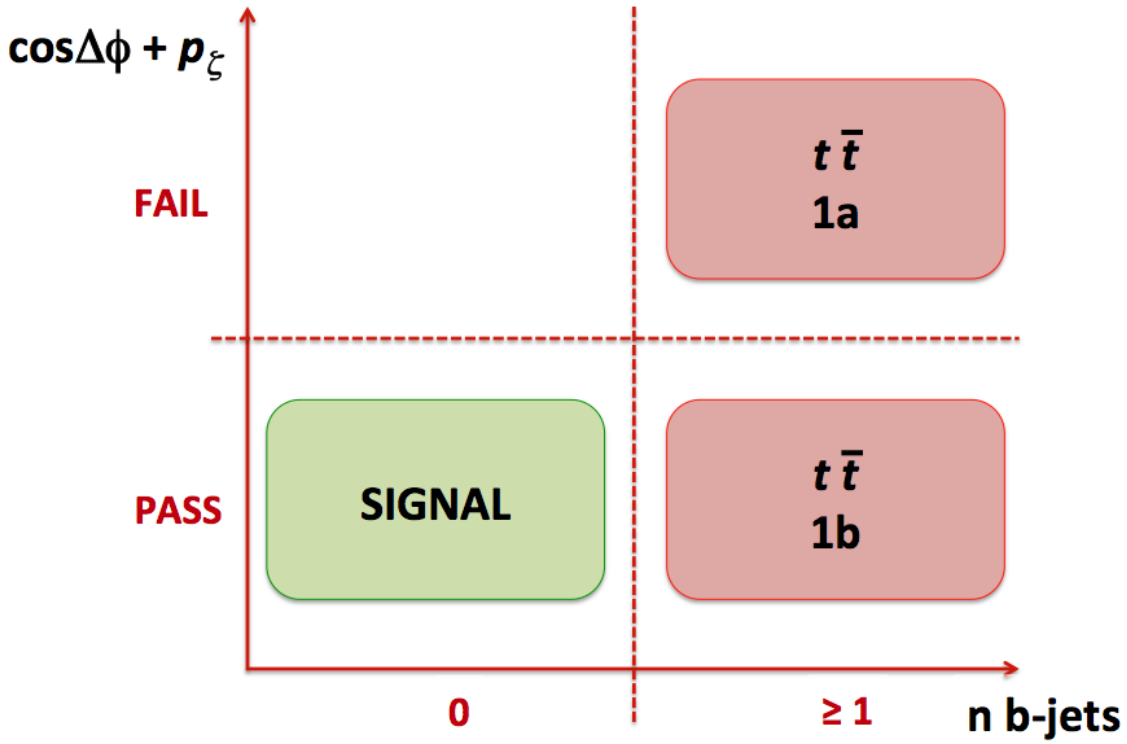

Figure 5.13: An Illustration of the Control Regions Used to Evaluate the Contribution of the $t\bar{t}$ Background. High purity of $t\bar{t}$ events is obtained by the removal of $\cos\Delta\phi(e,\tau_h)$ and the p_ζ cuts and the requirement of at least one $b-jet$. The main $t\bar{t}$-CR1 is composed by regions 1a and 1b. The region labeled as "signal" is defined by the main event selections for this analysis and is where most of the $Z' \to \tau\tau$ signal would be expected.

composed of regions 1a and 1b. The main sources of contamination in this region are due to $Z/\gamma^* \to \tau^+\tau^-$ and $W + jets$. The distribution of variables $cos\Delta\phi(e, \tau_h)$, p_ζ, $M_T(e, \not{E}_T)$, and $M(e, \tau_h)$ demonstrate good agreement between collision data and the MC prediction of overall shapes in this control region.

Table 5.10: The Expected Yield of Events for Each of the Dominant Contributions in the Main $t\bar{t}$ Control Region Obtained Using Simulation is Shown Along with the Number of Observed Collision Data Events.

Source	Events
QCD-multijet	0
$W + jets$	85 ± 11
$Z/\gamma^* \to \tau^+\tau^-$	83 ± 16
$Z/\gamma^* \to e^+e^-$	$15. \pm 6.7$
Total non-$t\bar{t}$ Events, $N_{t\bar{t}-\mathrm{CR1}}^{MC(W+jets, Z/\gamma^*\to\tau^+\tau^-, Z/\gamma^*\to e^+e^-)}$	183 ± 21
$t\bar{t}$, $N_{t\bar{t}-\mathrm{CR1}}^{MC(t\bar{t})}$	459.0 ± 8.8
Data, $N_{t\bar{t}-\mathrm{CR1}}^{Data}$	629

The $t\bar{t}$ events in the signal region are calculated using Equation 5.5:

$$N_{\mathrm{Signal}}^{t\bar{t}} = N_{1a+1b}^{t\bar{t}} \cdot \epsilon^{(cos(\Delta\phi(e,\tau_h)), p_\zeta)} \cdot \frac{P(\mathrm{NBtag} < 1)}{P(\mathrm{NBtag} \geq 1)}, \tag{5.5}$$

where $N_{t\bar{t}-\mathrm{CR1}}^{t\bar{t}}$ is the number of data events in the primary $t\bar{t}$ control region with the subtraction of $W + jets, Z/\gamma^* \to \tau^+\tau^-$, and $Z/\gamma^* \to e^+e^-$ contamination as predicted by MC:

$$N_{t\bar{t}-\mathrm{CR1}}^{t\bar{t}} = N_{1a+1b}^{Data} - N_{1a+1b}^{MC(W+jets, Z/\gamma^*\to\tau^+\tau^-, Z/\gamma^*\to e^+e^-)} \tag{5.6}$$

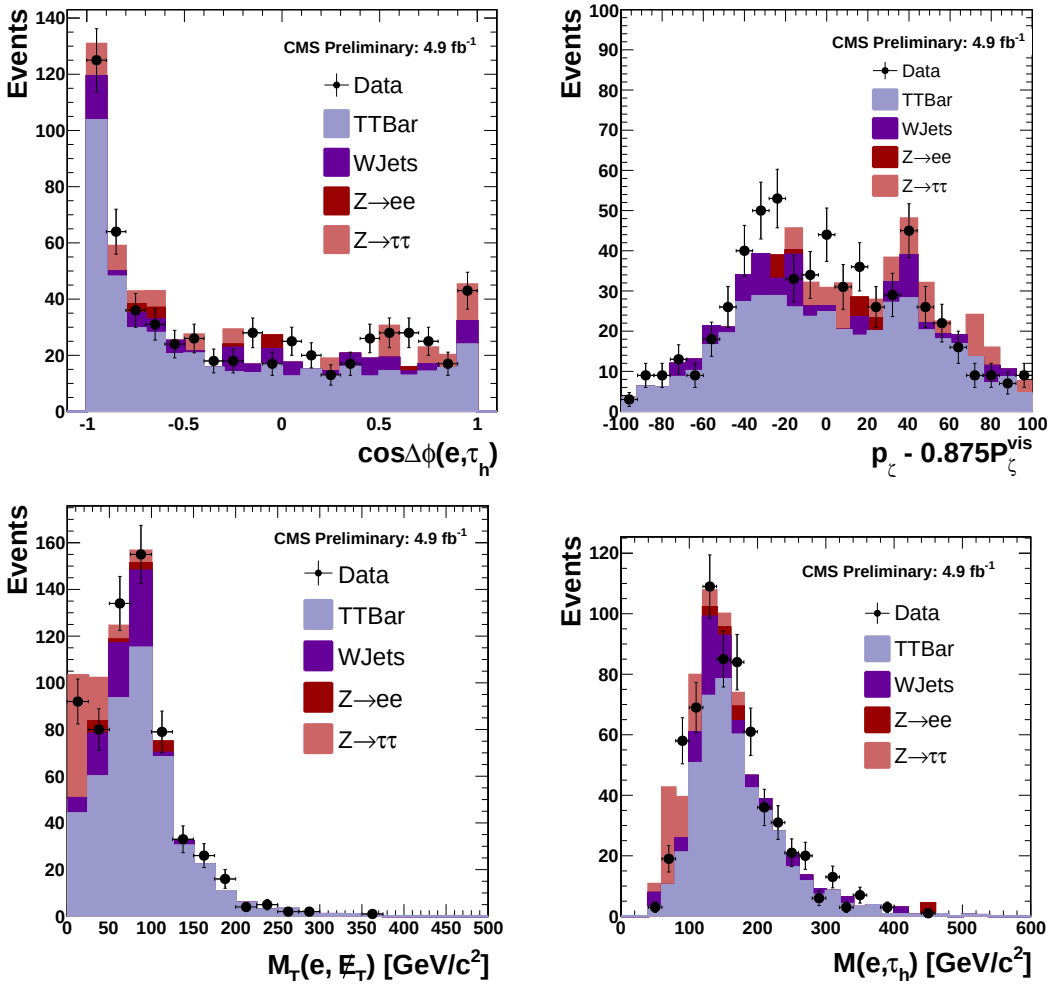

Figure 5.14: The Distributions of the Following Variables (a) $cos\Delta\phi(e,\tau_h)$, (b) p_ζ, (c) $M_T(e,\not{E}_{\rm T})$, and (d) $M(e,\tau_h)$. The distributions for events in the $t\bar{t}$ control region in data are compared to the expected contributions of known background processes as obtained using the simulation.

As shown in Equation 5.5, estimating the $t\bar{t}$ contribution in the signal region requires knowledge of the efficiency of the $cos\Delta\phi(e,\tau_h)$ cut ($\epsilon^{cos\Delta\phi(e,\tau_h)}$) and the p_ζ cut (ϵ^{p_ζ}). In addition, the probability to tag $\geq 1b-jets$ ($P(\text{NBtag}\geq 1)$) is needed. Since the $cos\Delta\phi(e,\tau_h)$ and p_ζ cuts are correlated as they both make use of variables based on the back-to-back topology of objects selected as e and τ_h candidates, the efficiencies

of these selections are measured as a single efficiency, $\epsilon^{(cos\Delta\phi(e,\tau_h),p_\zeta)}$. This single efficiency is determined by the fraction of events passing both $cos\Delta\phi(e,\tau_h)$ and p_ζ cuts (region 1b) over the total number of events (region 1a + region 1b). For an accurate measurement, the predicted non-$t\bar{t}$ MC events are subtracted from each quantity. Equation 5.7 shows the formula used to $\epsilon^{(cos\Delta\phi(e,\tau_h),p_\zeta)}$ in a data-driven way.

$$\epsilon_{t\bar{t}}^{(cos\Delta\phi(e,\tau_h),p_\zeta)} = \frac{N_{1a}^{Data} - N_{1a}^{MC(W+jets,Z/\gamma^*\to\tau^+\tau^-,Z/\gamma^*\to e^+e^-)}}{N_{1a+1b}^{Data} - N_{1a+1b}^{MC(W+jets,Z/\gamma^*\to\tau^+\tau^-,Z/\gamma^*\to e^+e^-)}} \tag{5.7}$$

The $\epsilon^{(cos\Delta\phi(e,\tau_h),p_\zeta)}$ was measured to be 0.096 ± 0.021.

To determine the probability to tag $\geq 1b-jets$ ($P(\text{NBtag} \geq 1)$), a secondary control region is necessary. This region was created using $\mu\tau_\text{h}$ final states by selecting events with at least two jets. The measurement of this efficiency from the $\mu\tau_\text{h}$ channel, where higher purity of $t\bar{t}$ events in this secondary control region is achieved, is applicable in the $e\tau_\text{h}$ channel since b-tagging efficiencies are independent of the final state since both channels share the same kinematic properties. For the secondary $t\bar{t}$-CR2, the $\mu\tau_\text{h}$ signal event selections (Appendix A.2) are modified by:

- removing $\cos\Delta\phi(e,\tau_h) < -0.95$ and p_ζ cut, $p_\zeta - 0.875 \times p_\zeta^{vis} > -7$ cuts
- removing the 0 jets tagged as $b-jets$ using requirement
- requiring at least 2 jets in the event

This control region, as well as the signal region, are illustrated on Figure 5.15. Region 2a contains events where 0 jets are tagged as $b-jets$ and Region 2b contains events where ≥ 1 jets are tagged as $b-jets$, using the TCHEM discriminator. Figure 5.16 shows the distribution of the number of jets tagged as $b-jets$ (TCHEM) in this

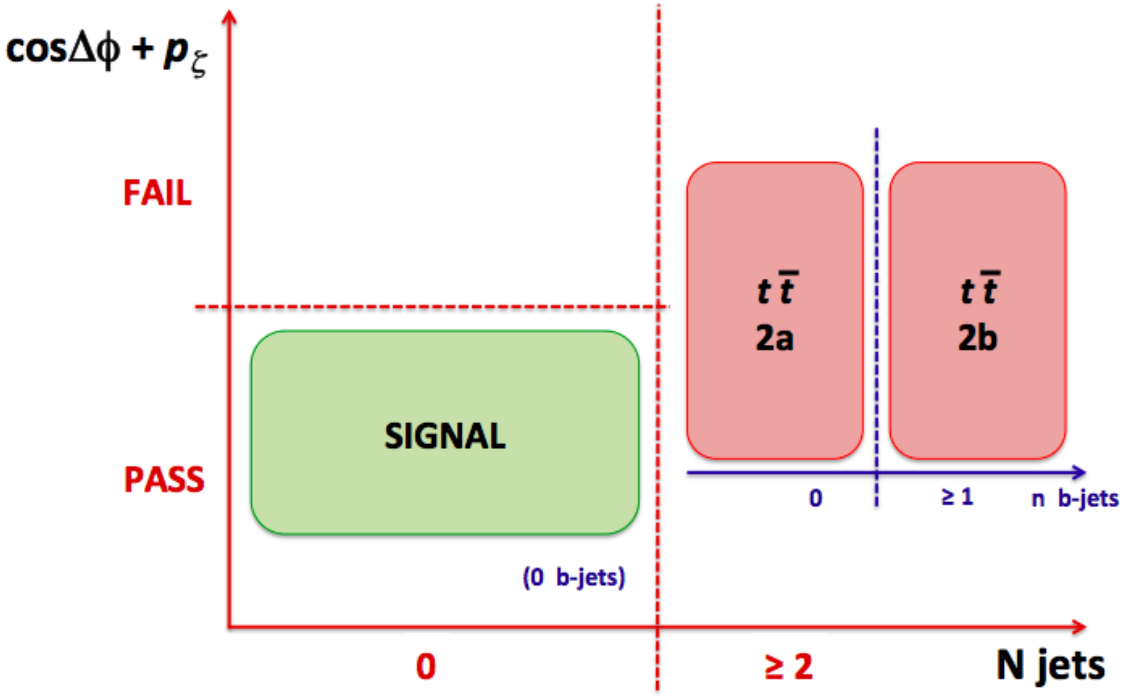

Figure 5.15: An Illustration of a Secondary $t\bar{t}$ Control Region. A secondary $t\bar{t}$ control region is used to evaluate the b-tagging probabilities needed to determine $t\bar{t}$ even contributions in the signal region. Using $\mu\tau_{\mathrm{h}}$ final states, the high purity of $t\bar{t}$ events is obtained by the removal of $\cos\Delta\phi(e,\tau_h)$ and the p_ζ cuts and the 0 $b-jet$ selection. The secondary $t\bar{t}$ CR is composed by regions 2a and 2b. The region labeled as "signal" is defined by the main event selections for this analysis and is where a $Z' \to \tau\tau$ event would be expected.

control region used to obtain the probability to tag 0 $b-jets$, $P(\mathrm{NBtag} < 1) = 0.202 \pm 0.0240$ and $P(\mathrm{NBtag} \geq 1) = 1 - P(\mathrm{NBtag} < 1)$.

A summary of all efficiencies and values used for the extrapolation of $t\bar{t}$ events in the signal region is shown in Table 5.11. Using Equation 5.5, the predicted $t\bar{t}$ rate in the signal region is 10.8 ± 2.8 events.

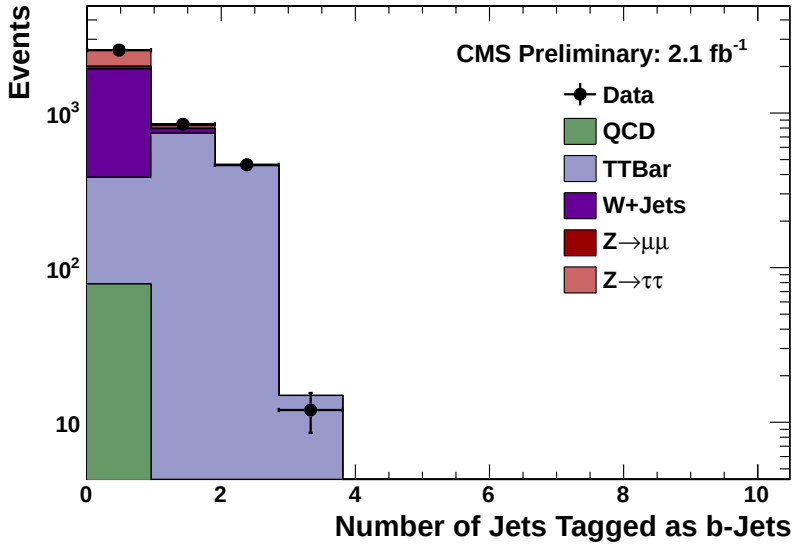

Figure 5.16: The Distribution of the Number of Jets Tagged as $b-jets$ Using the TCHEM Working Point for Events in the Secondary $t\bar{t}$ Control Region. Data events are compared to the expected contributions of known background processes as obtained using the simulation.

5.7.2 $W+jets$ Background Estimation

$W+jets$ events entering the signal region are characterized by:

- the objects identified as the electron and τ_h candidates do not have back-to-back topology.
- the $\not\!\!E_{\mathrm{T}}$ associated with $t\bar{t}$ events is not collinear with either the identified electron or the τ_h.

Similar to $t\bar{t}$, the $\cos\Delta\phi(e,\tau_h) < -0.95$ and $p_\zeta - 0.875 \times p_\zeta^{vis} > -7GeV$ requirements are used to reject $W+jets$ events based on their topology. Removing these selections from the main requirements is not sufficient to create a control region since the signal region would be embeded inside the control region. To create a control

Table 5.11: The Measured Quantities Required for the Calculation of the $t\bar{t}$ Contribution to the Signal Region, using Equation 5.5. These are determined from the $t\bar{t}$ control region using collision data corresponding to 4.9 fb^{-1}. The uncertainties shown are statistical only.

Measured Quantity	
$\epsilon^{(cos\Delta\phi(e,\tau_h),p_\zeta)}$	0.096 ± 0.021
Probability to tag 0 $b-jets$ (TCHEM)	0.202 ± 0.0240
$t\bar{t}$ events in Control Region, $N^{t\bar{t}}_{t\bar{t}-\mathrm{CR1}}$	446. ± 32.
Measured $t\bar{t}$ events in signal region, $N^{t\bar{t}}_{\mathrm{Signal}}$	10.8 ± 2.8
Purity	0.72 ± 0.14

region that contains no signal region events, an additonal requirement on the transverse mass between the electron and the $\not\!\!E_{\mathrm{T}}$, Equation 5.8 is applied. For $W+jets$ events, $M_T(e,\not\!\!E_{\mathrm{T}})$ is expected to be above 50 GeV.

$$M_T(e,\not\!\!E_{\mathrm{T}}) = \sqrt{2p_T^e \not\!\!E_{\mathrm{T}}(1-cos\Delta\phi(e,\not\!\!E_{\mathrm{T}}))} \tag{5.8}$$

In summary, the primary $W+jets$ control region is illustrated on Figure 5.17 as regions 1a and 1b and the modifications used to enhance $W+jets$ events in the control region are defined by:

- removing the $\cos\Delta\phi(e,\tau_h) < -0.95$ and p_ζ cut, $p_\zeta - 0.875 \times p_\zeta^{vis} > -7$ cuts from the signal region selections
- requiring $50 < M_T(e,\not\!\!E_{\mathrm{T}}) < 100$ GeV.

Events that fail the $\cos\Delta\phi(e,\tau_h)$ and p_ζ cuts and have $50 < M_T(e,\not\!\!E_{\mathrm{T}}) < 100$ GeV are in region 1a. region 1b is contains the events pass the $\cos\Delta\phi(e,\tau_h)$ and the p_ζ cuts and fall within $50 < M_T(e,\not\!\!E_{\mathrm{T}}) < 100$ GeV. The primary $W+jets$ control

region is a combination of regions 1a and 1b. The expected event rates obtained using simulation and the observed events in collision data in the primary $W + jets$ control region are shown in Table 5.12. The expected MC contributions due to other SM backgrounds in this control region ($Z/\gamma^* \to \tau^+\tau^-$, $Z/\gamma^* \to e^+e^-$, and $t\bar{t}$) are subtracted from the observed data events to calculate the purity in this control region. A purity of 87% is achieved in the primary control region composed of regions 1a and 1b. Contamination in this region is mainly from DY events. The distribution of variables $cos\Delta\phi(e, \tau_h)$ and $M(e, \tau_h)$ demonstrate good agreement between collision data and the MC prediction of overall shapes in this control region.

Table 5.12: The Expected Yield of Events for Each of the Dominant Contributions in the Main $W + jets$ Control Region Obtained Using Simulation is Shown Along with the Number of Observed Collision Data Events.

Source	Events
QCD-multijet	0
$t\bar{t}$	$52. \pm 2.8$
$Z/\gamma^* \to \tau^+\tau^-$	$181. \pm 23.$
$Z/\gamma^* \to e^+e^-$	$307. \pm 30.$
Total non-$W + jets$ MC Events, $N_{W+jets-\mathrm{CR1}}^{MC(t\bar{t},Z/\gamma^*\to\tau^+\tau^-,Z/\gamma^*\to e^+e^-)}$	$540. \pm 38$
$W + jets$, $N_{W+jets-\mathrm{CR1}}^{MC(W+jets)}$	3719 ± 70
Data, $N_{W+jets-\mathrm{CR1}}^{Data}$	3888

The extrapolation of $W+jets$ events to the signal region is done by measuring the efficiency of the $\cos\Delta\phi(e, \tau_h)$ and p_ζ cuts, $\epsilon^{(cos\Delta\phi(e,\tau_h),p_\zeta)}$ in addition to the efficiency of the $M_T(e, \not{E}_\mathrm{T})$ cuts, $\epsilon^{M_T(e,\not{E}_\mathrm{T})}$. The number of events in the signal region is estimated

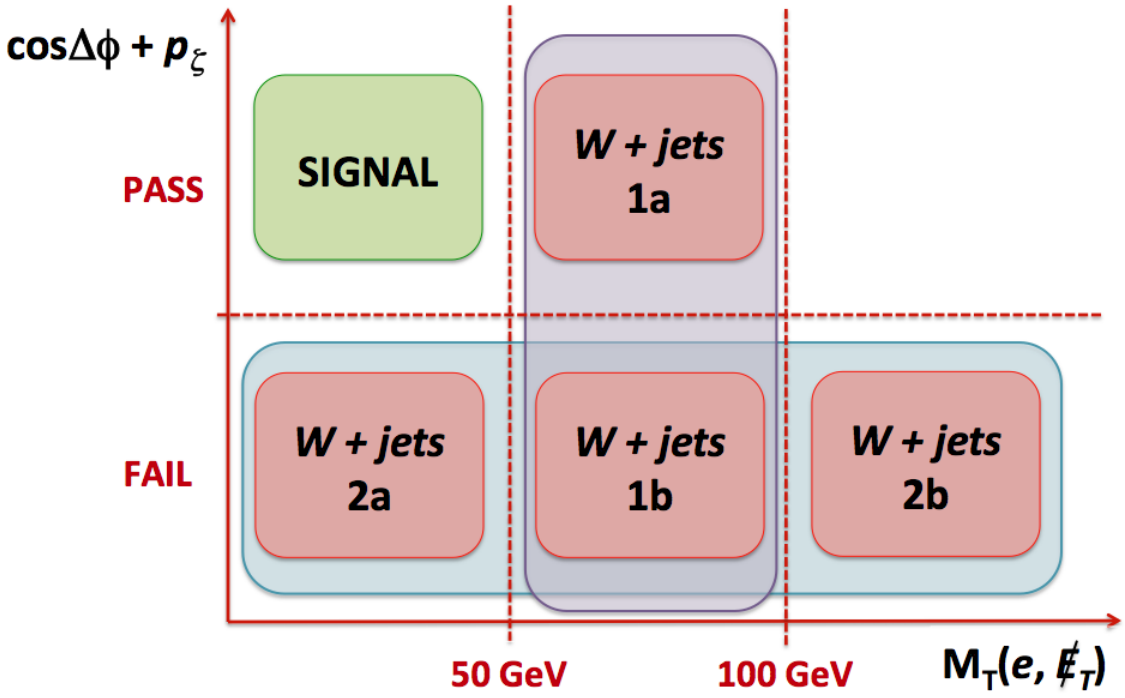

Figure 5.17: An Illustration of the Control Regions Used to Evaluate the Contribution of the $W + jets$ Background. High purity of $W + jets$ events is obtained by the removal of cos $\Delta\phi(e, \tau_h)$ and the p_ζ cuts and the requirement of $50 < M_T(e, \not{E}_{\mathrm{T}}) < 100$ GeV. The main $W + jets$ control region ($W + jets$-CR1) is composed by regions 1a and 1b. A secondary region, $W + jets$-CR2, is composed of regions 2a, 1b, and 2b. The second region is used to measure the efficiency of the $M_T(e, \not{E}_{\mathrm{T}})$ cut. The region labeled as "signal" is defined by the main event selections for this analysis and is where most of the $Z' \to \tau\tau$ signal would be expected.

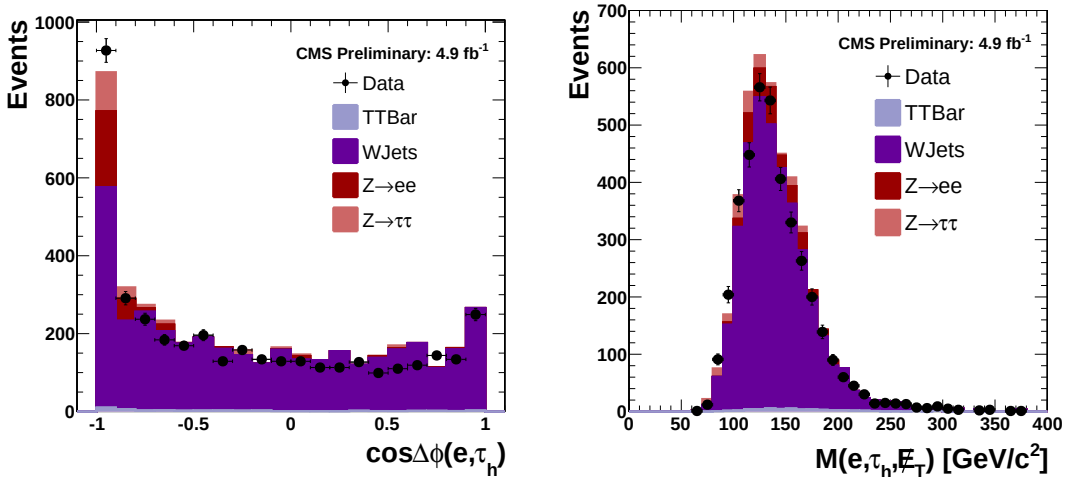

Figure 5.18: The Distributions of the Following Variables (a) $cos\Delta\phi(e,\tau_h)$ and (b) $M(e,\tau_h)$. The distributions for events in the main $W+jets$ control region (CR1) in data are compared to the expected contributions of known background processes as obtained using the simulation.

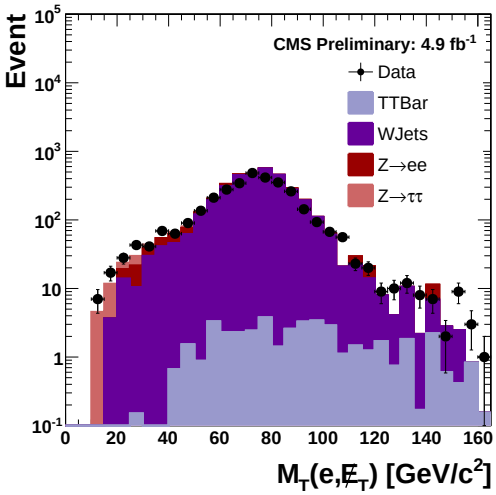

Figure 5.19: The Distributions of $M_T(e,\not{E}_{\rm T})$ for Events in the Secondary $W+jets$ Control Region (CR2). Data events are compared to the expected contributions of known background processes as obtained using the simulation.

using Equation 5.9.

$$N^{W+jets}_{\rm Signal} = N^{W+jets}_{W+jets-1a+1b} \cdot \frac{\epsilon^{(cos\Delta\phi(e,\tau_h),p_\zeta)}_{W+jets}}{\epsilon^{M_T(e,\not{E}_T)}_{W+jets}} \tag{5.9}$$

where $N^{W+jets}_{W+jets-\mathrm{CR1}}$ is the number of data events in the primary $W+jets$ control region ($W+jets$-CR1).

$$N^{W+jets}_{W+jets-\mathrm{CR1}} = N^{Data}_{W+jets-1a+1b} - N^{MC(t\bar{t},QCD,Z/\gamma^*\to\tau^+\tau^-,Z/\gamma^*\to e^+e^-)}_{W+jets-1a+1b} \tag{5.10}$$

$\epsilon^{(cos\Delta\phi(e,\tau_h),p_\zeta)}$, as described in Equation 5.11, is measured in $W+jets$-CR1. The $\epsilon^{(cos\Delta\phi(e,\tau_h),p_\zeta)}$ is equivalent to a ratio between data in region 1a and data in regions 1a and 1b. MC simulation is used to remove the contamination in the control region coming from other SM backgrounds.

$$\epsilon^{(cos\Delta\phi(e,\tau_h),p_\zeta)}_{W+jets} = \frac{N^{Data}_{W+jets-1a} - N^{MC(t\bar{t},QCD,Z/\gamma^*\to\tau^+\tau^-,Z/\gamma^*\to e^+e^-)}_{W+jets-1a}}{N^{Data}_{W+jets-1a+1b} - N^{MC(t\bar{t},QCD,Z/\gamma^*\to\tau^+\tau^-,Z/\gamma^*\to e^+e^-)}_{W+jets-1a+1b}} \tag{5.11}$$

The $\epsilon^{(cos\Delta\phi(e,\tau_h),p_\zeta)}$ was measured to be 0.046 ± 0.009.

A second $W+jets$ control region is needed to measure the efficiency of the additional $M_T(e,\not\!\!E_{\mathrm{T}})$ cut. To create the second $W+jets$ control region, the $\cos\Delta\phi(e,\tau_h)$ and p_ζ cuts are inverted:

- $-0.95 < \cos\Delta\phi(e,\tau_h) < 1.0$
- $P_\zeta - 0.875 \times P^{vis}_\zeta < -7.$

This second control region ($W+jets$-CR2) is composed of regions 2a, 2b, and 1b in Figure 5.17. Similarity, the $M_T(e,\not\!\!E_{\mathrm{T}})$ distribution in the second $W+jets$ control region also shows good agreement between collision data and the MC prediction overall event rates and shapes. The $M_T(e,\not\!\!E_{\mathrm{T}})$ distribution in this control region is shown in Figure 5.19. With this high purity sample, the $\epsilon^{M_T(e,\not\!\!E_{\mathrm{T}})}$ is measured using Equation 5.12.

$$\epsilon^{M_T(e,\not\!\!E_{\mathrm{T}})}_{W+jets} = \frac{N^{Data}_{W+jets-2a+1b+2b}}{N^{Data}_{W+jets-2a+2b}} \tag{5.12}$$

The $\epsilon^{M_T(e,\not{E}_T)}$ measured in $W + jets$-CR2 was 0.85 ± 0.019.

The predicted rates and observed number of events in Control Region 1 is shown in Table 5.12. Using Equation 5.9, the predicted $W + jets$ contribution in the signal region is 181. ± 36. events.

Table 5.13: The Measured Quantities Required for the Calculation of the $W + jets$ Contribution to the Signal Region, Using Equation 5.9. These are determined from the $W + jets$ control regions using collision data corresponding to 4.9 fb^{-1}. The uncertainties shown are statistical only.

Measured Quantity	
$\epsilon^{(cos\Delta\phi(e,\tau_h),p_\zeta)}$	0.046 ± 0.009
$\epsilon^{M_T(e,\not{E}_T)}$	0.85 ± 0.019
$W + jets$ events in the Control Region 1, $N^{W+jets}_{W+jets-\mathrm{CR1}}$	3350 ± 52
Measured $W + jets$ events in the Signal Region	181 ± 36
Purity	0.87 ± 0.02

5.7.3 QCD-multijet Estimation

In ditau analyses, it is crucial to estimate the contribution of QCD-multijet events accurately. These events emerge from the high probability of jets to be misidentified as τ_h candidates (present in $\sim 88\%$ of ditau decays). In the $e\tau_\mathrm{h}$ channel, electrons may come from both heavy flavor quark decays (i.e. $c \to e\nu_e$) or from non-heavy flavor decays ($\pi^0 \to \gamma\gamma \to e$ or a light jet faking an electron). Due to the QCD-multijet events which can have more than 2 jets, although dijet is dominant, more than one $e\tau_\mathrm{h}$ pair candidate that may pass the signal selections. The probability of selecting an opposite-sign (OS) pair, where the electron and τ_h candidates have

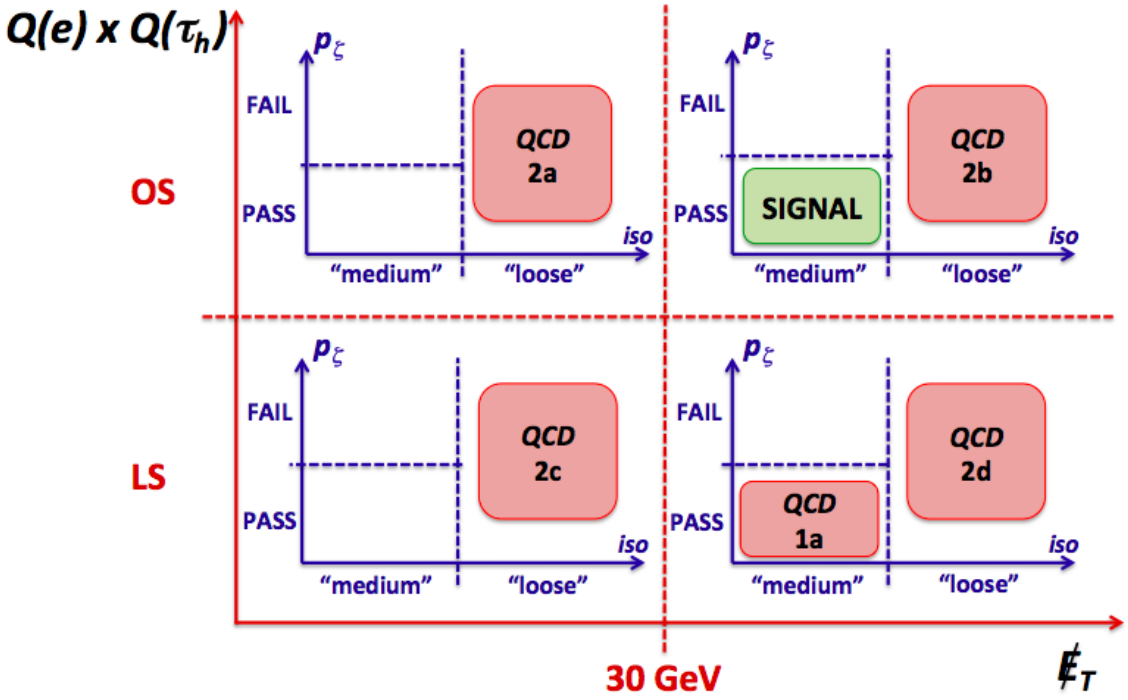

Figure 5.20: An Illustration of the Control Regions Used to Evaluate the Contribution of the QCD Background. The main QCD-multijet rich control region is obtained by the requiring like-sign events to pass the signal region selections and is illustrated by region 1a, QCD-CR1. Regions 2a - 2d are used to calculate the OS/LS ratio, QCD-CR2. The region labeled as "signal" is defined by the main event selections for this analysis and is where most of the $Z' \to \tau\tau$ signal would be expected.

opposite electric charge ($Q(e) \times Q(\tau_h) < 0$), is comparable to the probability of choosing a like-sign (LS) pair, where the electron and τ_h candidates have same electric charge ($Q(e) \times Q(\tau_h) > 0$). Since signal events only contain OS pairs, events with LS pairs passing all other signal selections do not overlap with those coming from Z' decays and are predominatly QCD-multijet events with the same kinematics and topology similar to those in the signal region.

A control region with LS events passing all other signal selections, illustrated in Figure 5.20 as region 1a, is used as the main QCD-multijet control sample, QCD-

CR1. Contamination is expected from backgrounds, such as $W + jets$, that are likely to have real LS pairs as well as backgrounds, such as $\mathrm{Z}/\gamma^* \rightarrow \tau^+\tau^-$, where charge misidentification due to conversions is probable. All contributions to this control region due to SM background are estimated using MC. The difference between the MC estimation of SM backgrounds and the collision data is the QCD LS contribution, $N^{LS\_QCD}_{\text{QCD-CR1}}$.

$$N^{LS\_QCD}_{\text{QCD-CR1}} = N^{Data}_{\text{1a}} - N^{MC(t\bar{t},W+jets,\mathrm{Z}/\gamma^*\rightarrow\tau^+\tau^-,\mathrm{Z}/\gamma^*\rightarrow e^+e^-)}_{\text{1a}} \tag{5.13}$$

where N^{Data}_{1a} is the number of data events and $N^{MC(t\bar{t},W+jets,\mathrm{Z}/\gamma^*\rightarrow\tau^+\tau^-,\mathrm{Z}/\gamma^*\rightarrow e^+e^-)}_{\text{1a}}$ is the non-QCD backgrounds predicted by MC in the QCD-CR1. Table 5.14 shows the number of events in the control region. The invariant mass, $M(e, \tau_h, \not{E}_{\mathrm{T}})$, for the selected $e\tau_{\mathrm{h}}$ candidates is shown Figure 5.21.

Table 5.14: The Expected Yield of Events for Each of the Dominant Contributions in the Main QCD Control Region Obtained Using Simulation is Shown Along with the Number of Observed Collision Data Events. The difference between the total MC (expected like-sign contributions due to non-qcd processes) is due to like-sign QCD-multijet events

Source	Events
$W + jets$	80.0 ± 11.0
$t\bar{t}$	2.07 ± 0.60
$\mathrm{Z}/\gamma^* \rightarrow \tau^+\tau^-$	73.3 ± 15.0
$\mathrm{Z}/\gamma^* \rightarrow e^+e^-$	27.1 ± 9.0
Total MC Non-QCD Events, $N^{MC(t\bar{t},W+jets,\mathrm{Z}/\gamma^*\rightarrow\tau^+\tau^-,\mathrm{Z}/\gamma^*\rightarrow e^+e^-)}_{\text{QCD-CR1}}$	183.0 ± 21.0
Data, $N^{Data}_{\text{QCD-CR1}}$	351

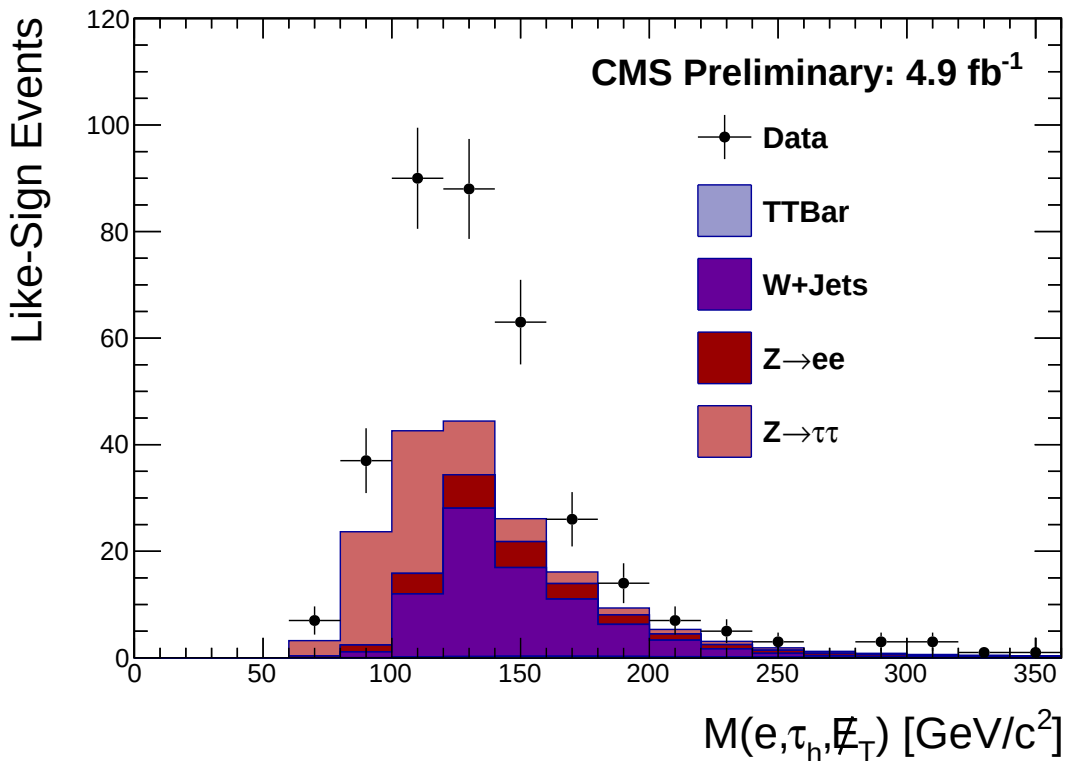

Figure 5.21: The Distribution for $M(e, \tau_h, \not{E}_{\mathrm{T}})$ for Events in the Main QCD-multijet Control Region. Data is compared to the expected contributions of known background processes as obtained using the simulation.

To extrapolate the number of expected QCD-multijet events to the signal region, $N_{\mathrm{1a}}^{LS\_QCD}$ must be scaled by an OS to LS ratio measured in a QCD-multijet enriched control region ($R_{OS/LS}^{QCD}$) as shown in Equation 5.14.

$$N_{\mathrm{Signal}}^{QCD} = N_{\mathrm{1a}}^{LS\_QCD} \times R_{OS/LS}^{QCD} \tag{5.14}$$

A second control region, QCD-CR2, where the OS/LS ratio can be measured, is created by using a sample of data events with non-isolated $l + \tau_h$. However, isolation is applied on both the electron and the τ_h candidates in the $e + \tau_h$ cross-triggers used in this analysis. Non-isolated single electron triggers with low enough thresholds

were only available for a small percentage of the total integrated luminosity. A non-isolated single muon trigger was chosen to create the second control region since the corresponding luminosity was higher than that available for the single electron triggers. The total integrated luminosity corresponding to the non-isolated single muon trigger is 51.5 pb^{-1}. The signal event selections for the $\mu\tau_{\rm h}$ final state (Appendix A.2) are used with the modifications:

- remove $\not\!\!E_{\rm T}$
- remove p_ζ cut
- remove the OS cut, $Q(\mu) \times Q(\tau_h) < 0$, so select both OS and LS pairs
- select non-isolated muons, $4.0 < \Sigma p_T^{trackiso} < 20$ and $4.0 < \Sigma p_T^{ecaliso} < 20$

By removing $\not\!\!E_{\rm T}$ and p_{zeta}, the QCD-multijet contribution is enhanced. Similarity, the removal of the OS cut almost doubles the amount of QCD-multijet events in the control region. The selection of events with non-isolated muons removes the contamination from other backgrounds. Choosing non-isolated muons also assures that the control region and signal region do not share events as the isolation requirement excludes the isolation region used to select signal events. The control region is composed of regions 2a - 2d in Figure 5.20. The OS/LS ratio is calculated by subtracting non-QCD events from regions 2a-2d using MC predictions for $t\bar{t}, W + jets, {\rm Z}/\gamma^* \to \tau^+\tau^-$, and ${\rm Z}/\gamma^* \to e^+e^-$. The OS/LS ratio is determined using:

$$R_{OS/LS}^{QCD} = \frac{N_{\rm 2a+2b}^{OS\_QCD}}{N_{\rm 2c+2d}^{LS\_QCD}} \tag{5.15}$$

The OS/LS ratio, $R_{OS/LS}^{QCD}$, was measured to be 1.10 ± 0.04. The total number of expected QCD-multijet events in the signal region is $185. \pm 32.$.

Table 5.15: The Measured Quantities Required for the Calculation of the QCD-Multijet Contribution to the Signal Region, Using Equation 5.14. These are determined from the QCD-multijet control regions using collision data corresponding to 4.9 fb^{-1}. The uncertainties shown are statistical only.

Measured Quantity	
Opposite-Sign to Like-Sign ratio, $R_{OS/LS}$	1.1 ± 0.04
QCD-multijet events in control region 1, $N^{LS\_QCD}_{\text{QCD-CR1}}$	$169. \pm 28.0$
Measured QCD-multijet events in Signal Region, N^{QCD}_{Signal}	185.0 ± 32.0

5.7.4 $Z/\gamma^* \to e^+e^-$ Estimation

$Z/\gamma^* \to e^+e^-$ events enter the signal region whenever a well-isolated electron is identified as the electron candidate and the other electron is misidentified as a 1-prong τ_h candidate. Inverting the "tight" electron veto to enhance events with electrons passing the tau-ID requirements creates a high-purity $Z/\gamma^* \to e^+e^-$ control region. Since there is no $\not{E}_T$ from neutrinos associated with $Z/\gamma^* \to e^+e^-$, the $\not{E}_T$ cut is removed to further improve purity in this control region. With reference to the signal region $e\tau_h$ event selections, the requirements for the $Z/\gamma^* \to e^+e^-$ control region are:

- remove $\not{E}_T$ cut
- remove "tight" electron veto
- select electrons that are misidentified as τ_h candidates by requiring ≥ 1 τ_h candidate to pass the HPS inverted "tight" electron veto.

The $Z/\gamma^* \to e^+e^-$ control region is labeled on Figure 5.22 as region 1a. Unlike the $W + jets$, $t\bar{t}$, and QCD-multijet backgrounds, $Z/\gamma^* \to e^+e^-$ is expected to be reasonably well modeled by MC. Therefore, the number of $Z/\gamma^* \to e^+e^-$ events in the

signal region, $N_{Signal}^{\mathrm{Z}/\gamma^* \to e^+e^-}$, is estimated by scaling the MC prediction for $\mathrm{Z}/\gamma^* \to e^+e^-$ events in the signal region, $N_{Signal}^{MC\mathrm{Z}/\gamma^* \to e^+e^-}$, with a Data/MC scale factor measured in the control region, $Sc_f^{\mathrm{Z}/\gamma^* \to e^+e^-}$, as shown in Equation 5.16.

$$N_{Signal}^{\mathrm{Z}/\gamma^* \to e^+e^-} = N_{Signal}^{MC(\mathrm{Z}/\gamma^* \to e^+e^-)} \times Sc_f^{\mathrm{Z}/\gamma^* \to e^+e^-} \tag{5.16}$$

The use of a scale factor to determine the $\mathrm{Z}/\gamma^* \to e^+e^-$ contribution is only valid when $Sc_f^{\mathrm{Z}/\gamma^* \to e^+e^-}$ is measured in a high purity control region and there exists good agreement between Data and MC prediction for both event rates and shapes. A good measurement of all contributions to the control region is needed to validate the agreement between collision data event rates and MC predictions. The contributions due to $W + jets$, $t\bar{t}$, and $\mathrm{Z}/\gamma^* \to \tau^+\tau^-$ are taken directly from simulation event predictions. To obtain a more accurate estimation of the QCD-multijet background in this region, N_{1a}^{QCD}, the number of LS collision data events passing the $\mathrm{Z}/\gamma^* \to e^+e^-$ control region selections are weighted by the OS/LS ratio measured in the previous subsection. This approach is taken due to mismodeling of the QCD-multijet background by MC and the low statistics in the QCD-multijet simulation samples.

A 99.4% purity of $\mathrm{Z}/\gamma^* \to e^+e^-$ events is measured for the control region. The event rates predicted by MC and observed number of collision data events, $N_{\mathrm{Z}/\gamma^* \to e^+e^- - CR1}^{Data}$, for this region are shown in Table 5.16. Good agreement in the low mass region, where the $\mathrm{Z}/\gamma^* \to e^+e^-$ peak is expected, is also observed between MC and data for both event rates and shapes (shown in the $M(e,\tau)$ and $\not{E}_{\mathrm{T}}$ distributions in Figure 5.23). The Data/MC scale factor, $Sc_f^{\mathrm{Z}/\gamma^* \to e^+e^-}$, determined by Equation 5.17, was measured to be 0.932 ± 0.0027

$$Sc_f^{\mathrm{Z}/\gamma^* \to e^+e^-} = \frac{N_{1a}^{Data} - N_{1a}^{QCD} - N_{1a}^{MC(t\bar{t},W+jets,\mathrm{Z}/\gamma^* \to \tau^+\tau^-)}}{N_{1a}^{MC(\mathrm{Z}/\gamma^* \to e^+e^-)}} \tag{5.17}$$

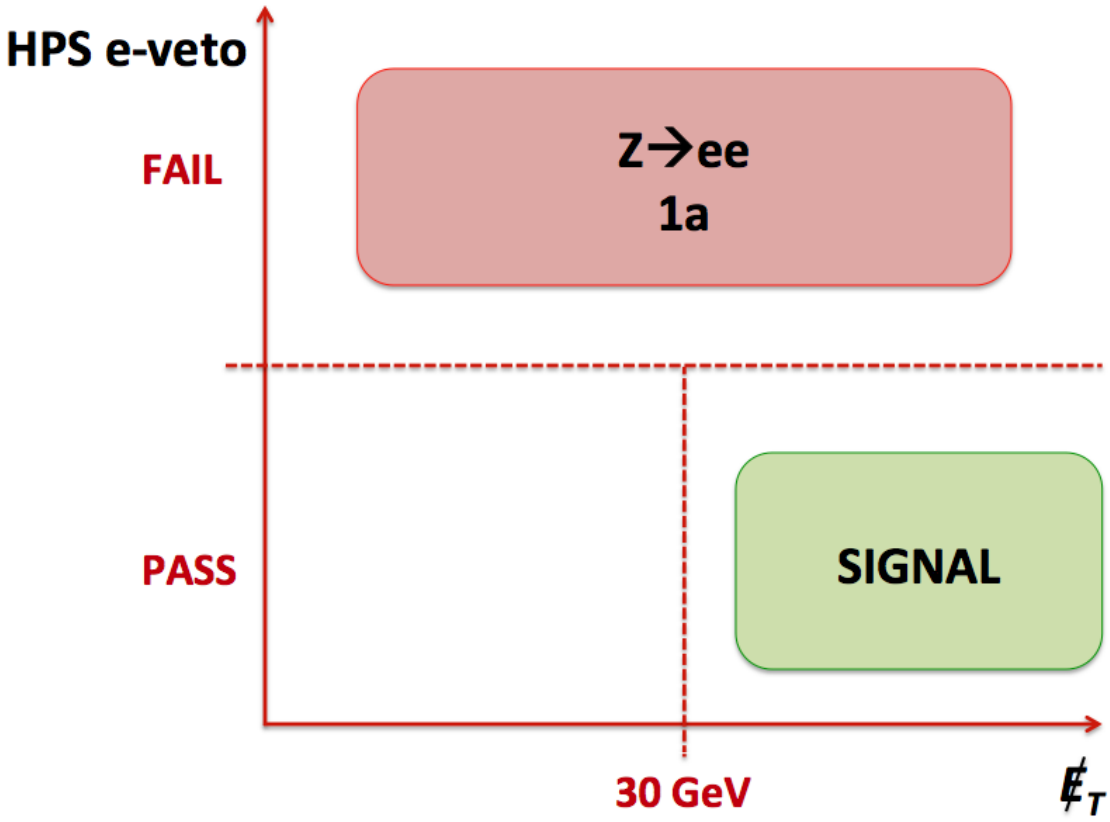

Figure 5.22: An Illustration of the Control Regions Used to Evaluate the Contribution of the $Z/\gamma^* \to e^+e^-$ Background. The $Z/\gamma^* \to e^+e^-$ control region is created by inverting the HPS "tight" electron veto and removing the $\not{E}_T$ cut. The control region is shown as region 1a. The region labeled as "signal" is defined by the main event selections for this analysis and is where most of the $Z' \to \tau\tau$ signal would be expected.

Therefore, using Equation 5.16, the $Z/\gamma^* \to e^+e^-$ estimation in the signal region is scaled to obtain the final $Z/\gamma^* \to e^+e^-$ contribution of $220. \pm 24.$ events.

Table 5.16: The Expected Yield of Events for Each of the Dominant Contributions in the Main $Z/\gamma^* \to e^+e^-$ Control Region Obtained Using Simulation is Shown Along with the Number of Observed Collision Data Events.

Source	Events
$N^{QCD}_{Z/\gamma^* \to e^+e^- - CR1}$	438 ± 175
$W + jets$	213 ± 18
$t\bar{t}$	44.6 ± 2.8
$Z/\gamma^* \to \tau^+\tau^-$	2250 ± 85
Total non-$Z/\gamma^* \to e^+e^-$ events, $N^{MC(t\bar{t},W+jets,Z/\gamma^* \to \tau^+\tau^-)}_{Z/\gamma^* \to e^+e^- - CR1}$	2950 ± 195
$Z/\gamma^* \to e^+e^-$	$462600 \pm 1100.$
Data, $N^{Data}_{Z/\gamma^* \to e^+e^- - CR1}$	434400

5.7.5 $Z/\gamma^* \to \tau^+\tau^-$ Estimation and Validation of τ-ID

$Z/\gamma^* \to \tau^+\tau^-$ events strongly resemble the $Z' \to \tau\tau$ signal signature. Therefore, the signal region event selections are already optimized for $Z/\gamma^* \to \tau^+\tau^-$ events. To create an orthogonal region to the signal region, a restriction on the p_T of the electron candidate is applied, $20 < p_T < 35$ GeV/c, since $Z/\gamma^* \to \tau^+\tau^-$ events have $e\tau_{\mathrm{h}}$ candidates with lower p_T spectrum and are concentrated in the low mass region (< 200 GeV/c^2). Additionally, 1-prong τ_h candidates are required to remove QCD-multijet contamination in this control region. Additional requirements are needed to remove contributions due to QCD-multijet, $Z/\gamma^* \to e^+e^-$, $t\bar{t}$, and $W +$

Table 5.17: The Measured Quantities Required for the Calculation of the $Z/\gamma^* \to e^+e^-$ Contribution to the Signal Region, Using Equation 5.16. These are determined from the $Z/\gamma^* \to e^+e^-$ control region using collision data corresponding to 4.9 fb^{-1}. The uncertainties shown are statistical only.

Measured Quantity	Events
$Sc_f^{Z/\gamma^* \to e^+e^-}$	0.932 ± 0.003
MC prediction of $Z/\gamma^* \to e^+e^-$ events in the Signal Region, $N_{Signal}^{MCZ/\gamma^* \to e^+e^-}$	$236. \pm 26.$
I Measured $Z/\gamma^* \to e^+e^-$ events in the Signal Region, $N_{Signal}^{Z/\gamma^* \to e^+e^-}$	$220. \pm 24.$
Purity	99.4%

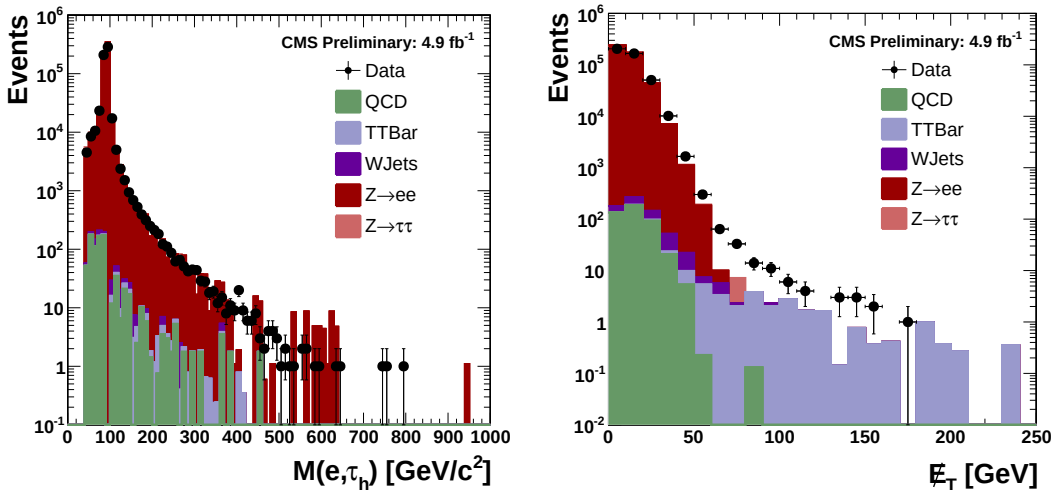

Figure 5.23: The Distributions of the Following Variables (a) $M(e, \tau)$, and (b) $\not{E}_{\mathrm{T}}$ for Events in the $Z/\gamma^* \to e^+e^-$ Control Region. Data is compared to the expected contributions of known background processes as obtained using the simulation.

jets backgrounds. Figure 5.24 shows regions 1a and 1b with the additional cut requirements used to remove contaminations coming from non$-Z/\gamma^* \to \tau^+\tau^-$ events in the control region. These requirements are defined as:

- apply "tight" electron isolation to reduce QCD-multijet contamination
  - Ecal Isolation: $\Sigma \mathrm{E}_{\mathrm{T}}^{ecal} < 2.0$ GeV
    ($\mathrm{E}_{barrel}^{EcalRecHit} > 0.08$ GeV, $\mathrm{E}_{\mathrm{T}endcap}^{EcalRecHit} > 0.1$ GeV, $\Delta \mathrm{R}_{iso} = 0.4$)
  - Track Isolation $\Sigma \mathrm{p}_{\mathrm{T}}^{trk} < 1.0$ GeV ($\mathrm{p}_{\mathrm{T}}^{trk} > 0.7$ GeV, $\Delta \mathrm{R}_{iso} = 0.4$)
- $\not\!\!E_{\mathrm{T}} > 10$ GeV to reduce the QCD-multijet and $\mathrm{Z}/\gamma^* \to e^+e^-$ contributions to the CR
- $M_T(e, \not\!\!E_{\mathrm{T}}) < 40$ GeV to reject $\mathrm{Z}/\gamma^* \to e^+e^-$
- apply $\mathrm{Z}/\gamma^* \to e^+e^-$ veto to further remove $\mathrm{Z}/\gamma^* \to e^+e^-$. The $\mathrm{Z}/\gamma^* \to e^+e^-$ veto removes events with two candidates passing the electron ID and isolation selections and whose invariant mass falls within 3σ of the nominal Z-mass.

with respect to the control region.

Out of all the backgrounds in this analysis, $\mathrm{Z}/\gamma^* \to \tau^+\tau^-$ is expected to be the most accurately modeled by simulation. In addition, the extrapolation to the signal region by measuring the efficiencies of the many modified cuts would introduce high systematic uncertainties. Therefore, the scale factor approach used to determine $\mathrm{Z}/\gamma^* \to e^+e^-$ contribution to the signal region is applied for the estimation of $\mathrm{Z}/\gamma^* \to \tau^+\tau^-$ events. The QCD-multijet events in this control region are also estimated by requiring like-sign pairs that pass the control region selections weighted by the OS/LS ratio measured in Subsection 5.7.3. Along with the estimated QCD-multijet events, the MC estimation of $\mathrm{Z}/\gamma^* \to e^+e^-$, $t\bar{t}$, and $W+jets$ events, $N_{1a+1b}^{MC(t\bar{t},W+jets,\mathrm{Z}/\gamma^* \to e^+e^-)}$, are subtracted from collision data events in the control region, N_{1a+1b}^{Data}, to obtain the scale factor, $Sc_f^{\mathrm{Z}/\gamma^* \to \tau^+\tau^-}$, as shown in Equation 5.18.

$$Sc_f^{\mathrm{Z}/\gamma^* \to \tau^+\tau^-} = \frac{N_{1a+1b}^{Data} - N_{1a+1b}^{QCD} - N_{1a+1b}^{MC(t\bar{t},W+jets,\mathrm{Z}/\gamma^* \to e^+e^-)}}{N_{1a+1b}^{MC(\mathrm{Z}/\gamma^* \to \tau^+\tau^-)}} \tag{5.18}$$

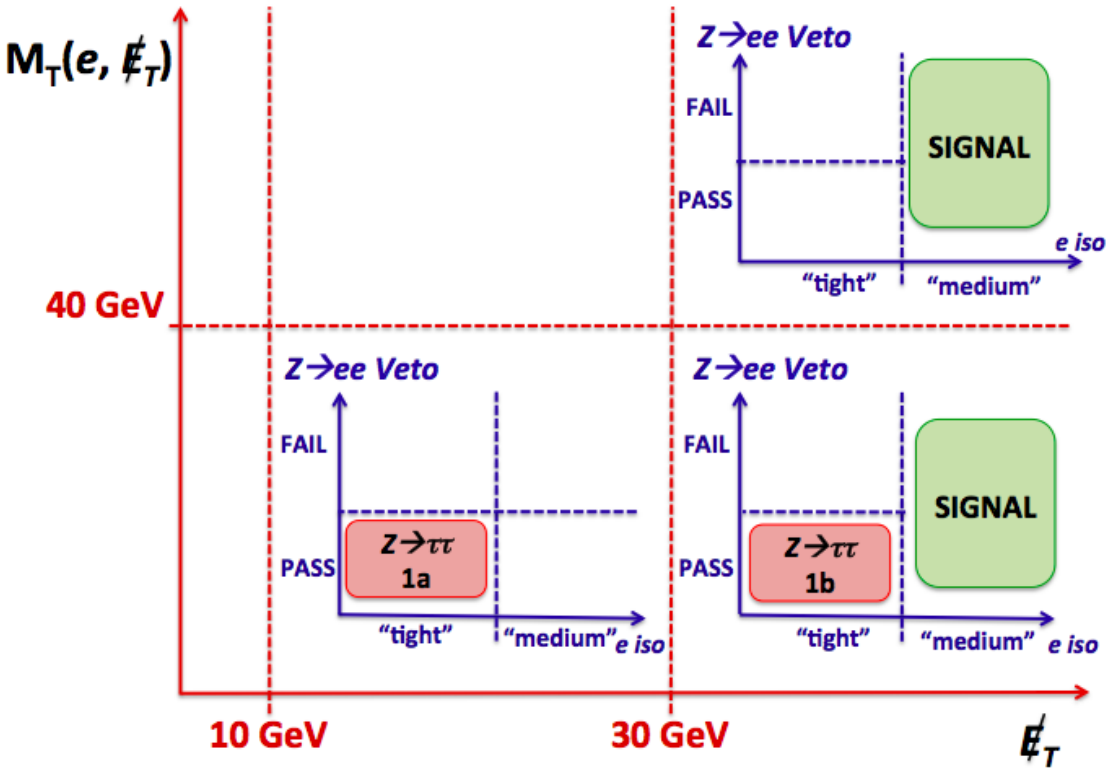

Figure 5.24: An Illustration of the Control Regions Used to Evaluate the Contribution of the $Z/\gamma^* \to \tau^+\tau^-$ Background. Events containing electron candidates with $20 < p_T < 35$ GeV/c and 1-prong τ_h candidates, and that pass all other signal region selections, are required to fall in regions 1a and 1b to create the $Z/\gamma^* \to \tau^+\tau^-$ Control Region, $Z/\gamma^* \to \tau^+\tau^-$-CR1. The region labeled as "signal" is defined by the main event selections, with the exception of electron p_T and 1-or-3-prong decays, for this analysis. However, $Z' \to \tau\tau$ events have electron candidates with higher p_Ts and 3-prong τ_h candidates are also considered, thus the signal region is not fully illustrated in this diagram.

where $N_{1a+1b}^{MC(\mathrm{Z}/\gamma^* \to \tau^+\tau^-)}$ is the number of $\mathrm{Z}/\gamma^* \to \tau^+\tau^-$ events predicted by simulation.

The number of events in the control region is summarized on Table 5.18. The purity $\mathrm{Z}/\gamma^* \to \tau^+\tau^-$ events achieved in this signal region is 69%. Good agreement between MC and Data is shown in the $\not\!\!E_{\mathrm{T}}$ and $M(e, \tau_h)$ distributions shown in Figure 5.25. The scale factor measured using Equation 5.18 is 0.921 ± 0.065. After applying the scale factor to the MC estimation of $\mathrm{Z}/\gamma^* \to \tau^+\tau^-$ events in the signal region, predicted number of $\mathrm{Z}/\gamma^* \to \tau^+\tau^-$ events is $462. \pm 56.$.

Table 5.18: The Expected Yield of Events for Each of the Dominant Contributions in the Main $\mathrm{Z}/\gamma^* \to \tau^+\tau^-$ Control Region Obtained Using Simulation is Shown Along with the Number of Observed Collision Data Events.

Source	Events
QCD	221 ± 21
$W + jets$	52 ± 8.5
$t\bar{t}$	0.42 ± 0.24
$\mathrm{Z}/\gamma^* \to e^+e^-$	$162. \pm 19.$
Total non-$\mathrm{Z}/\gamma^* \to \tau^+\tau^-$ events	$435 \pm 21.$
$\mathrm{Z}/\gamma^* \to \tau^+\tau^-$	$969. \pm 45.$
Data, $N_{\mathrm{Z}/\gamma^* \to \tau^+\tau^- - CR1}^{Data}$	1328

Table 5.19: The Measured Quantities Required for the Calculation of the $Z/\gamma^* \to \tau^+\tau^-$ Contribution to the Signal Region These are determined from the $Z/\gamma^* \to \tau^+\tau^-$ control region using collision data corresponding to 4.9 fb^{-1}. The uncertainties shown are statistical only.

Measured Quantity	Events
Sc_f	0.921 ± 0.065
MC prediction of $Z/\gamma^* \to \tau^+\tau^-$ events in the Signal Region, $N_{Signal}^{MCZ/\gamma^* \to \tau^+\tau^-}$	$502. \pm 50.$
$Z/\gamma^* \to \tau^+\tau^-$ events in the Signal Region, $N_{Signal}^{Z/\gamma^* \to \tau^+\tau^-}$	$462. \pm 56.$
Purity	69%

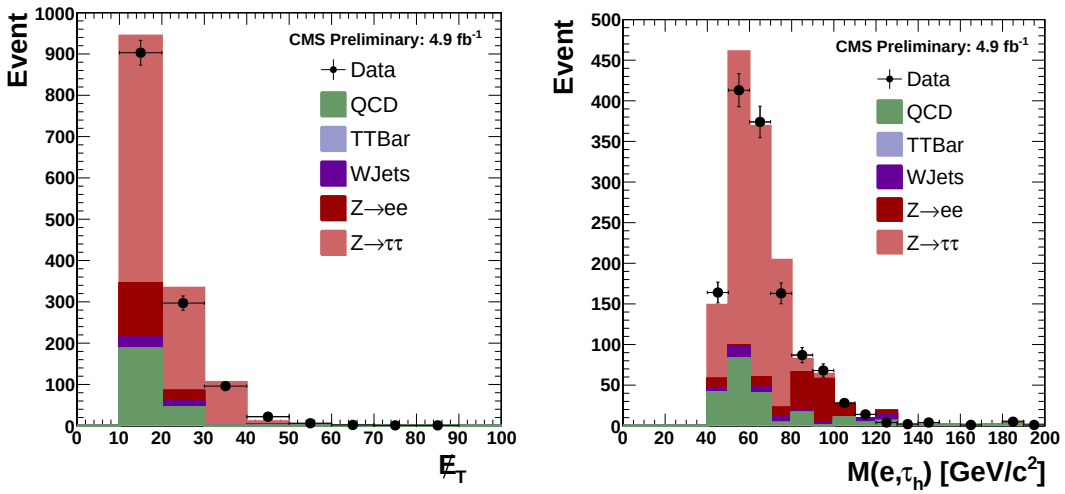

Figure 5.25: The Distributions of the Following Variables (a) $\not\!\!E_{\mathrm{T}}$ and (b) $M(e, \tau_h)$ for Events in the $Z/\gamma^* \to \tau^+\tau^-$ Control Region. Data are compared to the expected contributions of known background processes as obtained using the simulation.

5.8 Data in Signal Region

Once the background studies in the control regions are completed, a last cross-check is performed to verify that the signal selections are able to reconstruct the low mass region. The ratio between the expected number of background events, as calculated from the control regions, and the observed data events for the low mass region ($M(e, \tau_h, \not{E}_{\mathrm{T}}) < 300$ GeV/c^2) is shown in Figure 5.26 and demonstrates good agreement between expectation and data. This validates the robustness of the signal selections and background estimation methods.

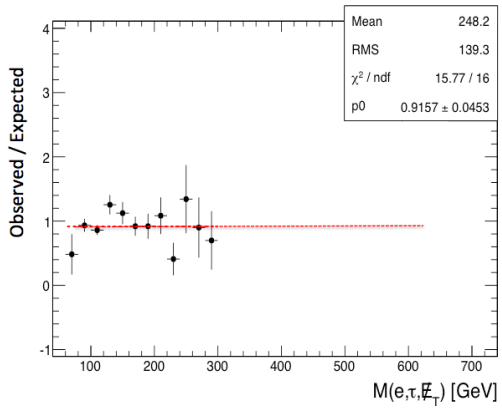

Figure 5.26: The Measured Ratio of the Number of Observed Events in the Date to the Expectation as a Function of $M(e, \tau_h, \not{E}_{\mathrm{T}})$ for Events Satisfying all Signal Selections, but Restricted to the Region of $M(e, \tau_h, \not{E}_{\mathrm{T}}) < 300 GeV/c^2$ GeV

After verifying that we can accurately describe physical processes in the low mass region, the analysis is unblinded. The number of expected background and observed events are shown in Table 5.20 for 4.9 fb^{-1} in the signal region. Figure 5.27 shows the M(e, $\tau_h, \not{E}_{\mathrm{T}}$) distribution in the signal region with Z$'$ mass of 750 GeV/c^2.

Table 5.20: Number of Observed Events in Data and Estimated Background Events for the Whole Mass Range with Statistical Uncertainties for 4.9 fb^{-1}

Sample	Events
QCD	185 ± 31
$W + Jets$	181 ± 36
$t\bar{t}$	10.8 ± 2.8
$Z \rightarrow \tau\tau$	462 ± 56
$Z \rightarrow$ ee	220 ± 24
Total	1058 ± 77
Observed	1043

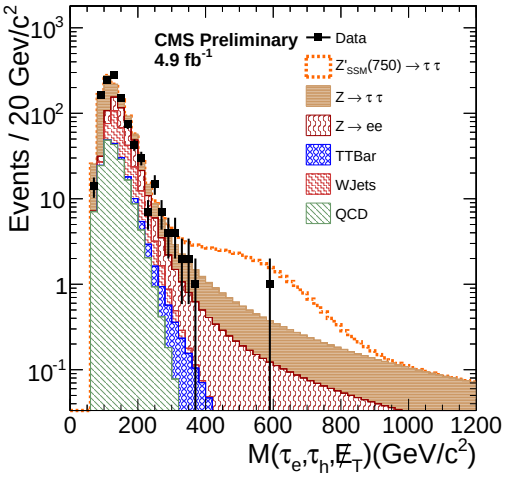

Figure 5.27: The Distribution of the Invariant Mass, $M(\tau_1, \tau_2, \not{E}_T)$, for $e\tau_h$ Final States. The dashed line represents the expectation for the production of the Z'_{SSM} boson, as predicted by the Sequential Standard Model, with a mass of 750 GeV/c^2.

5.9 Systematic Uncertainties

A variety of systematic uncertainties can affect the estimated background and signal event rates in the signal region. It is necessary to evaluate possible sources

of systematic uncertainties in order to appropriately incorporate them into the limit calculation. The sources of non-negligible systematic uncertainties for this analysis are summarized on Table 5.21. The largest source of overall systematic uncertainty is introduced by background estimating methods, mainly due to limited statistics in the control regions.

Table 5.21: Summary of the Sources of Systematic Uncertainties

Source of Systematic	$e\tau_{\mathrm{h}}$
Background Estimation	8.0%
Electron ID	4.5%
Tau ID	6.8%
Tau Energy Scale	2.1%
Tau Trigger	4.0%
Jet Energy Scale	4.0%
Luminosity	2.2%
Parton distribution functions	$4.0 - 6.5\%$
Initial-state radiation	3.1%
Final-state radiation	2.2%

The following systematics have been considered:

- **Background Estimation Uncertainty:** The uncertainty in the number of estimated background events in the signal region arises from both statistical and systematic uncertainties. Statistical uncertainties dominate due to the limited statistics of collision data events in the control regions. MC simulation is used to subtract the contamination from other backgrounds in the control

region; however, this has a negligible effect on the statistical uncertainty. The measurement of efficiencies and scale factors used to determine the number of background events in the signal region come from control regions are included as systematic uncertainties. In addition, the systematic uncertainty on the number of events reported on the final results in Table 5.20 also includes the uncertainty in the LO and NLO cross sections of background processes. Together, the statistical and systematic uncertainty introduce an overall systematic uncertainty of 8.0% to the total number of expected background events in the signal region.

- **Electron ID Efficiency:** Electron trigger, identification, and reconstruction efficiencies are measured using the Tag and Probe method on $Z/\gamma \rightarrow ee$ events in the Z peak region [75]. The efficiencies are measured in data and then compared to simulation to measure simulation-to-data corrections. The electron detection efficiency can be factorized into three components $\epsilon_{tot} = \epsilon_{reco} \times \epsilon_{ID} \times \epsilon_{HLT}$.

  The electron reconstruction efficiency (ϵ_{reco}) is defined as the efficiency for a supercluster to be matched to a reconstructed ECAL driven GSF electron. The data to simulation scale factor was measured for the W and Z cross-section analysis [76], and found to be consistent with 1.0.

  The electron identification efficiency (ϵ_{ID}) is defined as the efficiency for a GSF electron to pass the HEEP identification criteria used to select electron candidates in the $e\tau_{\mathrm{h}}$ signal region, Subsection 5.6.2. The uncertainty takes into account the statistical error on the efficiency measured in the data and MC sample, and the systematic error associated to the choice of the fitting function used to describe the double electron invariant mass.

The electron trigger efficiency (ϵ_{HLT}) is defined as the efficiency for a good (passing the ID criteria) electron to be matched to a trigger primitive. There is a very good agreement between data and simulation and $\epsilon_{HLT}^{DATA}/\epsilon_{HLT}^{MC}$ is compatible with unity.

In Table 5.22 the total correction factors for the electron efficiency are summarized.

Table 5.22: Data/MC Correction Factors for the Total ElectronEfficiency. EB and EE refer to electrons with supercluster in the ECAL Barrel and Endcaps respectively

	$\epsilon_{tot}^{DATA}/\epsilon_{tot}^{MC}$ for ID in $e\tau$ channel
EB, $15 < P_T < 35$ GeV	0.96 ± 0.02
EE, $15 < P_T < 35$ GeV	0.94 ± 0.02
EB, $P_T > 35$ GeV	1.02 ± 0.02
EE, $P_T > 35$ GeV	0.97 ± 0.02

An additional uncertainty of 4.0% is considered due to the electron identification efficiency on the number of pileup interactions. A total of 4.5% systematic uncertainty due to electron reconstruction, identification, and trigger is applied to the number of expected signal events as predicted by MC simulation.

- **Tau ID Efficiency:** The systematic uncertainty associated with the identification of τ_h candidates is extracted from a fit to the $Z \to \tau\tau$ visible mass distribution, $M(\tau_1, \tau_2)$. A relative uncertainty of 6.8% is measured by applying a constraint on the Z production cross section to the measured cross section in

the $Z \to \mu\mu$ and $Z \to ee$ [77]. MC simulation verifies that τ_h identification efficiency is constraint as a function of p_T.

- **Tau Energy Scale:** Systematic effects associated with tau energy scale are measured to have a 2% effect on the signal acceptance. The tau 4-momentum is smeared by a factor of $k = 1.02$ ($p_{smeared} = k \cdot p_{default}$) and variables are recalculated using $p_{smeared}$. By using the $p_{smeared}$ calculated with a factor of $k = \pm 1.02$, the signal acceptance fluctuates by 2%. Therefore, a systematic uncertainty of 2.1% is assigned on the signal acceptance due to tau energy scale.

- **Tau Trigger:** The τ_h trigger efficiency is measured from $Z \to \mu\tau_h$ events selected by the single-muon triggers. The relative uncertainty is 4.0% per τ_h candidate in the $e\tau_{\mathrm{h}}$ final state.

- **Luminosity:** A 2.2% uncertainty on the measured luminosity [78].

- **Jet Energy Scale:** An effect of a 2-5% jet energy scale uncertainty on the signal acceptance (depending on the η and p_T of the considered jet). The jet 4-momentum is measured by a factor of $k = 1.05$ ($p_{smeared} = k \cdot p_{default}$) and variables are recalculated using $p_{smeared}$. $p_{smeared}$ is smeared by a factor of $k = \pm 1.05$, the signal acceptance fluctuates by 4%. Therefore, a 4% systematic uncertainty is assigned on the signal acceptance due to jet energy scale.

- **Parton Distribution Functions (PDF):** The systematic effect due to imprecise knowledge of the parton distribution functions is determined by comparing CTEQ6.6L, MSTW2008nnlo, and NNPDF20 PDF with the default PDF and variations within the family of parameterizations [79, 80, 81]. The maximal

deviation from the central value is used the overall systematic due to PDFs and is measured to be 6.5%.

- **Initial State Radiation (ISR) and Final State Radiation (FSR):** The systematic effect due to imprecise modeling of initial and final state radiation is determined by re-weighting events to account for effects such as missing a terms in the soft-collinear approach [82] and missing NLO terms in the parton shower approach [83]. Systematic uncertainties are 3.1% and 2.2% for ISR and FSR respectively.

5.10 Statistical Analysis

The interpretation of results is presented in terms of CLs limits. A fitting framework has been designed for the statistical interpretation of data and evaluation of signal significance. The Fitter incorporates the effects of systematic uncertainties on normalization and shapes in the calculation of limits for individual channels by marginalization of nuisance parameters. In addition, inter-channel correlations are taken into account when combining the four channels explored in the high mass ditau search, $\mu\tau_{\mathrm{h}}$, $e\tau_{\mathrm{h}}$, $e\mu$, and $\tau_{\mathrm{h}}\tau_{\mathrm{h}}$. The final output provides the 95% CL expected and observed limits for the signal cross section for each channel as well as the combined limit.

5.10.1 The CL_s Method

The framework performs a CL_s fit of data against the expected mass distribution to calculate the binned likelihood:

$$\mathcal{L}(\epsilon_1, \epsilon_2, .., \epsilon_n) = \prod_{i=1}^{Nbins} \mathcal{L}_i(\mu_i, \nu_i) \tag{5.19}$$

where $\mathcal{L}_i$ is the Poisson probability of observing events ν_i in data for bin i, given an expectation of $\mu_i(\sigma)$ events:

$$\mathcal{L}_i = \frac{\mu_i^{\nu_i} e^{-\mu_i}}{\nu_i!} \tag{5.20}$$

To properly calculate the total/joint likelihood, the individual channels are combined as follows:

$$\mathcal{L}_{total} = \mathcal{L}(\mu\tau) * \mathcal{L}(\mathrm{e}\tau) * \mathcal{L}(\mathrm{e}\mu) * \mathcal{L}(\tau_{\mathrm{h}}\tau_{\mathrm{h}}) \tag{5.21}$$

The binned likelihood is used as the test statistic to calculate the 95% CL limit using the CL_s method. CL_s is defined as:

$$CL_s = \frac{CL_{s+b}}{CL_b} \tag{5.22}$$

where CL_{s+b} is the binned likehood for a background + signal hypothesis:

$$CL_{s+b} = \mathcal{P}(obs|s+b) = \prod_{i=1}^{Nbins} \frac{(s_i + b_i)^{\nu_i} e^{-(s_i+b_i)}}{\nu_i!} \tag{5.23}$$

and CL_b is the binned likehood for the background only hypothesis:

$$CL_b = \mathcal{P}(obs|b) = \prod_{i=1}^{Nbins} \frac{b_i^{\nu_i} e^{-b_i}}{\nu_i!} \tag{5.24}$$

In Equations 5.23 and 5.24, s_i is the expected signal, b_i is the expected background, and ν_i is the number of observed events in bin i.

For sensitivity studies, pseudo-data samples are generated, from background only distributions, using a Poisson based random event generator. Figure 5.28a shows an example of a MC based sensitivity study where pseudo-data samples are generated from background only distributions. The pseudo-experiments are used to calculate the expected limits ($\pm 2\sigma$) reported in the next section.

5.10.2 Incorporation of Systematic Uncertainties

Systematic uncertainties can affect the global normalization of the event rate and also create an uncertainty in the knowledge of the mass shape. To incorporate systematic uncertainties into our binned likelihood calculation, MC numerical integration methods are used to integrate over nuisance parameters. The nuisance parameters, α_k, are generated according to a lognormal probability density function for normalizations and Gaussian for mass spectrum uncertainties. If $\epsilon_{\rm n}$ is an efficiency with systematic error $\delta\epsilon$, the likelihood integral becomes:

$$\int \mathcal{L}(\epsilon_1, \epsilon_2, .., \epsilon_n) \mathrm{d}^n\epsilon = N^{-1} \sum_{j=1}^{N} \mathcal{L}(\epsilon_1 + \alpha_1^j \delta\epsilon_1, \epsilon_2 + \alpha_2^j \delta\epsilon_2, .., \epsilon_n + \alpha_n^j \delta\epsilon_n) \qquad (5.25)$$

To incorporate the effects of possible variations in shape, a "morphing" procedure on default, unsmeared mass templates, D_i^{def}, is applied to generate variated templates, D_i^j . Taking into account the smeared templates, the likelihood integral is modified to:

$$N^{-1} \sum_{j=1}^{N} \mathcal{L}(\epsilon_1 + \alpha_1^j \delta\epsilon_1, .., \epsilon_n + {\alpha_n}^j \delta\epsilon_n, D_1^{def} + \alpha_1^j \delta D_1^j, ..., D_n^{def} + \alpha_n^j \delta D_n^j) \qquad (5.26)$$

where $\delta\mathcal{D}_i^k = \mathcal{D}_i^k - \mathcal{D}_i^{def}$ is the difference between the default and the deviated shape for the k^{th} systematic effect. The fitting framework also takes into account

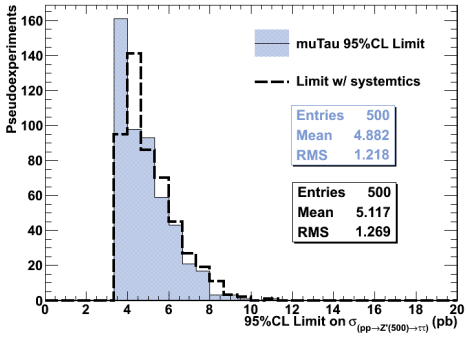

(a) Distribution of the 95% C.L. Limits for a Pseudoexperiment with and without Systematics

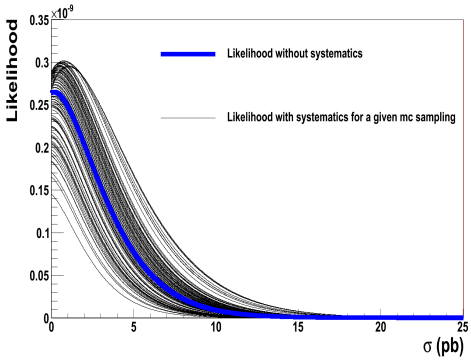

(b) An Illustration of the Effect of Systematic Uncertainties on the Poisson Likelihood for Several Pseudoexperimensts.

Figure 5.28: An Illustration of the Effect of Systematic Uncertainties on the 95% C.L. Limit.

correlations between systematic uncertainties considered in each channel and across channels. For example, to incorporate correlations across channels, the nuisance parameters can be modified as such:

$$\alpha_k = f * \alpha_f + g * \alpha_g, \tag{5.27}$$

where f and g represent the correlated and uncorrelated terms respectively. Figure 5.28b shows the default likelihood (no "smearing" or nuisance parameters incorporated) as well as several likelihood distributions that represent the effect of the nuisance parameters.

5.11 Statistical Interpretation of the Results

The observed mass spectrum does not reveal statistically significant evidence for $Z' \to \tau\tau$ production. Therefore, the 95% C.L. upper limits on the cross-section as a

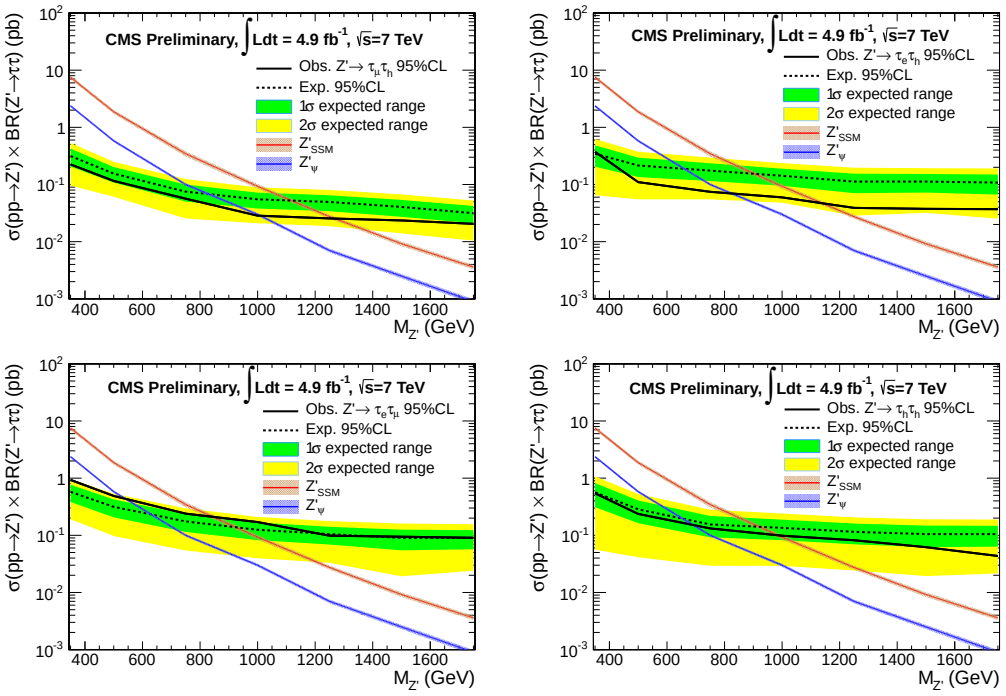

Figure 5.29: 95% CL Upper Limits on the Signal Production Cross-Section as a Function of Z' Mass for (a) $\mu\tau_{\rm h}$, (b) $e\tau_{\rm h}$, (c) emu, and (d) $\tau_h\tau_h$ Channels.

function of Z' mass are calculated. Figure 5.29 shows the upper limits on the cross-section as well as the theoretical cross-section for varying Z' masses in the Sequential Standard Model (SSM). The bands on the expected limits represent the 1σ deviation obtained using a large sample of pseudoexperiments where the pseudodata is obtained from background only distributions using a Poisson based random event generator. Although the $e\mu$ final state is cleaner than the $\mu\tau_{\rm h}$ and $e\tau_{\rm h}$ final states, the upper limit is weaker due to the smaller branching fraction of $\tau^+\tau^-$ to $e\mu$. To determine the upper limits on the Z' mass times the branching fraction to $\tau^+\tau^-$ pairs, the point at which the experimental limit on the cross-section exceeds the theoretical value is determined. One can see from Figure 5.29 that Z'_Ψ and Z'_{SSM} with masses less than 1096 and 1363 GeV, respectively, are excluded at 95% C.L.

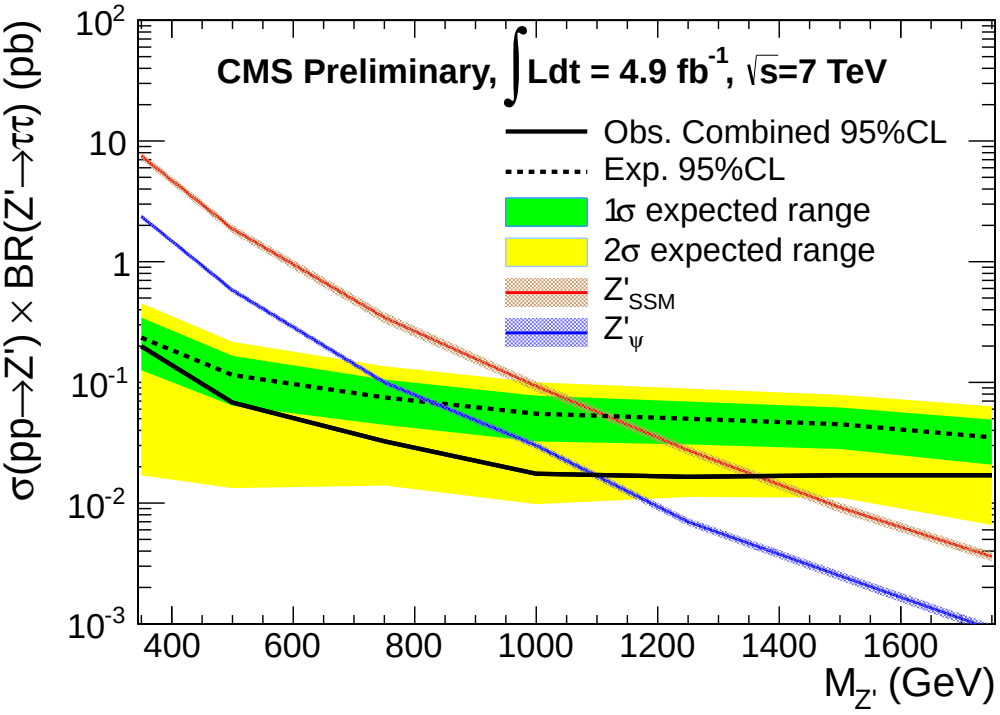

Figure 5.30: The Combined 95% CL Upper Limits on the Signal Production Cross-Section as a Function of Z' Mass.

6. CONCLUSION

The direct search for high mass neutral resonances decaying into ditaus using data recorded by the Compact Muon Solenoid (CMS) experiment, corresponding to an integrated luminosity of 4.94 fb^{-1}, from proton-proton collisions at the LHC with center-of-mass energy $\sqrt{s} = 7$ TeV has been completed. While the data yields no evidence of new physics phenomena within the sensitivity of this measurement, the results of this study significantly reduce the allowed parameter space of models predicting such new bosons. In the context of the Sequential Standard Model (SSM), which predicts a new heavy boson (Z'_{SSM}) with universal couplings, this search allows exclusion of new Z′ bosons with masses lower than 1.4 TeV/c^2. In addition, the results presented in this dissertation are directly applicable to a broad range of other models, predicting such new states, including Grand Unified Theories (GUTs) [38, 20], models with extra spatial dimensions [21], and Supersymmetry (SUSY) [22]. For the Z'_{ψ} predicted by the E_6 GUT, the mass region below 1.1 TeV/c^2 has been excluded by this search. Under the assumption that Z'_{ψ} is assumed to have universal couplings. The search for Z′ bosons decaying into $\tau^+\tau^-$ is of particular importance for models that predict enhanced couplings of the new resonance to third generation particles [23]. In addition, these results significantly extend the range of excluded masses compared to the previous world best limit obtained by the CDF Collaboration, which set the low mass limit at $M_{\text{Z}'} = 399$ GeV/c^2.

Many of the methods and techniques described in this thesis have become the basis for the next generation of searches for production of new neutral bosons at CMS in the final state with two taus as the experiment continues to accumulate new data. In particular, the data that will be accumulated following the upgrade of the

LHC complex to the new center-of-mass energy to 13 TeV in 2015 will provide a unique opportunity for a large extension of the CMS reach for possible production of new heavy bosons. The dissertation particularly focuses on the analysis of the $e\tau_{\mathrm{h}}$ channel and the statistical procedure designed to combine the results of individual decay channels of the search, where the author has been the main contributor. The results were published shortly after this analysis was completed [43].

The results presented continue to impose the most stringent limits for hypothesized high mass resonances decaying into $\tau^+\tau^-$ final states, under the assumption of universal couplings. Recently published results by the ATLAS collaboration [84] are comparable with those reported in these thesis. The search for new heavy bosons decaying into $\tau^+\tau^-$ complements the CMS searches with e^+e^- and $\mu^+\mu^-$ final states, which have provided the current leading results for Z′ searches. These results were obtained by combining pp collision data at $\sqrt{s} = 7$ TeV and $\sqrt{s} = 8$ TeV with the total integrated luminosities of 5.3 and 4.1 fb^{-1}, respectively, and exclude masses below 2.59 TeV for the SSM Z'_{SSM} and 2.26 TeV/c^2 for the E_6 Z'_{ψ} [85].

REFERENCES

[1] D. Kazakov, "Beyond the Standard Model: In search of Supersymmetry," *Joint Institute for Nuclear Research (JINR)*, pp. 125–199, 2000.

[2] C. Das, L. Laperashvili, H. Nielsen, and A. Tureanu, "E6 unification and the hidden sector of the universe," *arXiv:1105.6286*, 2011.

[3] S. Chatrchyan *et al.*, "The CMS experiment at the CERN LHC," *JINST*, vol. 3, p. S08004, 2008.

[4] S. Chatrchyan *et al.*, "Performance of CMS muon reconstruction in *pp* collision events at $\sqrt{s} = 7$ TeV," *JINST*, vol. 7, p. P10002, 2012.

[5] S. Baffioni, C. Charlot, F. Ferri, D. Futyan, P. Meridiani, *et al.*, "Electron reconstruction in CMS," *Eur.Phys.J.*, vol. C49, pp. 1099–1116, 2007.

[6] CMS Collaboration, "Particle–flow event reconstruction in CMS and performance for jets, taus, and $E_{\mathrm{T}}^{\mathrm{miss}}$," CMS Physics Analysis Summary CMS-PAS-PFT-09-001, 2009.

[7] S. Chatrchyan *et al.*, "Search for neutral Higgs bosons decaying to τ pairs in *pp* collisions at $\sqrt{s} = 7$ TeV," *Phys.Lett.*, vol. B713, pp. 68–90, 2012.

[8] S. L. Glashow, "Partial-symmetries of weak interactions," *Nuclear Physics*, vol. 22, p. 579, 1961.

[9] S. Weinberg, "A model of leptons," *Phys. Rev. Lett.*, vol. 19, p. 1264, 1967.

[10] A. Salam, "Weak and electromagnetic interactions," in *Elementary particle physics: relativistic groups and analyticity* (N. Svartholm, ed.), (Stockholm), p. 367, Almqvist & Wiksell, 1968. Proceedings of the eighth Nobel symposium.

[11] F. Englert and R. Brout, "Broken symmetry and the mass of gauge vector mesons," *Phys. Rev. Lett.*, vol. 13, p. 321, 1964.

[12] P. W. Higgs, "Broken symmetries and the masses of gauge bosons," *Phys. Rev. Lett.*, vol. 13, p. 508, 1964.

[13] P. W. Higgs, "Spontaneous symmetry breakdown without massless bosons," *Phys. Rev.*, vol. 145, p. 1156, 1966.

[14] S. Chatrchyan *et al.*, "Observation of a new boson at a mass of 125 GeV with the CMS experiment at the LHC," *Phys.Lett.*, vol. B716, pp. 30–61, 2012.

[15] G. Aad *et al.*, "Observation of a new particle in the search for the Standard Model Higgs boson with the ATLAS detector at the LHC," *Phys.Lett.*, vol. B716, pp. 1–29, 2012.

[16] B. Pontecorvo, "Inverse beta processes and nonconservation of lepton charge," *Sov.Phys.JETP*, vol. 7, pp. 172–173, 1958.

[17] B. Pontecorvo, "Mesonium and anti-mesonium," *Sov.Phys.JETP*, vol. 6, p. 429, 1957.

[18] Z. Maki, M. Nakagawa, and S. Sakata, "Remarks on the unified model of elementary particles," *Prog.Theor.Phys.*, vol. 28, pp. 870–880, 1962.

[19] D. Spergel *et al.*, "First year Wilkinson Microwave Anisotropy Probe (WMAP) observations: Determination of cosmological parameters.," *Astrophys.J.Suppl.*, vol. 148, pp. 175–194, 2003.

[20] J. L. Hewett and T. G. Rizzo, "Low-energy phenomenology of superstring inspired E(6) models," *Phys.Rept.*, vol. 183, p. 193, 1989.

[21] A. Lukas, B. A. Ovrut, and D. Waldram, "On the four-dimensional effective action of strongly coupled heterotic string theory," *Nucl.Phys.*, vol. B532, pp. 43–82, 1998.

[22] S. P. Martin, "A Supersymmetry primer," *Adv.Ser.Direct.High Energy Phys.*, vol. 21, pp. 1–153, 2010.

[23] K. Agashe, H. Davoudiasl, S. Gopalakrishna, T. Han, G.-Y. Huang, *et al.*, "LHC signals for warped electroweak neutral gauge bosons," *Phys.Rev.*, vol. D76, p. 115015, 2007.

[24] V. Aseev *et al.*, "An upper limit on electron antineutrino mass from Troitsk experiment," *Phys.Rev.*, vol. D84, p. 112003, 2011.

[25] K. Assamagan, C. Bronnimann, M. Daum, H. Forrer, R. Frosch, *et al.*, "Upper limit of the muon-neutrino mass and charged pion mass from momentum analysis of a surface muon beam," *Phys.Rev.*, vol. D53, pp. 6065–6077, 1996.

[26] R. Barate *et al.*, "An upper limit on the tau-neutrino mass from three-prong and five-prong tau decays," *Eur.Phys.J.*, vol. C2, pp. 395–406, 1998.

[27] H. Fritzsch, M. Gell-Mann, and H. Leutwyler, "Advantages of the color octet gluon picture," *Physics Letters B*, vol. 47, no. 4, pp. 365 – 368, 1973.

[28] T. D. Lee and C.-N. Yang, "Question of parity conservation in weak interactions," *Phys. Rev.*, vol. 104, pp. 254–258, 1956.

[29] C. S. Wu, E. Ambler, R. W. Hayward, D. D. Hoppes, and R. P. Hudson, "Experimental test of parity conservation in beta decay," *Phys. Rev.*, vol. 105, pp. 1413–1414, 1957.

[30] E. Gildener, "Gauge symmetry hierarchies," *Phys.Rev.*, vol. D14, p. 1667, 1976.

[31] S. Weinberg, "Implications of dynamical symmetry breaking," *Phys.Rev.*, vol. D13, pp. 974–996, 1976.

[32] P. Langacker, "The physics of heavy Z' gauge bosons," *Rev.Mod.Phys.*, vol. 81, pp. 1199–1228, 2009.

[33] A. Leike, "The phenomenology of extra neutral gauge bosons," *Phys.Rept.*, vol. 317, pp. 143–250, 1999.

[34] P. Langacker and M. Plumacher, "Flavor changing effects in theories with a heavy Z' boson with family nonuniversal couplings," *Phys.Rev.*, vol. D62, p. 013006, 2000.

[35] R. Diener, S. Godfrey, and T. A. Martin, "Unravelling an extra neutral gauge boson at the LHC using third generation fermions," *Phys.Rev.*, vol. D83, p. 115008, 2011.

[36] P. Nath, B. D. Nelson, H. Davoudiasl, B. Dutta, D. Feldman, *et al.*, "The hunt for new physics at the Large Hadron Collider," *Nucl.Phys.Proc.Suppl.*, vol. 200-202, pp. 185–417, 2010.

[37] J. D. Anderson, M. H. Austern, and R. N. Cahn, "Tau polarization asymmetry as a probe of Z' couplings," *Phys. Rev. Lett.*, vol. 69, pp. 25–27, Jul 1992.

[38] H. Georgi and S. Glashow, "Unity of all elementary particle forces," *Phys.Rev.Lett.*, vol. 32, pp. 438–441, 1974.

[39] N. Polonsky, "Supersymmetry: Structure and phenomena. extensions of the Standard Model," *Lect.Notes Phys.*, vol. M68, pp. 1–169, 2001.

[40] U. Ellwanger, C. Hugonie, and A. M. Teixeira, "The Next-to-Minimal Supersymmetric Standard Model," *Phys.Rept.*, vol. 496, pp. 1–77, 2010.

[41] D. Chung, L. Everett, G. Kane, S. King, J. D. Lykken, *et al.*, "The soft Supersymmetry breaking Lagrangian: Theory and applications," *Phys.Rept.*, vol. 407, pp. 1–203, 2005.

[42] P. Langacker, N. Polonsky, and J. Wang, "A low-energy solution to the mu problem in gauge mediation," *Phys.Rev.*, vol. D60, p. 115005, 1999.

[43] S. Chatrchyan *et al.*, "Search for high mass resonances decaying into τ^- lepton pairs in pp collisions at $\sqrt{s} = 7$ TeV," *Phys.Lett.*, vol. B716, pp. 82–102, 2012.

[44] CERN, "LEP design report. vol. 1. the LEP injector chain," tech. rep., 1983.

[45] CERN, "LEP design report: Vol. 2. the LEP main ring," tech. rep., 1984.

[46] K. Hagiwara *et al.*, "Review of particle physics. Particle Data Group," *Phys.Rev.*, vol. D66, p. 010001, 2002.

[47] M. S. Carena, A. Daleo, B. A. Dobrescu, and T. M. Tait, "Z' gauge bosons at the Tevatron," *Phys.Rev.*, vol. D70, p. 093009, 2004.

[48] T. Aaltonen *et al.*, "Search for high mass resonances decaying to muon pairs in $\sqrt{s} = 1.96$ TeV $p\bar{p}$ collisions," *Phys.Rev.Lett.*, vol. 106, p. 121801, 2011.

[49] D. Acosta *et al.*, "Search for new physics using high mass tau pairs from 1.96 TeV $p\bar{p}$ collisions," *Phys.Rev.Lett.*, vol. 95, p. 131801, 2005.

[50] T. Aaltonen *et al.*, "Search for new particles decaying into dijets in proton-antiproton collisions at $\sqrt{s}$= 1.96-TeV," *Phys.Rev.*, vol. D79, p. 112002, 2009.

[51] S. Chatrchyan *et al.*, "Search for resonances in the dilepton mass distribution in pp collisions at $\sqrt{(}s) = 7$ TeV," *JHEP*, vol. 1105, p. 093, 2011.

[52] G. Aad *et al.*, "Search for dilepton resonances in pp collisions at $\sqrt{s} = 7$ TeV with the ATLAS detector," *Phys.Rev.Lett.*, vol. 107, p. 272002, 2011.

[53] A. Breskin and R. Voss, *The CERN Large Hadron Collider: Accelerator and Experiments*. Geneva: CERN, 2009.

[54] K. Aamodt *et al.*, "The ALICE experiment at the CERN LHC," *JINST*, vol. 3, p. S08002, 2008.

[55] J. Alves, A. Augusto *et al.*, "The LHCb Detector at the LHC," *JINST*, vol. 3, p. S08005, 2008.

[56] G. Aad *et al.*, "The ATLAS experiment at the CERN Large Hadron Collider," *JINST*, vol. 3, p. S08003, 2008.

[57] CMS Collaboration, "Absolute calibration of luminosity measurement at CMS: Summer 2011 update," tech. rep., 2011.

[58] S. Chatrchyan *et al.*, "Energy calibration and resolution of the CMS electromagnetic calorimeter in pp collisions at $\sqrt{s} = 7$ TeV," *JINST*, vol. 8, p. P09009, 2013.

[59] S. Banerjee and S. Banerjee, "Performance of hadron calorimeter with and without HO," tech. rep., 1999.

[60] S. Chatrchyan *et al.*, *The CMS muon project: Technical Design Report*. Technical Design Report CMS, Geneva: CERN, 1997.

[61] R. Fruhwirth, "Application of Kalman filtering to track and vertex fitting," *Nucl.Instrum.Meth.*, vol. A262, pp. 444–450, 1987.

[62] S. Dasu *et al.*, "CMS. The TriDAS project. Technical design report, vol. 1: The trigger systems," tech. rep., 2000.

[63] E. Meschi, T. Monteiro, C. Seez, and P. Vikas, "Electron reconstruction in the CMS electromagnetic calorimeter," tech. rep., 2001.

[64] M. Cacciari, G. P. Salam, and G. Soyez, "The Anti-k(t) jet clustering algorithm," *JHEP*, vol. 0804, p. 063, 2008.

[65] S. Chatrchyan *et al.*, "Determination of jet energy calibration and transverse momentum resolution in CMS," *JINST*, vol. 6, p. P11002, 2011.

[66] CMS Collaboration, "b-Jet Identification in the CMS Experiment," tech. rep., 2012.

[67] M. L. Perl, G. Abrams, A. Boyarski, M. Breidenbach, D. Briggs, *et al.*, "Evidence for anomalous lepton production in e^+ - e^- annihilation," *Phys.Rev.Lett.*, vol. 35, pp. 1489–1492, 1975.

[68] F. Lacroix, "Missing transverse energy performance with the CMS detector," *PoS*, vol. EPS-HEP2011, p. 191, 2011.

[69] R. K. Ellis, I. Hinchliffe, M. Soldate, and J. van der Bij, "Higgs decay to $\tau^+\tau^-$: A possible signature of intermediate mass higgs bosons at the SSC," *Nucl.Phys.*, vol. B297, p. 221, 1988.

[70] G. Bayatian *et al.*, "CMS technical design report, volume ii: Physics performance," *J.Phys.*, vol. G34, pp. 995–1579, 2007.

[71] T. Sjostrand, S. Mrenna, and P. Z. Skands, "PYTHIA 6.4 physics and manual," *JHEP*, vol. 0605, p. 026, 2006.

[72] F. Maltoni and T. Stelzer, "MadEvent: Automatic event generation with MadGraph," *JHEP*, vol. 0302, p. 027, 2003.

[73] S. Jadach, J. H. Kuhn, and Z. Was, "TAUOLA: A Library of Monte Carlo programs to simulate decays of polarized tau leptons," *Comput.Phys.Commun.*, vol. 64, pp. 275–299, 1990.

[74] A. Abulencia *et al.*, "Search for neutral MSSM Higgs bosons decaying to tau pairs in $p\bar{p}$ collisions at $\sqrt{s} = 1.96$ TeV," *Phys.Rev.Lett.*, vol. 96, p. 011802, 2006.

[75] CMS Collaboration, "Electron reconstruction and identification at sqrt(s) = 7 TeV," Tech. Rep. CMS-PAS-EGM-10-004, CERN, Geneva, 2010.

[76] S. Chatrchyan *et al.*, "Measurement of the Inclusive W and Z Production Cross Sections in pp Collisions at $\sqrt{s} = 7$ TeV," *JHEP*, vol. 1110, p. 132, 2011.

[77] S. Chatrchyan *et al.*, "Measurement of the inclusive Z cross section via decays to tau pairs in pp collisions at $\sqrt{s} = 7$ TeV," *JHEP*, vol. 1108, p. 117, 2011.

[78] CMS Collaboration, "Absolute calibration of the luminosity measurement at CMS: Winter 2012 update," tech. rep., 2012.

[79] P. M. Nadolsky, H.-L. Lai, Q.-H. Cao, J. Huston, J. Pumplin, *et al.*, "Implications of CTEQ global analysis for collider observables," *Phys.Rev.*, vol. D78, p. 013004, 2008.

[80] A. Martin, W. Stirling, R. Thorne, and G. Watt, "Update of parton distributions at NNLO," *Phys.Lett.*, vol. B652, pp. 292–299, 2007.

[81] M. Ubiali, "NNPDF1.0 parton set for the LHC," *Nucl.Phys.Proc.Suppl.*, vol. 186, pp. 62–65, 2009.

[82] G. Nanava and Z. Was, "How to use SANC to improve the PHOTOS Monte Carlo simulation of bremsstrahlung in leptonic W boson decays," *Acta Phys.Polon.*, vol. B34, pp. 4561–4570, 2003.

[83] G. Miu and T. Sjostrand, "W production in an improved parton shower approach," *Phys.Lett.*, vol. B449, pp. 313–320, 1999.

[84] G. Aad *et al.*, "A search for high-mass resonances decaying to $\tau^+\tau^-$ in pp collisions at $\sqrt{s} = 7$ TeV with the ATLAS detector," *Phys.Lett.*, vol. B719, pp. 242–260, 2013.

[85] S. Chatrchyan *et al.*, "Search for heavy narrow dilepton resonances in pp collisions at $\sqrt{s} = 7$ TeV and $\sqrt{s} = 8$ TeV," *Phys.Lett.*, vol. B720, pp. 63–82, 2013.

APPENDIX A

SUMMARY OF OTHER DITAU CHANNELS INCLUDED IN THE SEARCH

A.1 Event Selections

The analysis selections are divided into three categories: geometric and kinematic acceptance, object identification, and topological selections as given below for the $\mu\tau_{\rm h}$, $\tau_{\rm h}\tau_{\rm h}$, and $e\mu$ channels. A summary of all signal selections is shown on Figure A.1.

A.2 $\mu\tau_{\rm h}$ Channel

The signal selections for the $\mu\tau_h$ final state are listed below:

Acceptance Selections:

- ≥ 1 Global muon) with $p_T > 20$ GeV/c and $|\eta| < 2.1$
- ≥ 1 PFTau with $p_T > 20$ GeV/c and $|\eta| < 2.1$
- ≥ 1 $\mu\tau_h$ pair with $\Delta R(\mu, \tau_h) > 0.7$

Muon Selections:

- ≥ 1 μ with tracker hits ≥ 10
- ≥ 1 μ with pixel hits ≥ 1
- ≥ 1 μ with ≥ 2 matching segments
- ≥ 1 μ with χ^2/ndof < 10
- ≥ 1 μ $|d_0| < 0.2$ cm

- ≥ 1 μ passing isolation $\sum p_T$ of tracks and Ecal RecHits < 1

Tau Selections:

- ≥ 1 τ_h passing the HPS "tight" muon veto
- ≥ 1 τ_h passing the HPS "tight" electron veto
- ≥ 1 τ_h passing the HPS decay mode finding
- ≥ 1 τ_h passing the HPS "medium" isolation

Topological Selections:

- $Q(\mu) \times Q(\tau_h) < 0$
- $\not\!\!E_{\rm T} > 30$ GeV
- $\cos\Delta\phi(\mu, \tau_h) < -0.95$
- $p_\zeta - 0.875 p_\zeta^{\rm vis} > -7$
- Zero jets tagged as b-jets using the TCHEM working point

A.3 $\tau_{\rm h}\tau_{\rm h}$ Channel

The $\tau_{\rm h}\tau_{\rm h}$ event selections are:

Acceptance:

- At least two HPS-taus
- $p_{\rm T} > 35$ GeV/c on both legs
- $|\eta| < 2.1$ on both legs

- $\Delta R(\tau_1, \tau_2) > 0.7$

Tau identification:

- Crack veto on both legs
- Leading track $p_{\mathrm{T}} > 5$ GeV/c on both legs
- True medium HPS-tau electron discriminant (electron veto) on both legs
- True loose HPS-tau muon discriminant (muon veto) on both legs
- True loose HPS-tau isolation on both legs
- True HPS-tau discriminant by decay mode finding on both legs
- Exactly one signal track on each leg

Topology:

- Charge product of both legs equal to -1
- $\cos\left(\Delta\phi(\tau_1, \tau_2)\right) < -0.95$
- $E_{\mathrm{T}}^{\mathrm{miss}} > 20$ GeV
- $p_\zeta - 0.875 \cdot p_\zeta^{vis} > -7$
- No jets tagged as b-jets (TCHEM)

A.4 $e\mu$ Channel

The selections for the $e\mu$ channel are:

Acceptance Selections:

- ≥ 1 Global muon with $p_T > 20$ GeV/c and $|\eta| < 2.1$
- ≥ 1 Electron with $p_T > 15$ GeV/c and $|\eta| < 2.1$
- ≥ 1 $e\mu$ pair with $\Delta R(e, \mu) > 0.7$

Muon Selections:

- ≥ 1 μ with tracker hits ≥ 10
- ≥ 1 μ with pixel hits ≥ 1
- ≥ 1 μ with ≥ 2 matching segments
- ≥ 1 μ with χ^2/ndof < 10
- ≥ 1 μ $|d_0| < 0.2$ cm
- ≥ 1 μ passing isolation $\sum p_T$ of tracks < 3.0 and Ecal RecHits < 3.5

Electron Selections:

- Electrons are required to pass HEEP selection criteria
- Ecal Isolation: $\Sigma \mathrm{E_T}^{ecal} < 3.5$ GeV
  ($\mathrm{E}_{barrel}^{EcalRecHit} > 0.08$ GeV, $\mathrm{E_T}_{endcap}^{EcalRecHit} > 0.1$ GeV, $\Delta \mathrm{R}_{iso} = 0.3$)
- Track Isolation $\Sigma \mathrm{p_T}^{trk} < 3.0$ GeV/c ($\mathrm{p_T}^{trk} > 0.7$ GeV/c, $\Delta \mathrm{R}_{iso} = 0.3$)

Topological Selections:

- $Q(\mu) \times Q(\tau_h) < 0$
- $\not{E}_{\mathrm{T}} > 20$ GeV
- $\cos\Delta\phi(\mu, \tau_h) < -0.95$

	$\mu\,\tau_h$	$e\,\tau_h$	$e\,\mu$	$\tau_h\,\tau_h$
		Acceptance		
$\Delta R(\tau_1,\tau_2) >$	0.7	0.7	0.7	0.7
$\tau_h\,p_T >$	20 GeV/c	20 GeV/c	—	35 GeV/c
$\mu\,p_T >$	20 GeV/c	—	20 GeV/c	—
$e\,p_T >$	—	20 GeV/c	15 GeV/c	—
$\lvert\eta_{\tau_{1,2}}\rvert <$	2.1	2.1	2.1	2.1
		Muon ID		
Global muon	Yes	—	Yes	—
$\lvert d_0\rvert <$	0.2cm	—	0.2cm	—
Pion veto	Yes	—	Yes	—
$\sum p_T^{iso\ trk} <$	1.0 GeV ($R_{iso}=0.5$)	—	3.0 GeV ($R_{iso}=0.5$)	—
$\sum E_T^{iso\ \gamma} <$	1.0 GeV ($R_{iso}=0.5$)	—	3.5 GeV ($R_{iso}=0.5$)	—
		Electron ID		
HEEP req's	—	Yes	Yes	—
$\sum p_T^{iso\ trk} <$	—	3.5 GeV ($R_{iso}=0.4$)	3.0 GeV ($R_{iso}=0.3$)	—
$\sum E_T^{iso\ \gamma} <$	—	4.5 GeV ($R_{iso}=0.4$)	3.5 GeV ($R_{iso}=0.3$)	—
		Tau ID		
Leading trk $p_T >$	—	—	—	5 GeV/c
HPS electron veto	Tight	Tight	—	Medium
HPS muon veto	Tight	Tight	—	Loose
HPS decay mode find.	True	True	—	True
Num. of signal tracks	—	—	—	1
HPS isolation	Medium	Medium	—	Loose
		Topology		
$\cos\Delta\phi(\tau_1,\tau_2) <$	-0.95	-0.95	-0.95	-0.95
$Q(\tau_1)\times Q(\tau_2)$	-1	-1	-1	-1
$\not\!\!E_T >$	30 GeV	30 GeV	20 GeV	20 GeV
$\sum E_T$(other jets) $<$	—	—	150 GeV	—
$\Delta\phi(\ell_{lead}, MET) <$	—	—	0.6	—
ζ	$p_\zeta - 0.875 p_\zeta^{vis} > -7$	$p_\zeta - 0.875 p_\zeta^{vis} > -7$	$p_\zeta - 1.25 p_\zeta^{vis} > -10$	$p_\zeta - 0.875 p_\zeta^{vis} > -7$
Num. TCHEM b-tags	0	0	0	0

Figure A.1: Summary of Signal Region Event Selections for the Four Most Sensitive Ditau Channels.

- ΣE_T (other jets) < 150 GeV
- $\Delta\phi(l_{lead}, \not\!\!E_T) < 0.6$
- $p_\zeta - 0.875 p_\zeta^{\rm vis} > -10$
- Zero jets tagged as b-jets using the TCHEM working point

A.5 Data in the Signal Region

The analysis strategy for the $\mu\tau_h$, $e\mu$, and $\tau_h\tau_h$ channels was similar to the approach described in this thesis for the $e\tau_h$ channel. After appropriate studies of

Process	$\tau_e\tau_\mu$	$\tau_e\tau_h$	$\tau_\mu\tau_h$	$\tau_h\tau_h$
$Z \to \tau^+\tau^-$	$816 \pm 58 \pm 44$	$462 \pm 56 \pm 24$	$804 \pm 53 \pm 44$	$30.9 \pm 3.6 \pm 4.3$
$Z \to \mu^+\mu^-$	–	–	$20.8 \pm 8.3 \pm 1.1$	–
$Z \to e^+e^-$	–	$220 \pm 24 \pm 11$	–	$0.66 \pm 0.33 \pm 0.22$
W+jets	$83 \pm 15 \pm 7$	$181 \pm 36 \pm 13$	$459 \pm 26 \pm 29$	$5.8 \pm 1.7 \pm 1.1$
WW	$55.6 \pm 1.4 \pm 1.9$	–	$24.59 \pm 0.80 \pm 0.80$	–
WZ	$5.60 \pm 0.35 \pm 0.22$	–	–	–
$t\bar{t}$	$9.6 \pm 1.2 \pm 0.7$	$10.8 \pm 2.8 \pm 0.9$	$46.2 \pm 6.9 \pm 3.7$	$0.00^{+0.76+0.15}_{-0.00}$
QCD	$45.1 \pm 3.3 \pm 9.0$	$185 \pm 31 \pm 19$	$72 \pm 18 \pm 8$	$467 \pm 26 \pm 67$
Total	$1015 \pm 60 \pm 45$	$1058 \pm 77 \pm 35$	$1427 \pm 63 \pm 53$	$504 \pm 26 \pm 67$
Observed	1044	1043	1422	488

Figure A.2: Number of Observed Events in Data and Estimated Background Events for the Whole Mass Range. The first and second uncertainties are the statistical and systematic, respectively.

backgrounds in the control regions, the execution of data-driven background estimation methods, and the validation of the event selections, each of the individual analyses was unblided. The event rates for all the four $\tau^+\tau^-$ channels used in the statistical combination of this search are shown in Figure A.2. The mass distributions for the $\mu\tau_h$, $e\mu$, and $\tau_h\tau_h$ channels are shown in Figure A.3.

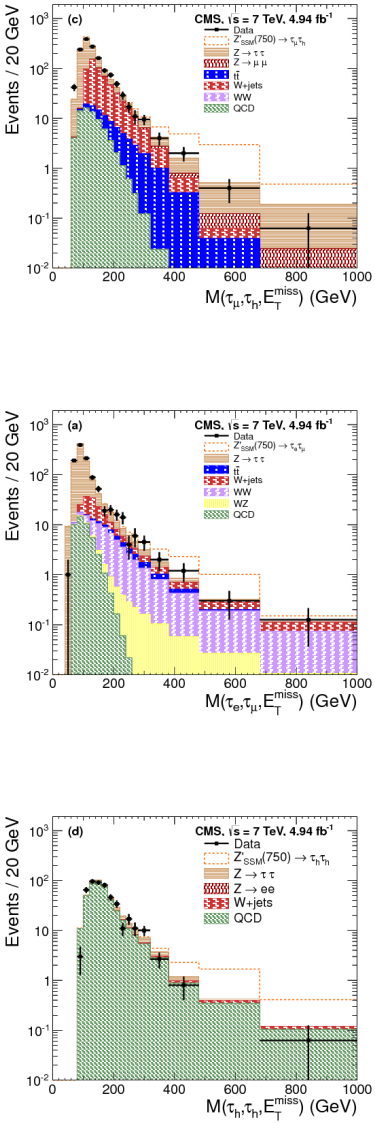

Figure A.3: The Distribution of the Invariant Mass, $M(\tau_1, \tau_2, \not{E}_{\mathrm{T}})$, for the (a) $\mu\tau_{\mathrm{h}}$, (b) $e\mu$, and (c) $\tau_h\tau_h$ Final States. The dashed line represents the expectation for the production of the Z'_{SSM} boson, as predicted by the Sequential Standard Model, with a mass of 750 GeV/c^2.